INFILTRATION OF FIBROUS PREFORMS BY A PURE METAL

by

LAWRENCE JAY MASUR

B.S. Physics, University of Connecticut 1979

S.M. Metallurgy, Massachusetts Institute of Technology 1982

SUBMITTED TO THE DEPARTMENT OF
MATERIALS SCIENCE AND ENGINEERING
IN PARTIAL FULFILLMENT OF THE REQUIREMENTS
FOR THE DEGREE OF

DOCTOR OF PHILOSOPHY

at the

MASSACHUSETTS INSTITUTE OF TECHNOLOGY

February 1988

Signature of Author _____
Department of Materials Science and Engineering
January 8, 1988

Certified by _____
James A. Cornie
Thesis Supervisor

Certified by _____
Andreas Mortensen
Thesis Supervisor

Certified by _____
Merton C. Flemings
Thesis Supervisor

Accepted by _____
John B. Vander Sande, Chairman
Departmental Commitee on Graduate Students

INFILTRATION OF FIBROUS PREFORMS BY A PURE METAL

by

LAWRENCE JAY MASUR

Submitted to the Department of Materials Science and Engineering on January 8, 1988 in partial fulfillment of the requirements for the Degree of Doctor of Philosophy in Materials Engineering

ABSTRACT

This thesis comprises an investigation of the flow of pure metals into fibrous preforms. General expressions are given to describe the infiltration. The expressions are solved analytically for simplified cases of practical interest. Solutions are given to the problem of unidirectional infiltration into a preform of aligned fibers under a constant applied pressure. Cases of the fibers at temperatures both above and below the metal melting point are considered. The case of greater engineering significance, that of the fibers at a temperature below the metal melting point, is solved to elucidate the effect on infiltration kinetics of parameters including: 1) fiber temperature, 2) metal temperature, 3) fiber volume fraction, 4) applied pressure, 5) fiber diameter, 6) fiber orientation, 7) fiber thermal properties, 8) mold radius, and 9) heat transfer coefficient.

It is concluded the basic mechanism leading to the above observed effect is the solidification of metal around the fibers in the form of a sheath. Metal superheat, when present, serves to progressively remelt the solidified sheath from the upstream end of the preform. Fiber volume fraction is predicted to have a major effect on infiltration kinetics, and metal superheat a relatively minor effect. Applied pressure has a parabolic effect on the infiltration kinetics for the case of negligible capillary pressure.

When no external heat extraction is present and a constant pressure is applied to the metal, flow through the preform will continue indefinitely. For the more practical case of external heat extraction, flow will cease when solidification from the external heat sink has closed the flow channel. This will occur first at the entrance to the fiber preform and is predicted analytically for simple geometries. Curves are presented for the predicted total infiltrated length as a function of fiber volume fraction, fiber temperature, and applied pressure.

Experiments were performed to test the results of the theory. An apparatus was designed and built for unidirectional infiltration under constant pressure and carefully controlled temperature parameters. A sensor was also developed to measure the position of the liquid metal in the fibrous preform during the experiment. This technique enabled quantitative comparison of theory and experiment.

Excellent agreement between theory and experiment was obtained for the case of 99.999% aluminum and Saffil™ alumina fibers fabricated into two-dimensionally random preforms. Fiber volume fraction was varied from 0.22 to 0.26, fiber preheat temperature was varied from approximately 210°C to 470°C, and metal superheat was varied from 20°C to 185°C. Infiltration pressure was varied from 0.9MPa to 4.5MPa (130psi to 650psi). Agreement between theory and experiment was excellent above about 2 MPa. Below this pressure, there was some deviation due, it is believed, to a larger than expected capillary pressure. The impurity level of the metal was also found to significantly influence infiltration. The measured preform permeability for 99.9% aluminum was much lower than that for 99.999% aluminum and is discussed in terms of solidification morphology.

The simple one dimensional analytical model presented in this work can be used to predict quantitatively the infiltration behavior in some cases of practical interest, such as fiber-reinforced rods, tubes, and pistons.

Thesis Supervisor: Dr. James A. Cornie
Title: Director, Center for the Processing and Evaluation of Metal and Ceramic Matrix Composites

Thesis Supervisor: Professor Merton C. Flemings
Title: Head, Department of Materials Science and Engineering and
Toyota Professor of Materials Processing

PREFACE

This thesis has been written as two self-contained journal style articles. Each article occupies a full chapter of the thesis (Chapters 1 and 2) and contains an introduction, conclusion, and references section in addition to the main body. Also, the figures associated with each article are contained within the chapter. Chapter 3 is the summary and conclusions of the entire thesis and encompasses Chapters 1 and 2. Chapter 4 contains the suggestions for further work.

TABLE OF CONTENTS

LIST OF FIGURES - CHAPTER 1

LIST OF FIGURES - CHAPTER 2

LIST OF TABLES

ACKNOWLEDGMENTS

The success of this work depended not on the contribution of a single person, but on the contributions of many people, and I would now like to thank them.

My thanks to my three advisors, Dr. James Cornie, Professor Andreas Mortensen, and Professor Merton Flemings; to Dr. Cornie for his vision of the future and power of persuasion to secure funding for this work, to Professor Mortensen for the day-to-day and hour-to-hour support, not to mention the late-night writing sessions; and to Professor Flemings for the ability to see the end and the encouragement to get me there. A special thanks to Maria Wehrle Due for her unfailing help and endless enthusiasm; to Dr. Joseph Blucher for the design and assistance in contruction of the pressure vessel; and to Mr. Terry Wong for many hours of talented assistance in the laboratory.

A very special thanks to General Motors Corporation for providing support under the supervision of Mr. Gerald Backer.

I am particularly grateful to my fiancee, Dale Sokoloff, for her understanding and unfailing support of my efforts, and especially for her insight and advice that enabled me to finish this work.

Lawrence J. Masur

Cambridge, Massachusetts
January, 1988

Chapter 1
INFILTRATION OF FIBROUS PREFORMS BY A PURE METAL
PART I: THEORY

I. INTRODUCTION

In 1982 Toyota introduced a fiber reinforced aluminum piston for use in a diesel engine [1], heralding the first commercial application of a fiber-reinforced metal. This introduction of a component of superior performance without an associated cost penalty aroused great interest in liquid metal infiltration for metal matrix composite (MMC) fabrication [2]. The liquid metal infiltration process consists of the injection and subsequent solidification of liquid metal into the interstitial spaces within a collection of ceramic fibers. While many researchers have studied the flow of fluids through porous media, both particulate [3,4] and fibrous [5,6,7], they have not considered the concurrent flow and solidification of a liquid metal. In MMC fabrication practice the fibers are generally held at a temperature significantly below that of the melt, making the concurrent solidification phenomenon considerably important.

Researchers in the field of foundry engineering have studied the concurrent flow and solidification of a metal in a mold. The study of this phenomenon, termed fluidity by foundrymen, has

concentrated on understanding the effects of such variables as metal and mold temperatures and metallostatic head [8], alloy composition [9,10], and surface tension and mold vibration [11,12], to name but a few. However, this work does not treat the flow of metal through a porous medium.

The problem of liquid metal infiltration of a fibrous ceramic preform is then a superposition of the two problems of flow through a porous medium and solidification during flow. This body of engineering has not been well investigated, with just a few processing studies emerging in recent years despite the considerable engineering relevance of the problem. In the area of flow of liquid metals through packed beds of particles, Nagata and Matsuda [13,14] have studied particles ranging in size from 37μm to 3400μm. They propose the existence of a critical preheat temperature, based upon physical constants of the metal and particles, above which the particles must be heated in order for infiltration to occur. Their parameter is based upon an overall thermal balance. Hosking and Netz [15] have studied the infiltration of an aluminum alloy into a packed bed of particles ranging in size from 3mm to 9mm. They present a statistically derived expression that is based upon their experimental results. No expressions are presented relating results to first principles.

On the flow of liquid metals through assemblies of fibers, Fukunaga and Goda have made experimental measurements and theoretical calculations of the permeability of a fibrous preform. They propose the formation of a layer of solidified

metal on the fibers and verify its existence through the use of mechanical tests on leached out fibers [16]. They then derive a Kozeny-type expression for the infiltration coefficient and compare it to experimental measurements [17]. They also propose a critical infiltration velocity as the mechanism for cessation of flow. Girot et al. [18] have performed a numerical analysis of the infiltration of liquid alloys into fibrous preforms. In this work they have proposed a model to predict the effect of various processing parameters on the depth of infiltration. They propose flow ceases when the metal cools to a critical temperature, but they do not account for the release of latent heat of solidification in their calculations. They also have not yet confirmed their calculations experimentally. Clyne et al. [19,20,21] have also considered the flow of liquid metal through a fibrous preform. They calculate the critical pressure necessary for melt infiltration and the effect of infiltration pressure on fiber preform deformation. They also explain the evolution of the composite microstructure, including an interpretation of the role of metal superheat.

This chapter describes the flow of pure liquid metal through a fibrous ceramic preform. A general case is first described, with solutions to specific cases following. A clear physical picture of the infiltration of a fibrous preform by a pure metal is developed, and a simple analytical model is presented to quantitatively predict infiltration behavior, with a specific consideration for the effect of those parameters that would be most appropriate to an engineer attempting to fabricate a part.

In the following chapter the calculations are compared with experimental measurements.

II. DESCRIPTION OF GENERAL PROBLEM

Consider the infiltration of a fibrous preform by a pure liquid metal. Figure 1 schematically illustrates the process by which a three-dimensional, selectively-reinforced part could be fabricated. In this example the pure liquid metal and the fibrous preform do not wet one another, requiring the application of pressure to force the metal through the preform. The objective of this thesis is to describe, both physically and mathematically, the flow of the metal through the preform.

The infiltrated portion of the preform is bound by surfaces S_1, S_2, S_3 and S_4, where S_1 is the infiltrated preform/ unreinforced liquid metal bath interface, S_2 the infiltrated preform/ uninfiltrated preform interface, S_3 the infiltrated preform/ mold wall interface, and S_4 the infiltrated preform/ solid metal interface. General aspects of the problem of infiltration can be appreciated by considering briefly the interactions at each surface.

Along S_1 the velocity of the metal and its temperature are continuous. At S_2 the liquid metal interacts with the fibers both chemically and thermally. If, for example, the metal does not wet the fibers (which is generally the case for fiber and metal systems of practical interest) then the pressure in the liquid metal at S_2 will be greater than the ambient pressure

ahead of the interface by an amount equal to the capillary pressure. This capillary pressure would need to be overcome before movement of the liquid metal could occur.

Also at S_2 the metal begins to exchange heat with the fibers. In this work it is assumed that the liquid metal is incompressible and that its flow upon entering the fiber preform is governed by Darcy's law, the equation and limitations for which are presented in section III. It is also assumed that heat transfer between the fibers and the metal is instantaneous. We thus treat the composite as one in which temperature variations are very small on the scale of the fiber. In both the fluid flow and heat transfer equations we therefore make use of the same differential element, which is small on the scale of the composite but sufficiently large to contain several fibers. It is assumed that viscous energy dissipation is negligible and that variations in density with temperature are negligible. Heat transfer to and from this volume element within the infiltrated preform is then dictated by the heat transfer equation presented in section III. The assumption of instantaneous heat transfer clarifies the physical model and simplifies the analytical model; the validity of this assumption is considered in section IV along with its effect.

Consideration of only the surfaces S_1 and S_2 (that is, S_3 is assumed to be adiabatic and S_4 non-existent) comprise a model where only the interactions between the metal and fibers are considered. This is termed the adiabatic model and described fully in section IV. The objective of the model is to predict

the spatial relationship between S_1 and S_2 at any time. The complete engineering problem, however, must necessarily include the surfaces S_3 and S_4, as described below.

At S_3 the metal is generally in contact with a surface below the metal melting point, resulting in the formation of solid metal. The problem thus now involves the consideration of another interface, S_4, which progresses towards the center of the casting cavity with time. The problem is similar to the adiabatic model mentioned above, except that flow can occur only within an inner "core" of the preform. This model, which includes interactions from all four interfaces, is termed the non-adiabatic model and comprises the adiabatic model coupled with a casting fluidity model. The non-adiabatic model is quantified in section V.

The problem of infiltration of a fibrous preform by a pure metal is then described by consideration of the interactions at all four interfaces. In general the solution is complex, in part because it is a free-boundary problem in which both the infiltration front and the solidification front must be derived. Solutions of the problem for specific cases are given below, to demonstrate essential features of the infiltration of a fibrous preform by a pure metal. These solutions are given following consideration of some general aspects of infiltrated fibrous composites.

III. UNIDIRECTIONAL INFILTRATION OF A REGULAR ARRAY OF FIBERS

Consider the case of liquid metal flowing unidirectionally through a fibrous preform. Under this assumption we develop expressions for the permeability, thermal conductivity, capillarity, heat transfer and fluid flow aspects of the problem which will be used in the solution of specific cases that are to follow.

A. Permeability

A comprehensive summary of existing experimental and theoretical work on the permeability of fibrous preforms has been recently published by Jackson and James [5]. Work to date has concentrated on aligned fiber networks, for flow both parallel and transverse to the fibers, on random 2D filter mats, and on random tri-dimensional fiber arrays. From their review, it is apparent that:

1) reliable experimental data exist over a wide range of fiber diameters ranging from 10Å to 10mm. In a plot of non-dimensionalized permeability as a function of solid volume fraction, all data fall roughly on a single curve, with a scatter band that narrows when data for flow parallel to the fibers, perpendicular to the fibers and through random 3-D mats are separated. Within each of these classes, most data fall within a factor two of one

another.

2) theoretical work has been proposed to model the permeability of each of these media. Most models agree well with the data, and it thus generally makes little difference whether a square array or a triangular array, for example, is assumed in the model.

3) the permeability for flow parallel to the fibers is about twice that for flow perpendicular to the fibers. The permeability of most fiber preforms (2-D random and parallel fiber preforms in particular) is thus not isotropic.

4) the presence of inhomogeneities in the fiber distribution within the preform increases the permeability significantly.

In the present study we are concerned with homogeneous fiber preforms with solid volume fractions of, at minimum, 0.20 for 2-D random preforms and 0.50 for parallel fiber preforms. Of the various models proposed, we have chosen to use the following expressions due to their range of validity and relative simplicity. Both assume that the fibers are continuous, with parallel axes located on a square grid. The first of these is:

$$K = \frac{0.427\, r_{sf}^2}{V_{sf}} \left[1 - \sqrt{\frac{2V_{sf}}{\pi}}\right]^4 \left[1 + 0.473 \left[\sqrt{\frac{\pi}{2V_{sf}}} - 1\right]\right] \qquad (1)$$

for flow parallel to the fiber axes, where r_{sf} is the radius of

the solid material and V_{sf} is its volume fraction. Equation 1 is valid for solid volume fractions ranging from 0.5 to $\pi/4$ and is based on calculations of Drummond and Tahir [6]. The second equation to be used is:

$$K = \frac{2\sqrt{2}}{9} \frac{r_{sf}^2}{V_{sf}} \left[1 - \sqrt{\frac{4 V_{sf}}{\pi}} \right]^{\frac{5}{2}} \qquad (2)$$

for flow perpendicular to the fiber axes. Equation 2 is valid for solid volume fractions ranging from approximately 0.2 to $\pi/4$ and is based on an approximation to numerical calculations of Sangani and Acrivos [7]. It is accurate to within a factor 2. A plot of the dimensionless quantity K/r_{sf}^2, for both parallel and transverse cases, is presented in Figure 2.

B. Thermal Conductivity

Several authors have proposed calculations of the thermal conductivity of fiber composites [26-30]. For parallel continuous fibers, the thermal conductivity in the direction of the fiber axes is given by the rule of mixtures, regardless of the fiber distribution:

$$k_c = k_f V_f + k_m (1 - V_f) \qquad (3)$$

For heat flow in the direction perpendicular to the axes of parallel continuous fibers lying on a square array, the equation

we adopt for the thermal conductivity of the composite is:

$$k_c = k_m \frac{(k_f + k_m) + (k_f - k_m) V_f}{(k_f + k_m) - (k_f - k_m) V_f} \quad (4)$$

This relatively simple equation was given independently by two authors using different approaches [26,27], and matches closely with the more precise (but more complex) equation of Perrins et al. [28]. A plot of the dimensionless quantity k_c/k_m, for both parallel and transverse cases, is presented in Figure 3.

C. Capillarity

In this study liquid is forced into the preform by an applied pressure, P_o. Resisting flow is the ambient pressure, P_a, and the pressure drop due to surface tension at the tip of the flowing stream, ΔP_γ, where:

$$\Delta P_\gamma = \frac{2 V_f (\sigma_{FL} - \sigma_{FA})}{(1 - V_f) r_f} \quad (5)$$

where σ_{FL} is the fiber/ liquid metal surface energy and σ_{FA} is the fiber/ atmosphere surface energy [31]. Implicit in equation 5 is the assumption that the equilibrium contact angle is attained even under the dynamic conditions of flow.

Neglecting entrance effects (the fibers are of very small diameter and flow distances are relatively long) and effects of rate of change of momentum (see the following section), the total pressure drop, ΔP_T, driving flow is composed of the

pressure drop for viscous resistance, ΔP_μ, and that for surface tension, ΔP_γ:

$$\Delta P_T = \Delta P_\mu + \Delta P_\gamma \tag{6}$$

where $\Delta P_T = P_o - P_a$

$\Delta P_\gamma = P_t - P_a$

$\Delta P_\mu = P_o - P_t$

The pressure P_t is that pressure at the tip of the flowing stream just inside the liquid metal. The pressure drops calculated and plotted in much of the following are ΔP_μ.

D. Fluid Flow and Heat Transfer

For slow flow of an incompressible fluid, flow is governed by Darcy's law, which in one dimension is written as (neglecting any effect of gravity):

$$v_o = -\frac{K}{\mu}\frac{dP}{dx} \tag{7}$$

where v_o = superficial velocity of liquid metal (average velocity the metal would have if no fibers were present)

μ = viscosity of liquid metal

K = permeability

P = pressure

x = position

The range of validity of Darcy's law is usually specified by a range of Reynolds numbers, which for the case of flow through porous media is defined as [3,5,32]:

$$Re = 2 r_f \rho_m v / \mu \qquad (8)$$

where v is the average velocity of the liquid metal within the porous medium. Investigators usually specify a 'critical' Reynolds number, universal for all porous media, above which Darcy's law no longer applies. Scheidegger [33] protests that since the definition of the Reynolds number is based upon hydraulic radius theory, then the results must be regarded as subject to the same principal shortcomings as the theory itself. He concludes that the correlations are, at best, valid only for the specific porous media studied.

However, Jackson and James [5], in their review of experimental and theoretical work on flow through fibrous porous media, found that Darcy's law was obeyed for a variety of porous media and fluids when Re<10. This criterion was also supported by the work of Bergelin et al.[34] for measurements on precisely aligned rows of large diameter tubes oriented perpendicular to flow. Similarly, in his widely accepted work, Ergun [3] evaluated experiments using a variety of porous media and fluids to derive an expression for pressure drop that consisted of two terms, one which described viscous energy losses (i.e. Darcy's law) and the other which described kinetic energy losses (i.e. deviations from Darcy's law). From Ergun's work, an expression is easily derived to evaluate the relative importance of the two

terms:

$$\frac{\text{Kinetic energy losses}}{\text{Viscous energy losses}} = \frac{1.75}{150}\frac{Re}{V_f} \tag{9}$$

Therefore, the contribution of the kinetic energy loss term is less than 2% when $Re/V_f < 1.7$. This is a more conservative upper limit than Jackson and James. Similarly, Szekely [32] and Geiger and Poirier [35] indicate that the upper bound of the "creeping flow" regime is Re≈2. Therefore, most investigators believe that Darcy's law should describe the pressure drop for flow where the Reynolds number is less than approximately unity, a conclusion substantiated by experimental data.

In the present work we seek to determine the position of the infiltration front, L, which is related to the superficial velocity by:

$$v_o = (1 - V_f)\frac{dL}{dt} \tag{10}$$

where t is time. Equation 7 then becomes:

$$\frac{dL}{dt} = \frac{-K}{\mu(1 - V_f)}\frac{dP}{dx} \tag{11}$$

and K is given by equation 1 or 2 for longitudinal or transverse infiltration, respectively.

The equation governing heat transfer within the preform is, for the one dimensional case under consideration:

$$\rho_c c_c \frac{\partial T}{\partial t} + \rho_m c_m v_o \frac{\partial T}{\partial x} = k_c \frac{\partial^2 T}{\partial x^2} \tag{12}$$

where:

$\rho_c c_c$ = volumetric heat capacity of composite, equal to $\rho_f c_f V_f + \rho_m c_m (1-V_f)$

$\rho_f c_f$ = volumetric heat capacity of fibers

$\rho_m c_m$ = volumetric heat capacity of metal

V_f = volume fraction fibers in the composite

k_c = thermal conductivity of the composite

T = temperature

and k_c is given by equation 3 or 4 for longitudinal or transverse infiltration, respectively.

IV. ADIABATIC UNIDIRECTIONAL INFILTRATION OF A SQUARE ARRAY OF FIBERS ALONG ONE OF THEIR PRINCIPAL AXES; NEGLIGIBLE TEMPERATURE GRADIENTS TRANSVERSE TO THE FLOW DIRECTION

We assume now that the fiber preform is composed of continuous fibers, with parallel axes located on a square grid; Figure 4 is an example. Furthermore, we assume that the preform is a semi-infinite cylinder, the axis of which either coincides

with or is transverse to the fiber axis. The mold wall S_3 coincides with the cylinder surface, and is impermeable to any heat flow. The surface of contact with the metal, S_1, is planar and is perpendicular to the cylinder axis at x=0; infiltration is unidirectional along this axis. We also neglect any variations in preform density due to compression by the metal during infiltration, as was considered by Clyne et al.[20,21].

At t = 0, where t is time, the metal contacts the fiber preform at x = 0. The temperature and the pressure of the metal at x = 0 (T_o and P_o,respectively) remain constant throughout infiltration; the entire preform is initially at $T = T_f$. The infiltration front is planar and is located at x = L(t); Figure 4 describes the problem for infiltration in cross-flow, i.e. perpendicular to the fiber axes. Heat transfer between the fibers and metal is assumed to be instantaneous and so local temperature differences transverse to flow are negligible. Since the flow front is flat and heat transfer to the surroundings is zero, temperature differences over the preform diameter (perpendicular to flow) are also zero. In addition, the thermal transport properties of the fiber preform are much smaller than those of the liquid metal, therefore we neglect any thermal losses ahead of the infiltration front. This last assumption is invoked for clarity and simplicity in both the physical and analytical models; it is relaxed later in this section. Several cases of increasing complexity are now considered in what follows.

A. Case of fibers heated at or above metal melting point $(T_f \geq T_M)$.

The first metal entering the preform at t = 0 exchanges heat with the fibers instantaneously, as we have assumed. At t = 0+Δt, it will exchange heat with a new set of fibers, and aft encountering a finite number of fibers n at time t = (n-1)Δt, will reach the fiber temperature. The infiltration front therefore reaches very quickly the fiber temperature T_f.

The permeability of the preform, K, is constant everywhere, and the applied pressure is constant, therefore equation 11 can be integrated from x=0 at t=0 to x=L at t=t to yield:

$$\frac{L}{\sqrt{t}} = \sqrt{\frac{2\,\Delta P_\mu\, K}{\mu\,(1 - V_f)}} \equiv \Psi \qquad (13)$$

where $\Delta P_\mu = P_o - P_t$. The permeability K of the preform, in this case, is given by equation 1 or 2 for longitudinal or transverse infiltration, respectively, with $V_{sf} = V_f$, and $r_{sf} = r_f$, where r_f is the fiber radius. To derive the temperature profile, we define

$$\chi = \frac{x}{L}. \qquad (14)$$

Equation 12 then becomes:

$$(\chi - \beta)\frac{dT}{d\chi} = -\frac{2\alpha_c}{\Psi^2}\frac{d^2T}{d\chi^2} \qquad (15)$$

where:

$$\alpha_c = \frac{k_c}{\rho_c c_c}$$

and

$$\beta = \frac{\rho_m c_m (1 - V_f)}{\rho_c c_c}$$

Boundary conditions are:

$$\chi = 0, \quad T = T_o$$

$$\chi = 1, \quad -k_c \left(\frac{dT}{d\chi}\right)_{\chi=1} = \frac{\rho_f c_f V_f (T_{\chi=1} - T_f)}{2} \Psi^2$$

The solution is then:

$$\frac{T(\chi) - T_f}{T_o - T_f} = 1 - \frac{Y^2 Z \left[\text{erf}(Y\beta) + \text{erf}(Y(\chi - \beta))\right]}{\frac{2}{\sqrt{\pi}} e^{-Y^2(1-\beta)^2} + Y^2 Z \left[\text{erf}(Y\beta) + \text{erf}(Y(1 - \beta))\right]} \quad (16)$$

where: $Y = \frac{\Psi}{2\sqrt{\alpha_c}}$

$$Z = \frac{2 \rho_f c_f V_f}{\rho_c c_c}$$

Plots of equation 16 for various values of Ψ are shown in Figure 5, using as example the thermal values of pure aluminum metal and alumina fibers.

B. Case of fibers at a temperature below the metal melting point ($T_f < T_M$).

1. No metal superheat ($T_o = T_M$)

As before, the first metal entering the preform will exchange heat instantaneously with the fibers. However, in this case the metal tip is not necessarily cooled below its melting point T_M, for to do so would require complete solidification of

the metal. Instead, a portion of the metal at the tip solidifies, releasing latent heat and heating the fibers to the metal temperature T_M. We assume that the metal solidifies at its melting point at a very rapid rate so that formation of the solid is instantaneous at the tip. As the metal tip advances past a row of fibers, the solid metal which has formed is entrapped by the fiber network and left behind. The liquid metal tip, which is still at temperature T_M, encounters the next row of fibers and the process is repeated. Note that the temperature throughout the composite is constant at T_M, therefore heat transfer is impossible through the composite. The fraction of metal which solidifies, g_S, is given by a heat balance at the tip of the flowing stream:

$$g_s = \frac{\rho_f c_f V_f (T_M - T_f)}{\rho_m \Delta H (1 - V_f)} = \frac{V_s}{1 - V_f} \qquad (17)$$

where ΔH is the latent heat of fusion and V_S is the volume fraction of solid metal. Figure 6 shows the dependence of g_S on temperature and fiber volume fraction, using as example pure aluminum metal and alumina fibers. If the fibers are sufficiently cold to cause complete solidification of the metal (g_S=1), then infiltration of the preform is impossible. For the case of fibers preheated above this minimum temperature, flow may continue, with the following boundary conditions:

$$x = L: T = T_M \quad \text{and} \qquad (18)$$

$$x = L: (T_M - T_f) V_f \rho_f c_f = \rho_m \Delta H V_S \qquad (19)$$

In this work we consider the solidification of a pure metal, with the solidifying metal growing to form a cylindrical sheath around the fibers. The work of Fukunaga et al.[16] has provided experimental evidence for this solidification geometry. The morphology of the solid phase is therefore preserved: flow of the liquid takes place between fine cylinders composed of the original reinforcement surrounded by a uniform layer of solid metal, Figure 7. The volume fraction of solid phase, however, now varies and is given by:

$$V_{sf} = V_f + V_s \tag{20}$$

and the radius of the solid cylinders r_{sf} is:

$$r_{sf} = r_f \sqrt{\frac{V_{sf}}{V_f}} \tag{21}$$

The permeability of the preform is given by equations 1 and 2 for longitudinal and transverse flow, respectively, with V_{sf} and r_{sf} as given immediately above.

The rate of infiltration is given by equation 11 using the appropriate value of K, which is found from either equation 1 or equation 2, except that now V_{sf} and r_{sf} are given by equations 20 and 21, respectively. After integration from x=0 at t=0 to x=L at t=t, we obtain, as before:

$$\frac{L}{\sqrt{t}} = \sqrt{\frac{2\Delta P_\mu K}{\mu(1 - V_f)}} \equiv \Psi \tag{22}$$

Figure 8 shows the dependence of permeability K on fiber temperature and fiber volume fraction, while Figures 9 and 10

show the dependence of Ψ on fiber preheat temperature, fiber volume fraction, and infiltration pressure, for alumina fibers infiltrated in cross-flow by aluminum and conditions of practical significance. Figure 11 shows the dependence of infiltration length on time for different values of fiber preheat temperature for the same fiber-matrix system.

2. Finite metal superheat ($T_o > T_M$)

The metal enters the preform at a temperature, T_o, above the melting point. As described above, the tip of the metal stream will exchange heat instantaneously with the fibers it encounters. Its temperature will therefore be lowered very rapidly to the melting point, T_M. Thus the physical situation at the tip is identical to that of no metal superheat and solid metal will form according to equation 15.

Upstream, however, liquid metal is supplied at the superheat temperature, $T_o > T_M$. Close to $x = 0$, therefore, the temperature will be above T_M. In the region behind the tip, liquid and solid metal coexist and the temperature is necessarily uniform at T_M; within this region no heat transport is possible. The transition between this region where solid metal and liquid metal coexist at $T = T_M$ and that at $T > T_M$, extending downstream from $x = 0$, is a sharp boundary. In the geometry of the problem, this boundary is planar at some x defined as $L_s(t)$. The length L_s will increase with time as a result of continued gradual remelting of solid previously formed. Figure 12 schematically illustrates the effect of metal superheat.

To determine the temperature profile within the remelted region ($0 < x < L_s$), we use the same method of variable transformation as in section *A*. Equation 15 is again applicable:

$$(\chi - \beta)\frac{dT}{d\chi} = -\frac{2\alpha_c}{\Psi^2}\frac{d^2T}{d\chi^2} \tag{15}$$

with boundary conditions $\chi = 0$, $T = T_O$ and $\chi = \chi_S$, $T = T_M$, where χ_S is the position of the remelted front in χ-space. The solution is now:

$$\frac{T(\chi) - T_M}{\Delta T_s} = \frac{\operatorname{erf}\left[\frac{\Psi}{2\sqrt{\alpha_c}}(\chi - \beta)\right] - \operatorname{erf}\left[\frac{\Psi}{2\sqrt{\alpha_c}}(\chi_s - \beta)\right]}{\operatorname{erf}\left[\frac{\Psi}{2\sqrt{\alpha_c}}(-\beta)\right] - \operatorname{erf}\left[\frac{\Psi}{2\sqrt{\alpha_c}}(\chi_s - \beta)\right]} \tag{23}$$

where $\Delta T_S = T_O - T_M$ = metal superheat. An additional boundary condition is given from a heat balance at $x = L_S$:

$$-k_c \frac{\partial T}{\partial \chi}\Big)_{x=L_s,t} = \rho_m \Delta H V_s \frac{dL_s}{dt} \tag{24}$$

which, after the variable transformation, becomes:

$$\frac{T_o - T_M}{T_M - T_f} = A\chi_s(1-\beta)\sqrt{\pi}\left[\operatorname{erf}(A\beta) + \operatorname{erf}(A(\chi_s - \beta))\right] e^{[A(\chi_s - \beta)]^2} \tag{25}$$

where:

$$A = \frac{\Psi}{2\sqrt{\alpha_c}}$$

and implicitly defines χ_S. Plots of equation 23 for various

values of Ψ and χ_s are shown in Figures 13 and 14, using as example the thermal values of pure aluminum metal and alumina fibers.

The rate of infiltration is given by equation 11 treated separately in the two regions: 1) $0 < x < L_s$ and 2) $L_s < x < L$. Integrating from L=0 to L=L and t=0 to t=t yields:

$$\frac{L}{\sqrt{t}} = \sqrt{\frac{2\,\Delta P_\mu}{\mu\,(1 - V_f)\left[\frac{\chi_s}{K_1} + \frac{1-\chi_s}{K_2}\right]}} \equiv \Psi \qquad (26)$$

where K_1 is the permeability of the fiber preform in the remelted region and K_2 is the permeability of the fiber preform in the region where solid metal has formed. K_1 and K_2 are calculated using either V_f and r_f or V_{sf} and r_{sf}, respectively, in either equation 1 or equation 2. In practice, to calculate χ_s we graphically solve equation 25, resulting in the dimensionless plot shown in Figure 15. From this, we can then use equation 26 to calculate Ψ as a function of metal superheat, shown in Figure 16.

C. Effect of thermal losses ahead of the infiltration front

We now relax the assumption that the fiber preform ahead of the infiltration front does not transport heat. We focus attention on the case where the preform temperature T_f is lower than the metal melting point T_M. As before, the metal temperature at the infiltration front reaches T_M instantan-

eously, and solid metal forms to supply heat to the fibers, both at and ahead of the front. The resulting temperature profile is described in Figure 17. Let us "guess" that the infiltration front still advances as $L = \Psi\sqrt{t}$. Heat transport in the fibrous preform is described by:

$$\frac{\partial T}{\partial t} + \frac{\rho_g c_g}{\rho_c c_c} v_o \frac{\partial T}{\partial x} = \alpha_c \frac{\partial^2 T}{\partial x^2} \tag{27}$$

where ρ_g and c_g refer to the density and specific heat, respectively, of the gas that exists in the interfiber regions of the uninfiltrated preform, ρ_c and c_c refer to those same quantities for the uninfiltrated preform composite composed of fibers and gas, and α_c refers to the thermal diffusivity of the uninfiltrated preform composite. Boundary conditions are :

$$x \to \infty, \qquad T = T_f;$$

$$x = \Psi\sqrt{t}, \qquad T = T_M;$$

$$x = \Psi\sqrt{t}\ ; \qquad -k_c \frac{\partial T}{\partial x} = \rho_m \Delta H V_s \frac{dL}{dt} \tag{28}$$

Using the variable transformation of section *A*, equation 27 becomes:

$$(\chi - \beta)\frac{dT}{d\chi} = -\frac{2\alpha_c}{\Psi^2}\frac{d^2T}{d\chi^2} \tag{15}$$

where:

$$\beta = \frac{\rho_g c_g (1 - V_f)}{\rho_c c_c}$$

with boundary conditions $\chi = 1$, $T = T_M$ and $\chi \to \infty$, $T = T_f$.

The solution is then readily found:

$$\frac{T(\chi) - T_f}{T_M - T_f} = \frac{\operatorname{erf}\left[\frac{\Psi}{2\sqrt{\alpha_c}}(\chi - \beta)\right] - 1}{\operatorname{erf}\left[\frac{\Psi}{2\sqrt{\alpha_c}}(1 - \beta)\right] - 1} \tag{29}$$

The third boundary condition (equation 28) is obeyed provided:

$$V_s = \frac{V_f \rho_f c_f (T_M - T_f)}{\rho_m \Delta H}\left[\frac{1}{A\sqrt{\pi}}\frac{e^{-A^2}}{\operatorname{erfc}(A)}\right]\left[1 + \frac{\rho_g c_g (1 - V_f)}{\rho_f c_f V_f}\right] \tag{30}$$

where

$$A = \frac{\Psi}{2\sqrt{\alpha_c}}$$

In practice, the value of $\rho_g c_g$ is usually much less than $\rho_f c_f$ and so the last term in brackets in equation 30 can usually be neglected. Note that this solution converges to equation 17 when $A \to \infty$ [36], as expected. Also, this solution is consistent with solutions given above in section *B*, in that the infiltration front advances as $\Psi\sqrt{t}$ and is at the melting point of the metal T_M. Results from these sections therefore remain unaltered, save for a change in V_s which is now dictated by equation 30 instead of equation 17. This implies, in particular, that for the infiltration experiment considered here, heat losses ahead of the infiltration front (into the

preform) cannot be responsible for stoppage of the front during the course of the experiment. Figure 18 gives values for the term in brackets in equation 30 as a function of A, neglecting the contribution of $\rho_g c_g/\rho_f c_f$.

For case *A* above, namely when the fibers are initially at $T_f > T_M$, the same technique can be applied by equating the temperature and the heat flux at the infiltration front to derive the temperature in both the preform and the infiltrated composite. Similarly, the boundary condition of a constant temperature T_o along S_1 can be replaced with that of a very large cylindrical bath of metal at a fixed temperature T_o at $x \rightarrow -\infty$ with no greater difficulty. This assumption may be more realistic in several cases of practical interest, such as a squeeze casting operation.

D. Effect of non-instantaneous heat transfer to the fibers.

We now relax the assumption that heat transfer between the metal and fibers occurs instantaneously. We focus attention on the case where the preform temperature T_f is lower than the metal melting point T_M. In this case a fiber will heat up to the metal melting point in some finite time, $t-t_o$, where t_o is the time at which the metal first contacted the fiber. Similarly, the solid metal that forms does so in a finite time. Therefore the solid volume fraction along the length of the composite is now as depicted in Figure 19. In this section we calculate the position of the infiltration front with the

assumption of instantaneous heat transfer relaxed, and compare it to that obtained with the assumption invoked.

Consider the time, $t-t_o$, between when the fiber was first contacted by liquid metal and when it approximately reached its final temperature. Owing to the small diameter of most fiber reinforcements, we assume that temperature gradients within the fiber are negligible. The temperature of the fiber is then given by [37]:

$$\frac{T_M - T(t)}{T_M - T_f} = e^{\frac{-2h}{r_f c_f r_f}(t - t_o)} \tag{31}$$

To calculate the effect of non-instantaneous heat transfer on the infiltration behavior we integrate equation 11. However, unlike previous cases, the permeability K is now a function of position because the solidification of metal around the fibers is a function of position. The resulting equation, therefore, must be solved numerically:

$$\frac{dL}{dt} \int_0^L \frac{dx}{K(x)} = \frac{\Delta P_\mu}{\mu (1 - V_f)} \tag{32}$$

The integration of equation 32 provides an infiltration profile for the case of non-instantaneous heat transfer. Taking the ratio of this profile to that obtained for the case of instantaneous heat transfer provides a measure of the importance of this assumption. Figure 20 presents this ratio as a function of a dimensionless parameter, and also displays a time axis for

the case of pure aluminum and alumina fibers for a specific set of processing conditions.

V. NON-ADIABATIC UNIDIRECTIONAL INFILTRATION OF A SQUARE ARRAY OF FIBERS ALONG ONE OF ITS PRINCIPAL AXES; NEGLIGIBLE TEMPERATURE GRADIENTS TRANSVERSE TO THE FLOW DIRECTION

In the previous section we considered heat transfer and fluid flow within a preform thermally isolated from its surroundings; in this section we consider the additional effect of heat transfer to the surroundings by allowing heat flow to the mold through surface S_3.

Solid metal within the infiltrated preform may now originate from heat losses to the mold in addition to thermal exchange with the fibers. Since we are considering only the case of a pure metal in this work, solid forming as a result of heat losses to the mold will grow as a cylindrical shell emanating inwards from the mold surface. The problem is similar to the preceding case, except that flow can occur only within an inner "core" of the sample. The problem thus also involves the calculation of a new interface between fully solid and partially solid material, S_4; see Figure 1.

As above, we shall restrict the problem to simplified tractable cases. We consider the same preform but relax the assumption of an adiabatic mold/casting interface S_3. We add

the following assumptions: (i) the cylinder is circular of internal radius R_i, (ii) there is no heat exchange within the mold along the infiltration direction, (iii) the infiltrated portion is sufficiently long compared to the solidified layer of metal that flow remains essentially unidirectional, (iv) $T_o = T_M$ and $T_f \leq T_M$ (no metal superheat, cold fibers).

The infiltrated portion of the preform is now composed of a central core of semi-solid metal as before, with a volume fraction solid metal and a permeability given by the same equations as above. The outer portion of the infiltrated preform is fully solid, and extends from $R = R_c$ to $R = R_i$, where R_c is the radius of the semi-solid central core. At any location x along the preform axis, R_c is a decreasing function of time, given by the particular heat loss mechanism along S_3. Figure 21 schematically illustrates the solidification during infiltration. According to assumption (ii) above, R_c at x is solely a function of the time elapsed, Δt, since the metal first contacted the mold wall at x. The elapsed time can be written as:

$\Delta t(x) = t - L^{-1}(x)$, where $L^{-1}(x)$ is the reciprocal of the steadily increasing, and hence bijective, function $x = L(t)$. We can thus write :

$$R_c(x,t) = R_c\left(t - L^{-1}(x)\right)$$

From continuity, we have:

$$v_o R_c^2 = R_i^2 (1 - V_f) \frac{dL}{dt} \qquad (33)$$

From equations 7 and 33, after integration from x = 0 to x = L, we derive:

$$\frac{dL}{dt}\int_0^L \frac{dx}{\left[\frac{R_c\left(t - L^{-1}(x)\right)}{R_i}\right]^2} = \frac{K}{\mu\,(1 - V_f)}\,\Delta P_\mu \qquad (34)$$

This equation is the link between the infiltration front position L(t) and the applied pressure P_o (which can be a function of time in a more general context). The problem is defined with a specification of heat losses at the mold wall which, in turn, define $R_c(t)$. When R_c becomes zero (which necessarily occurs first at the preform entrance), choking occurs and the infiltration process stops. This determines the final infiltration length L_f.

Solutions of specific cases follow, given as a function of the assumed equation for $R_c(t)$. Some general dependencies can, however, be derived at this stage.

If $L_1(t) = n\,L_2(t)$, where n is a constant, we have :

$$\frac{dL_1}{dt}\int_0^{L_1} \frac{dx}{\left[\frac{R_c\left(t - L_1^{-1}(x)\right)}{R_i}\right]^2} = n^2\,\frac{dL_2}{dt}\int_0^{L_2} \frac{dx}{\left[\frac{R_c\left(t - L_2^{-1}(x)\right)}{R_i}\right]^2} \qquad (35)$$

Therefore, the position of the front at any time during the

infiltration process is proportional to:

$$\sqrt{\frac{K \Delta P_{\mu}}{\mu (1 - V_f)}}$$

independent of the heat loss mechanism along S_3. In what follows we will consider two limiting cases of heat transfer through surface S_3.

A. External heat loss through a mold of zero thickness; heat transfer limited by convection to the surroundings

For the case of a cylindrical mold, a radial temperature profile across the composite and mold is shown in Figure 22. In this case we have [8]:

$$\left[\frac{R_c}{R_i}\right]^2 = 1 - \frac{2 h_e (T_M - T_e)}{R_i (1 - V_{sf}) \rho_m \Delta H} t \qquad (36)$$

where h_e = heat transfer coefficient between metal and surrounding environment, and T_e is the temperature of the surroundings, assumed constant. Using equation 36, equation 34 can be numerically integrated to find infiltration length as a function of time, Figure 23. In addition, by integrating equation 34 to the point at which flow ceases, one can determine the effect of such process parameters as fiber temperature, fiber volume fraction and applied pressure on final infiltrated length, Figures 24, 25 and 26.

B. External heat loss through a mold of infinite thickness; heat transfer limited by conduction through the mold

For the case of a cylindrical mold, a radial temperature profile across the composite and mold is shown in Figure 27. In this case we have

$$\left[\frac{R_c}{R_i}\right]^2 = 1 - \frac{2(T_M - T_i)}{R_i(1 - V_f)\rho_m \Delta H}\sqrt{\frac{4\rho' c' k'}{\pi}}\sqrt{t} \qquad (37)$$

where k' = thermal conductivity of the mold, $\rho'c'$ = volumetric heat capacity of the mold, and T_i = initial temperature of the mold [38]. Integration of equation 34 using equation 37 yields the dependencies shown in Figures 28, 29, and 30.

VI. CONCLUSIONS

General expressions have been given to describe heat and fluid flow during infiltration of a fibrous preform by a pure metal. Analytical solutions have been given for the case of unidirectional infiltration into a preform of aligned fibers. Some conclusions of engineering importance are listed below.

a) For the case of fibers at a temperature below the metal melting point, pure metal will solidify as a sheath around the fibers. The processing parameter with the most significant effect on infiltration kinetics is the fiber

volume fraction. It is followed, in decreasing order of significance, by fiber temperature, applied pressure and metal superheat.

b) For the case of fibers at a temperature below the metal melting point, the effect of metal superheat is to remelt the solid metal sheath that has formed around the fibers. This occurs first at the fiber preform entrance and progresses towards the infiltration front. Although the remelting front progresses downstream as the infiltration front moves, the length of the remelted region always remains a fixed fraction of the total infiltration length, for the case of a constant applied pressure, no external heat extraction, and instantaneous heat transfer between the metal and fibers. The analytical solution obtained for this problem indicates a minor role of metal superheat on the infiltration kinetics.

c) For the case of fibers heated above the metal melting point, no external heat extraction, and constant applied pressure, flow through the preform will continue indefinitely. When external heat extraction is present, flow through the preform ceases when solidification from the external heat sink has progressed to the point where the flow channel has closed. This will occur first at the entrance to the fiber preform and can be predicted analytically for simple geometries. The final infiltrated length can then be predicted upon providing the external heat transfer kinetics.

d) Infiltration pressure does not effect the preform permeability. Therefore, under conditions of constant applied pressure, instantaneous heat transfer between the metal and fibers, and negligible capillary pressure, the effect of applied pressure on final infiltrated length is parabolic.

e) The effect of thermal losses ahead of the infiltration front is to increase the amount of solid metal that forms around the fibers. For the case of most fibers of engineering significance under practical processing conditions this effect is negligible.

f) The effect of non-instantaneous heat transfer between the metal and fibers is to delay the onset of solidification. For the case of most fibers of practical significance the delay is on the order of milliseconds; for larger diameter fibers of approximately 100μm, however, this delay can be on the order of a few seconds.

NOMENCLATURE

		Units
α_c	= thermal diffusivity of composite	m^2/s
α'	= thermal diffusivity of mold	m^2/s
μ	= viscosity of liquid metal	Pa s
ρ_f	= density of fiber	kg/m^3
ρ_m	= density of metal	kg/m^3
ρ'	= density of mold	kg/m^3
ρ_c	= density of composite	kg/m^3
ρ_g	= density of gas in interfiber regions of uninfiltrated preform	kg/m^3
c_f	= specific heat of fiber	J/kg K
c_m	= specific heat of metal	J/kg K
c'	= specific heat of mold	J/kg K
c_c	= specific heat of composite	J/kg K
c_g	= specific heat of gas in interfiber regions of uninfiltrated preform	J/kg K
g_s	= volume fraction of metal which has solidified	--
ΔH	= heat of fusion of metal	J/kg
h	= interfacial heat transfer coefficient between metal and fiber	W/m^2K
h_e	= interfacial heat transfer coefficient between metal and mold	W/m^2K
Ψ	= constant of proportionality between L and $\sqrt{t}$	$m/\sqrt{s}$
K	= permeability	m^2
k_c	= thermal conductivity of composite	W/m K

k_f	= thermal conductivity of fiber	W/m K
k_m	= thermal conductivity of metal	W/m K
k'	= thermal conductivity of mold	W/m K
L	= position of tip of liquid metal stream	m
L_f	= final infiltrated length of fiber preform	m
L_s	= position of remelted front	m
P	= pressure	Pa
P_a	= ambient pressure at flow tip of liquid metal stream	Pa
P_o	= applied pressure at entrance to preform	Pa
P_s	= pressure in liquid metal at remelted front	Pa
P_t	= pressure in liquid metal just behind flow tip	Pa
ΔP_T	= total pressure drop in liquid metal	Pa
ΔP_γ	= pressure drop in liquid metal due to surface tension	Pa
ΔP_μ	= pressure drop in liquid metal due to viscous drag	Pa
r_f	= radius of fiber	m
r_{sf}	= combined radii of fiber and solid metal sheath	m
R	= radius	m
R_o	= outside radius of mold	m
R_i	= inside radius of mold	m
R_c	= channel radius in mold at any time or position	m
t	= time	s
t_o	= time at which liquid metal enters a given volume element	s
Δt	= elapsed time from start of infiltration	s

T	= temperature	°C
T_e	= temperature of surroundings	°C
T_f	= initial temperature of fibers	°C
T_i	= initial temperature of mold	°C
T_o	= initial temperature of metal	°C
T_M	= melting point of pure metal	°C
ΔT_s	= metal superheat	°C
V_f	= volume fraction of fiber in volume element	--
V_L	= volume fraction of liquid metal in volume element	--
V_s	= volume fraction of solid metal in volume element	--
V_{sf}	= volume fraction of all solid material in volume element	--
v_o	= superficial velocity of liquid metal (average velocity the metal would have if no fibers were present)	m/s
v	= average velocity of liquid metal within the porous medium	m/s
x	= position in the liquid stream behind the tip	m

REFERENCES

1. J.D. Kidd: *Tech Update, American Metal Market*, August 2, 1982.
2. A. Mortensen, J.A. Cornie, and M.C. Flemings: in *Proc. Conf. Mechanical Properties of Aluminum Castings*, May 1987, American Foundrymen's Society.
3. Sabri Ergun: *Chem. Eng. Prog.*, 1952, vol.48, pp.89-94.
4. V. Stanek and J. Szekely: *AIChE Journal*, 1974, vol.20, pp.974-980.
5. G.W.Jackson and D.F.James: *Can. J.of Chem. Eng.*, 1986, vol.64, pp.364-374.
6. J.E.Drummond and M.I. Tahir: *Int. J. Multiphase Flow*, 1984, vol.10, pp.515-540.
7. A.S. Sangani and A. Acrivos: *Int. J. Multiphase Flow*, 1982, vol.8, pp.193-206.
8. D.V. Ragone, C.M. Adams, and H.F. Taylor: *Trans. AFS*, 1956, vol.64, pp.640-652.
9. M.C. Flemings, C.M. Adams, E.E. Hucke, and H.F. Taylor: *Trans. AFS*, 1956, vol.64, pp.636-639.
10. J.E. Niesse, M.C. Flemings, and H.F. Taylor: *Trans. AFS*, 1959, vol.67, pp.685-697.
11. M.C. Flemings, F.R. Mollard, E.F. Niyama, and H.F. Taylor: *Trans. AFS*, 1962, vol.70, pp.1029-1039.
12. M.C. Flemings: in *Proc. 30th World Foundry Congress*, Prague, 1963, pp.61-81.

13. S. Nagata and K. Matsuda: *IMONO*, 1981, vol.53, pp.300-304.

14. S. Nagata and K. Matsuda: *Trans. Japan Foundrymen's Soc.*, 1983, vol.2, pp.616-620.

15. F.M. Hosking and A.A. Netz: Sandia National Laboratory Report No.SAND83-2573, 1983.

16. H. Fukunaga and K. Goda: *J. of Japan Inst. of Metals*, 1985, vol.49, pp.78-83.

17. H. Fukunaga and K. Goda: *Bull. of JSME*, 1984, vol.27, pp.1245-1250.

18. F. Girot, J.P. Rocher, J.M. Quenisset and R. Naslain: in *Proc. Conf. Eur. MRS*, P. Lamicq, W.J.G. Bunk, and J.G. Wurm, eds., Strasbourg, France, 1985, pp.129-133.

19. T.W. Clyne: in *Proc. Sixth Int. Conf. Composite Materials (ICCM6)*, F.L. Mathews, N.C.R. Buskell, J.M. Hodgkinson, and J. Morton, eds., Elsevier Applied Science, 1987, pp.2.275-2.286.

20. T.W. Clyne and M.G. Bader: in *Proc. Fifth Int. Conf. Composite Materials (ICCM5)*, W.C. Harrigan, J. Strife, and A.K. Dhingra, eds., TMS-AIME, 1985, pp.755-771.

21. T.W. Clyne and J.F. Mason: *Metall. Trans. A*, 1987, vol.18A, pp.1519-1530.

22. A.E. Scheidegger: *The Physics of Flow through Porous Media, third edition*, University of Toronto Press, Toronto, Canada, 1974, p.78.

23. R.B. Bird, W.E. Stewart, and E.N. Lightfoot: *Transport Phenomena*, John Wiley & Sons, New York, NY, 1960, p.316.

24. H.S. Carslaw and J.C. Jaeger: *Conduction of Heat in Solids*, Oxford University Press, Oxford, England, 1959, p.38.

25. M.C. Flemings: *Soldification Processing*, McGraw-Hill, Inc., New York, NY, 1974, pp.1-30.

26. E. Behrens: *J. Comp. Materials*, 1968, vol.2, pp.2-17.

27. H. Hatta, M. Taya, and F.A. Kulacki: in *Proc. Fifth Int. Conf. Composite Materials (ICCM5)*, W.C. Harrigan, J. Strife, and A.K. Dhingra, eds., TMS-AIME, 1985, pp.1667-1681.

28. W.T. Perrins, D.R. McKenzie, and R.C. McPhedran: *Proc. R. Soc. Lond. A*, 1979, vol.369, pp.207-225.

29. S. Nomura and T-W Chou: *J. Comp. Materials*, 1980, vol.14, pp.120-129.

30. J.R. Willis: *J. Mech. Phys. Solids*, 1977, vol.25, pp.185-202.

31. A. Mortensen and J.A. Cornie: *Metall. Trans. A*, 1987, vol.18A, pp.1160-1163.

32. Julian Szekely: *Fluid Flow Phenomena in Metals Processing*, Academic Press, New York, NY, 1979, p.256.

33. A.E. Scheidegger: *ibid.*, p.154.

34. O.P. Bergelin, G.A. Brown, H.L. Hull, and F.W. Sullivan: *Trans. ASME*, 1950, vol.71, pp.881-888.

35. G.H. Geiger and D.R. Poirier: *Transport Phenomena in Metallurgy*, Addison-Wesley Publishing Company, Reading, MA, 1973, p.94.

36. H.S. Carslaw and J.C. Jaeger: *ibid.*, p.482.

37. G.H. Geiger and D.R. Poirier: *ibid.*, p.291.

38. M.C. Flemings: *ibid.*, p.12.

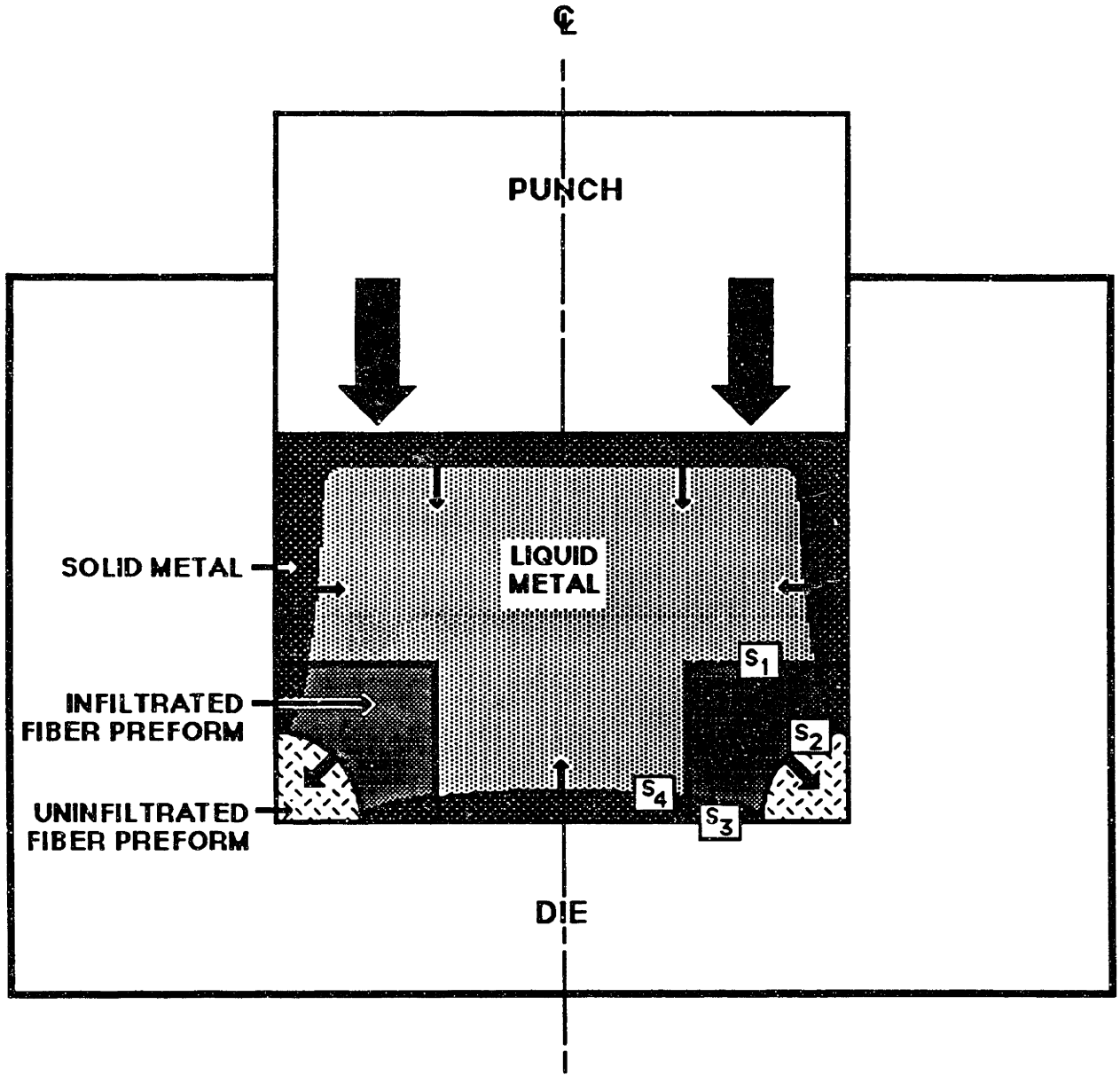

Figure 1: Generalized three-dimensional problem of infiltration of a fibrous preform. In this case, the part is a simplified version of a selectively reinforced piston fabricated by squeeze casting.

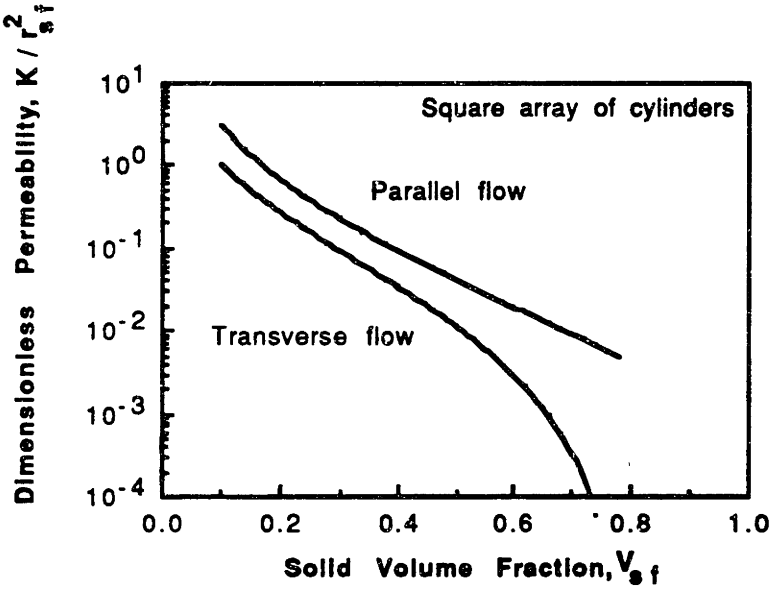

Figure 2: Dimensionless permeability through a square array o parallel fibers, for creeping flow parallel and perpendicular to the fiber axis, from equations 1 and 2.

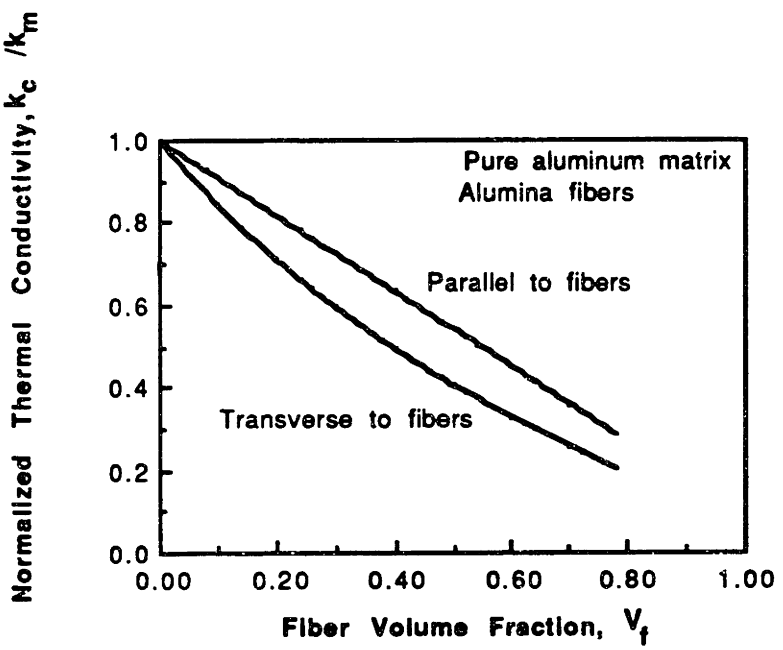

Figure 3: Plot of normalized thermal conductivity of the composite as a function of fiber volume fraction parallel and perpendicular to the fiber axis. For an array of aligned alumina fibers, from equations 3 and 4.

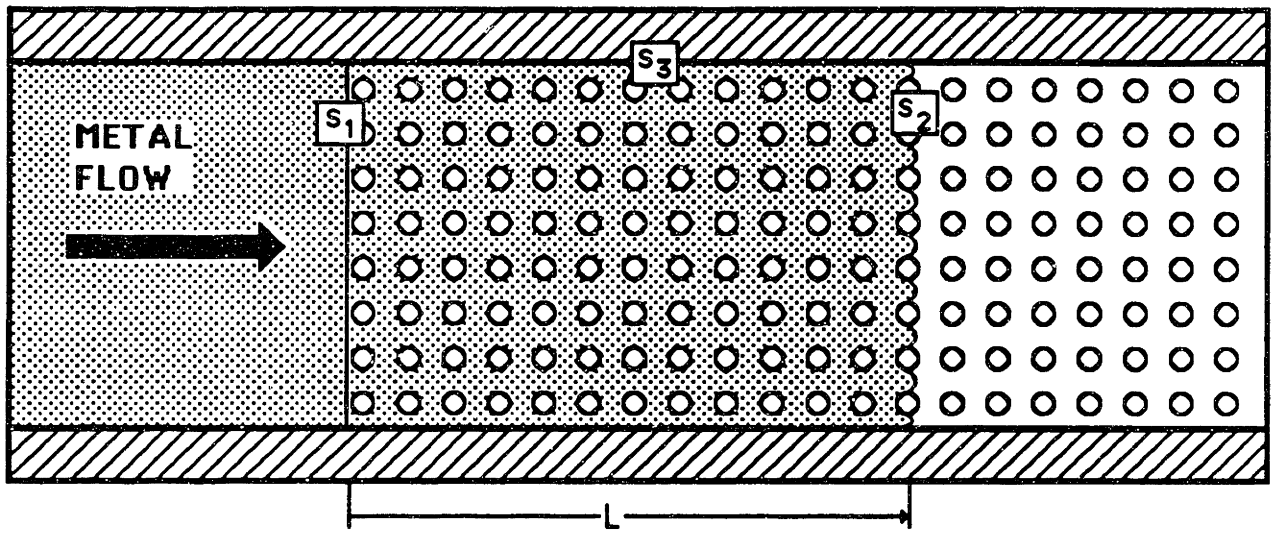

Figure 4: Schematic drawing of fiber preform in unidirectional crossflow.

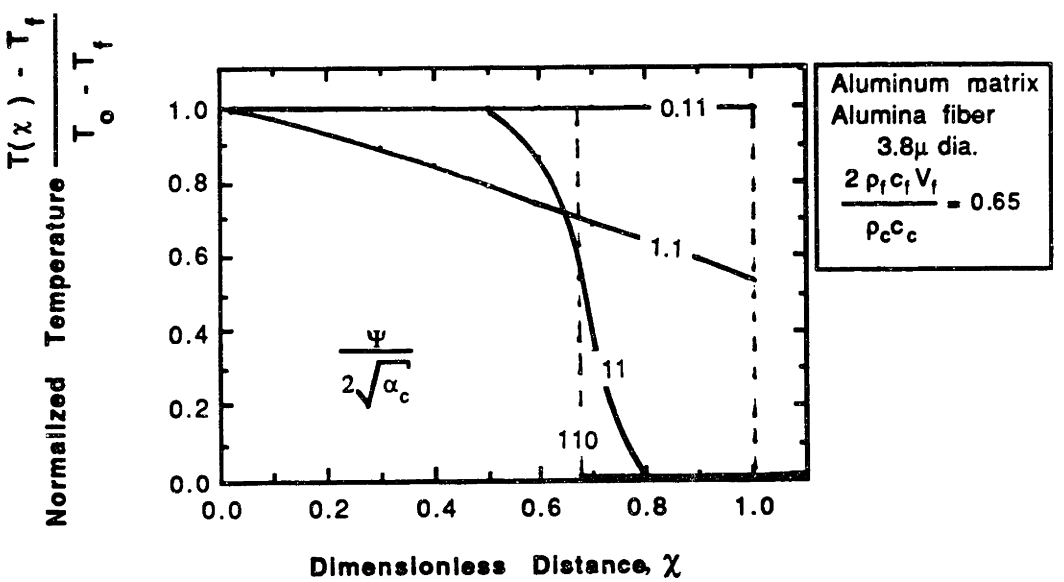

Figure 5: Normalized temperature profile within the infiltrated composite for the case of fibers heated at or above metal melting point. For an aluminum matrix reinforced with 24 volume percent alumina fibers; infiltration perpendicular to the fiber axis. From equation 19.

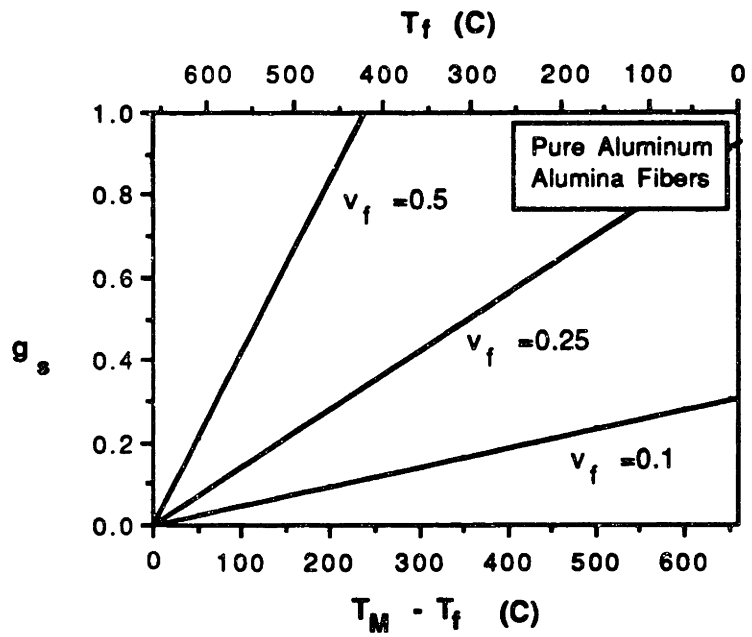

Figure 6: Plot of fraction solidified within the metal matrix during infiltration as a function of fiber temperature and volume fraction. For aluminum matrix and alumina fibers, from equation 17.

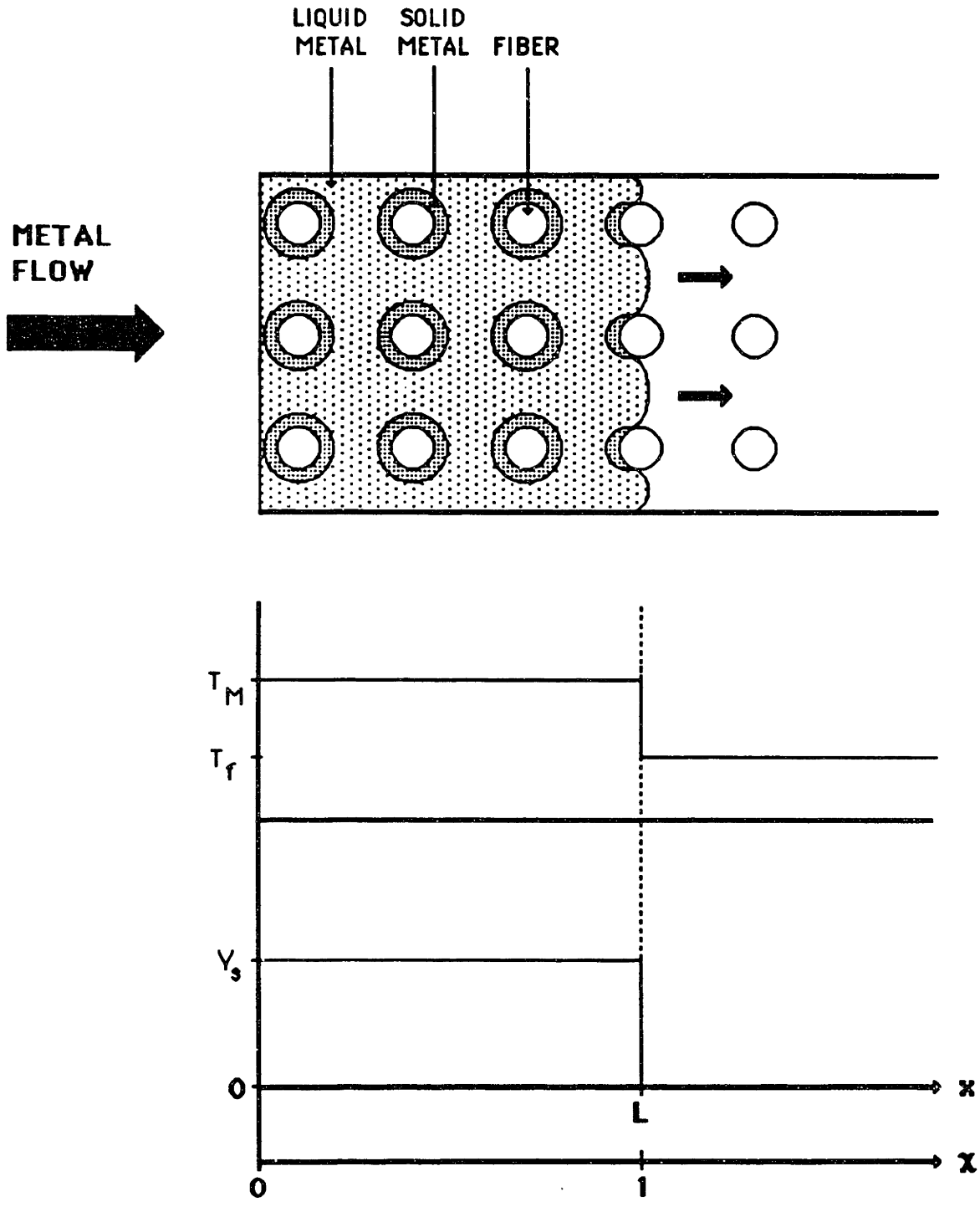

Figure 7: Schematic drawing of transverse flow and solidification within the fiber preform for the case of fibers heated below the metal melting point and no metal superheat. Also shown are the temperature and solid metal profiles.

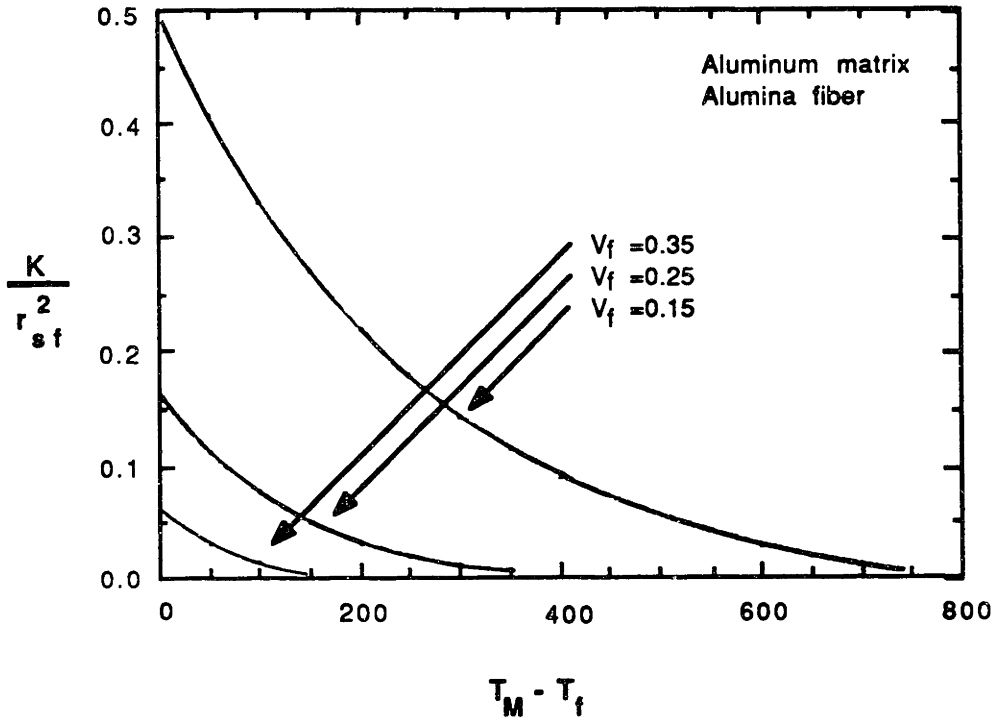

Figure 8: Dependence of dimensionless permeability K/r_{sf}^2 on fiber temperature and fiber volume fraction for alumina fibers infiltrated in cross-flow by aluminum. From equations 1 and 20; no metal superheat.

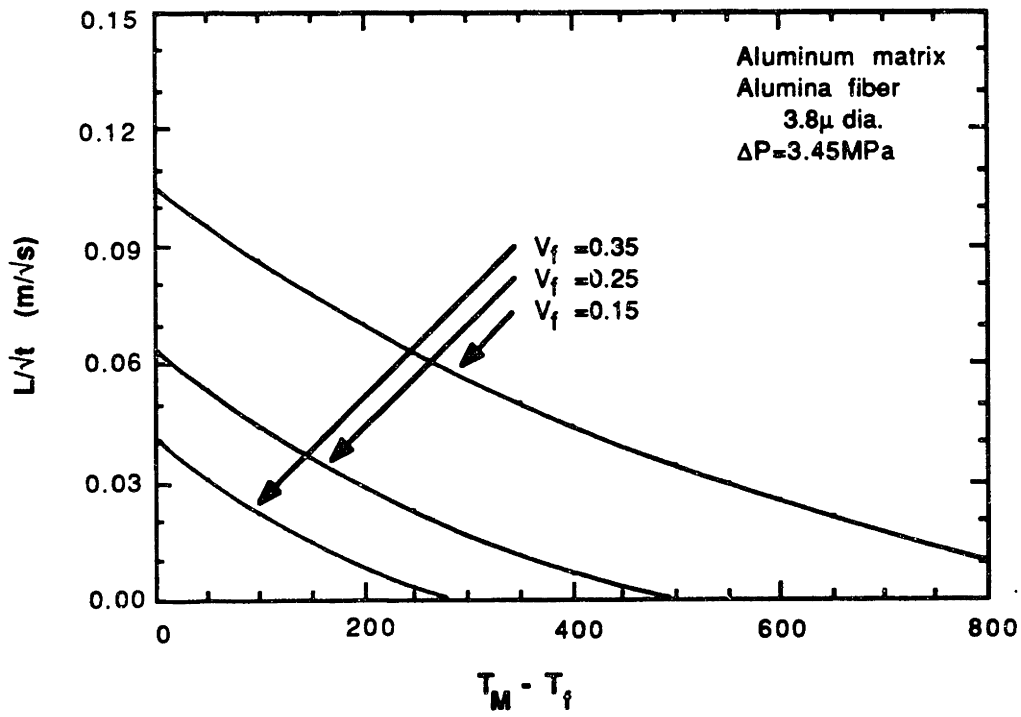

Figure 9: Dependence of $L/\sqrt{t}$ on fiber volume fraction and fiber temperature for alumina fibers infiltrated in cross-flow by aluminum. From equation 22; no metal superheat, no capillary pressure.

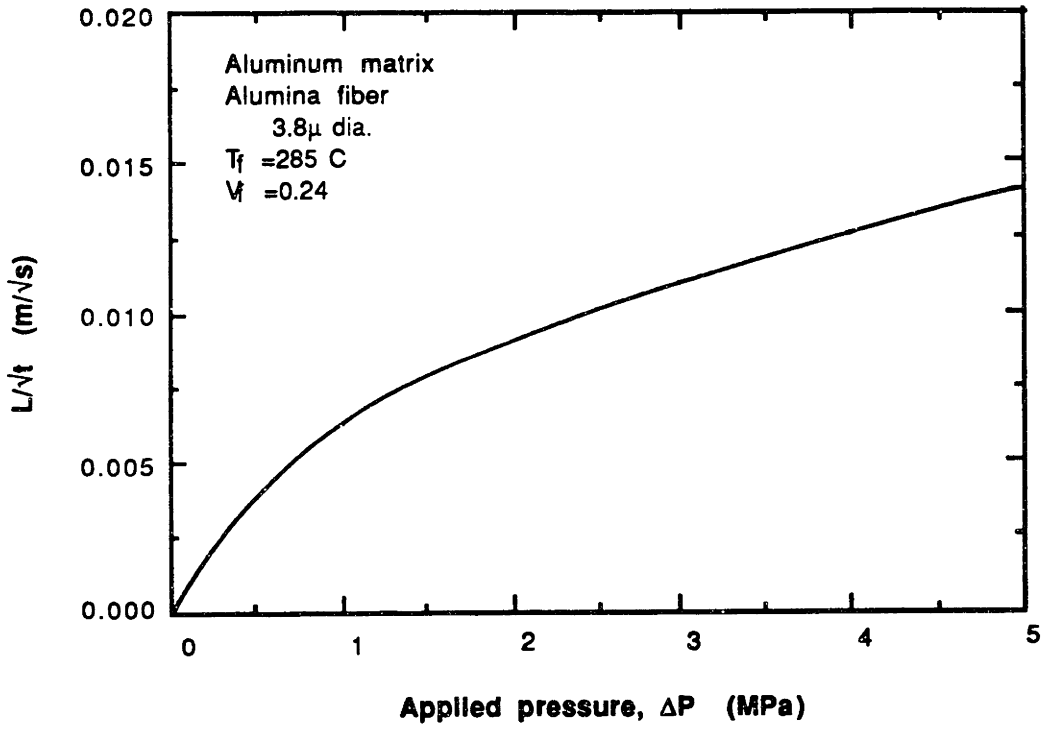

Figure 10: Dependence of $L/\sqrt{t}$ on applied pressure for alumina fibers infiltrated in cross-flow by aluminum. From equation 22; no metal superheat, no capillary pressure.

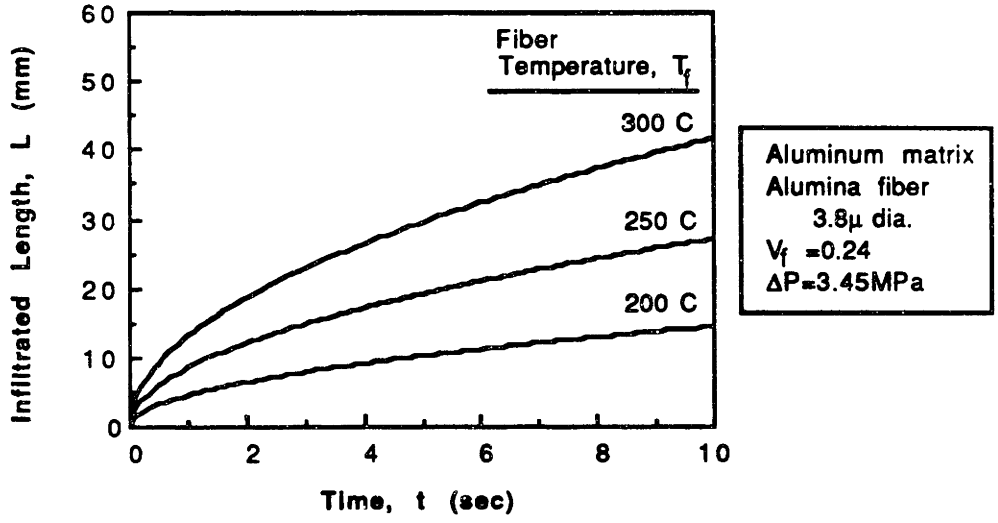

Figure 11: Infiltration length as a function of time for alumina fibers infiltrated in cross-flow by pure aluminum. This plot also shows the effect of fiber temperature. From equation 22; no metal superheat.

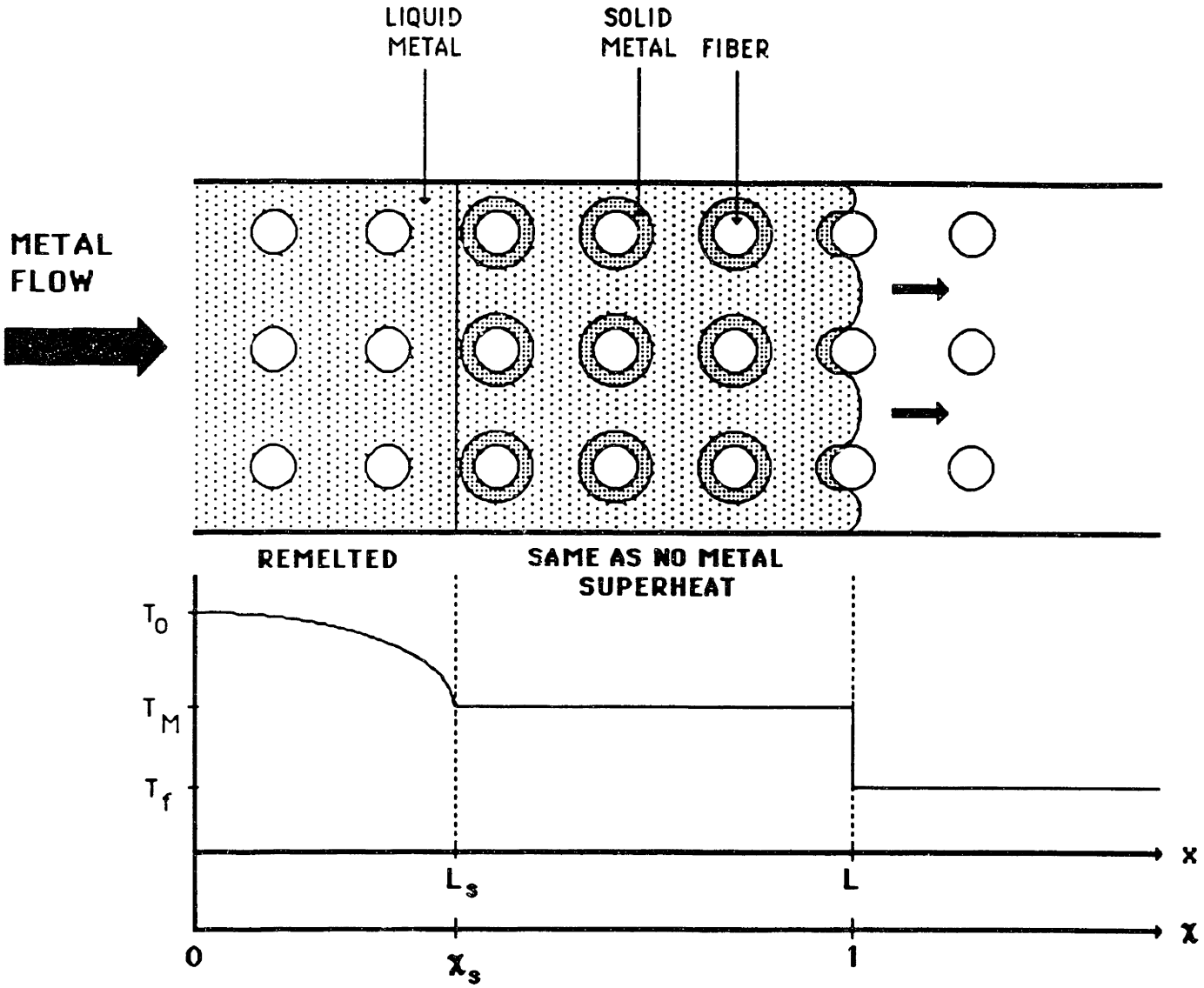

Figure 12: Schematic drawing of the remelted region caused by metal superheat for the case of fibers heated below the metal melting point and for transverse flow. Also included is the associated temperature profile.

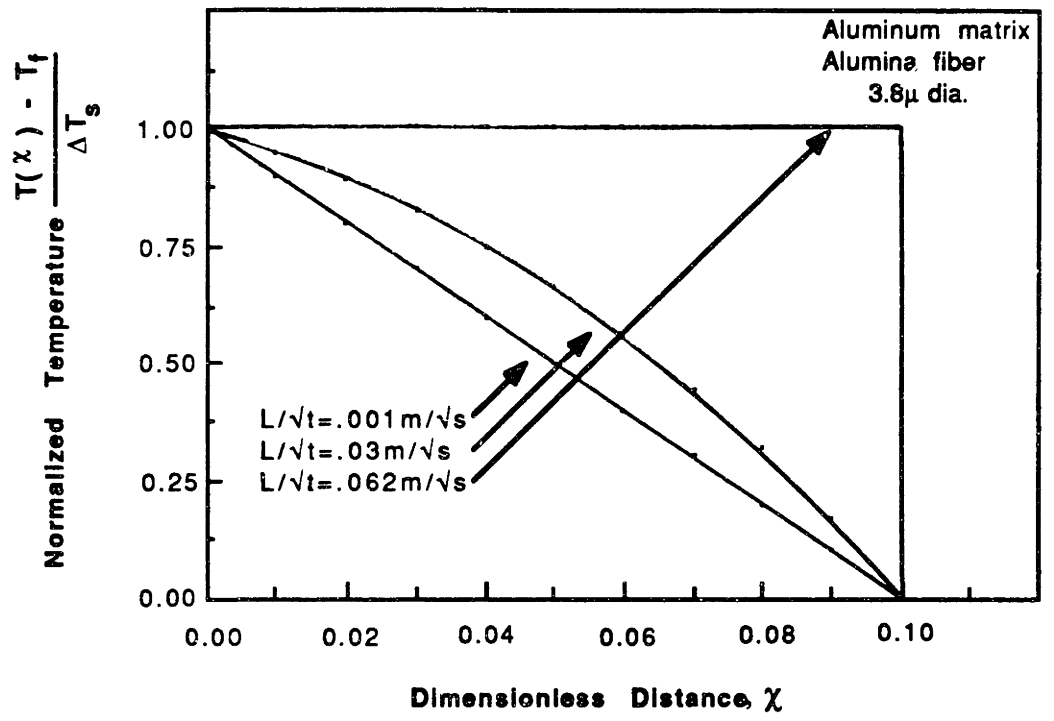

Figure 13: Normalized temperature profiles within the remelted region for an aluminum matrix reinforced with 24 volume percent alumina fibers; infiltration perpendicular to the fiber axis. For a remelted region extending into 10% of the total infiltrated length; from equation 23.

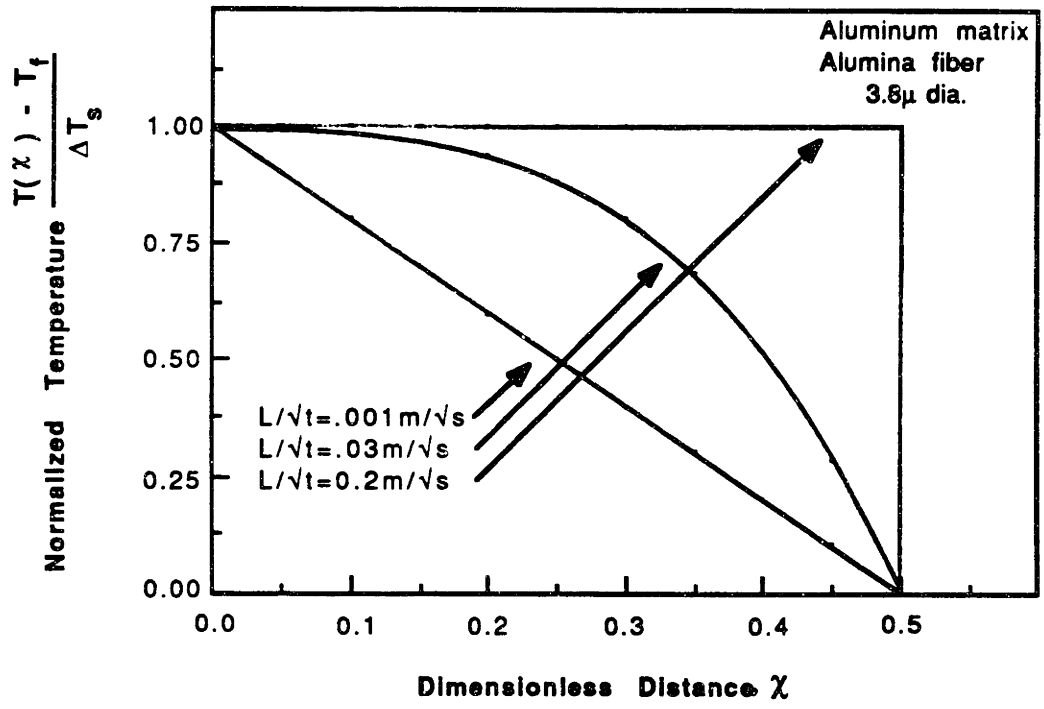

Figure 14: Normalized temperature profiles within the remelted region for an aluminum matrix reinforced with 24 volume percent alumina fibers; infiltration perpendicular to the fiber axis. For a remelted region extending into 50% of the total infiltrated length; from equation 23 .

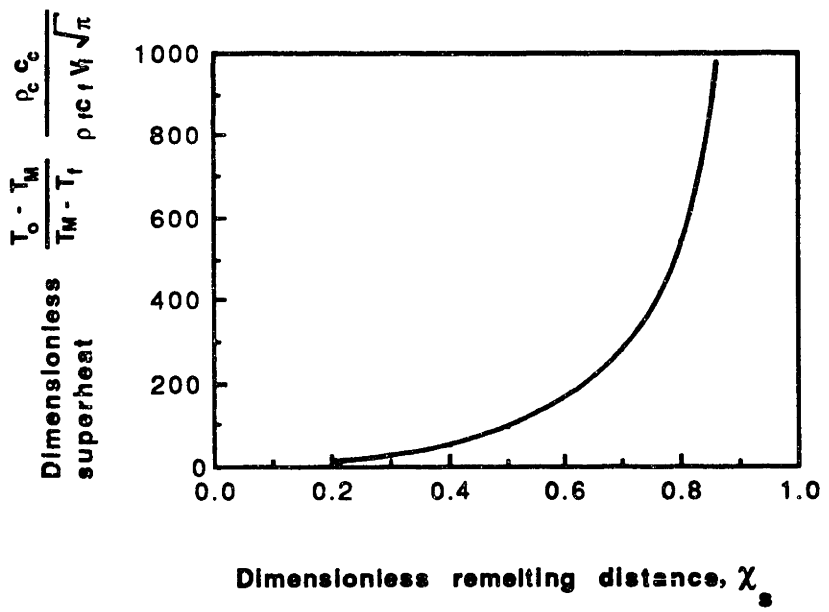

Figure 15: Graphical solution for χ_s from equation 25. For an aluminum matrix reinforced with aligned fibers; infiltration perpendicular to the fiber axis.

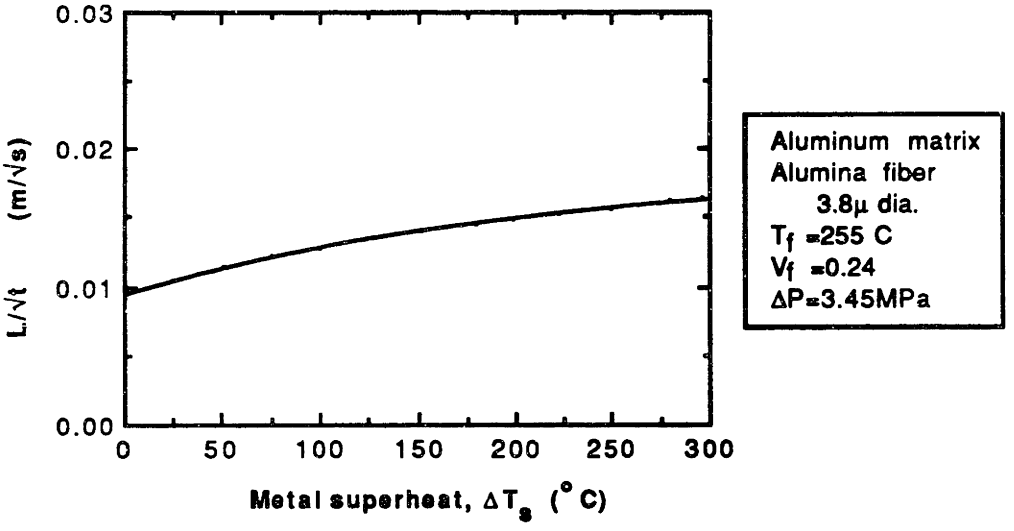

Figure 16: Dependence of $L/\sqrt{t}$ on metal superheat for alumina fibers infiltrated in cross-flow by aluminum. From equations 25 and 26.

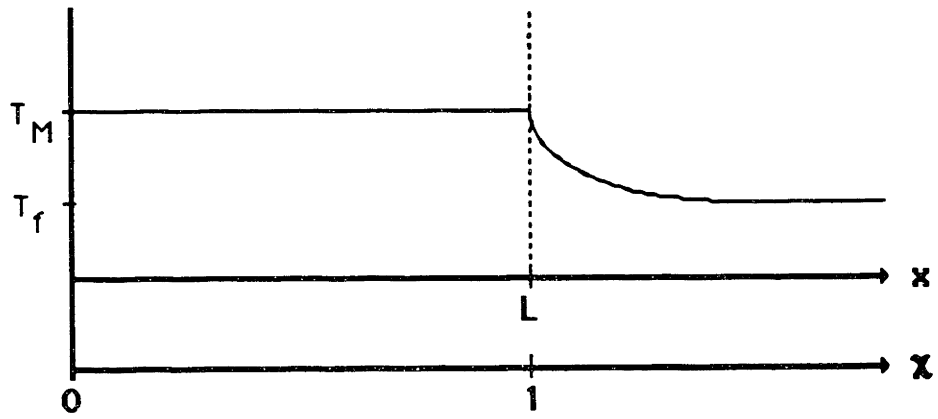

Figure 17: Schematic temperature profile through the fibers for the case when the fibers conduct heat ahead of the infiltration front

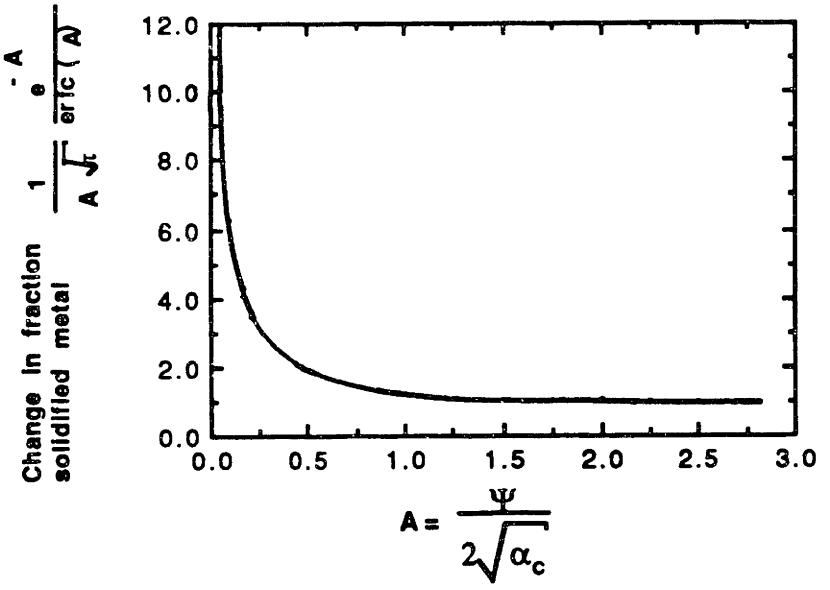

Figure 18: Plot of change in fraction solidified metal as a function of A for the case when thermal conduction occurs ahead of the infiltration front, equation 30.

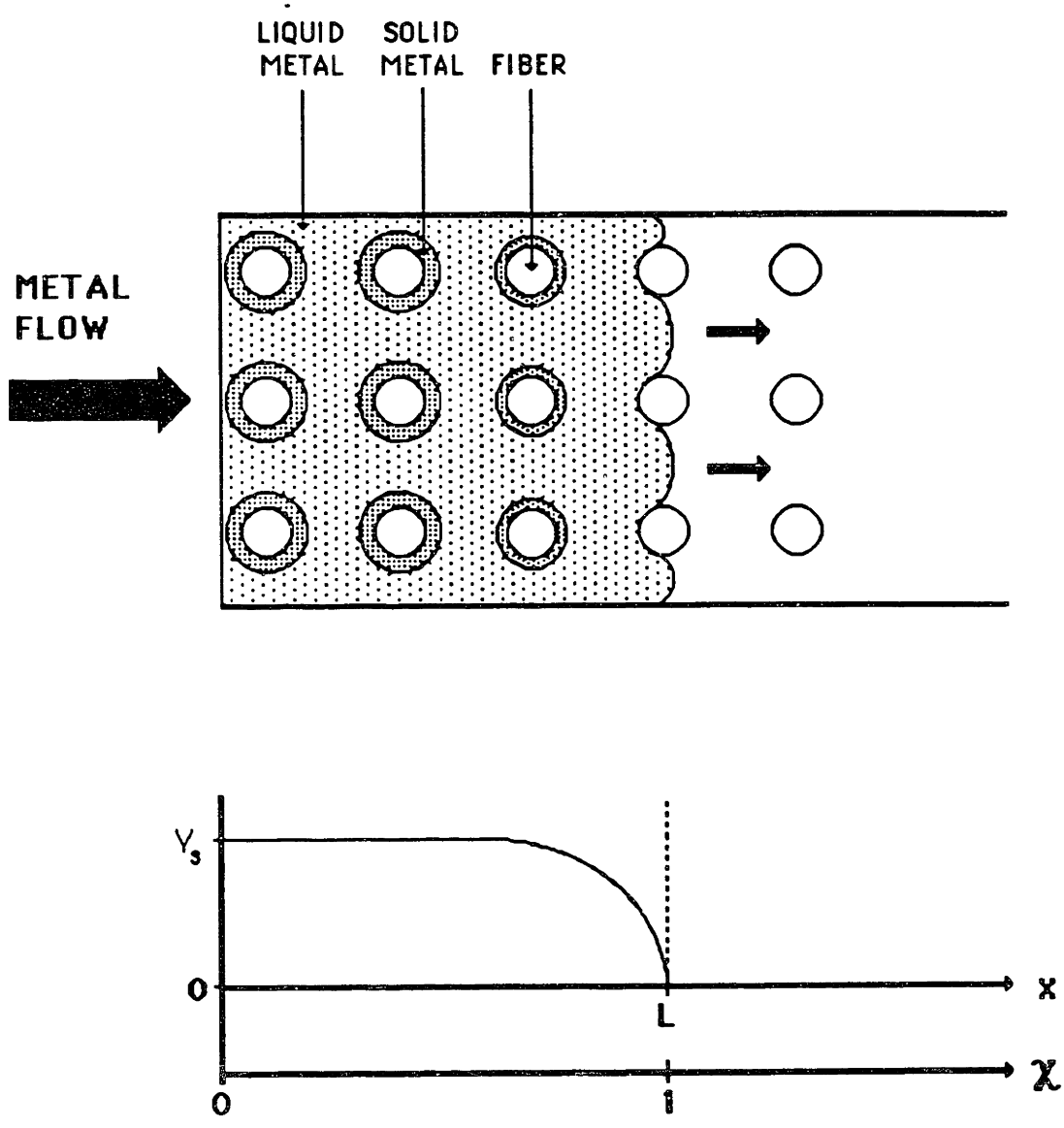

Figure 19: Schematic drawing of the effect of non-instantaneous heat transfer between metal and fibers.

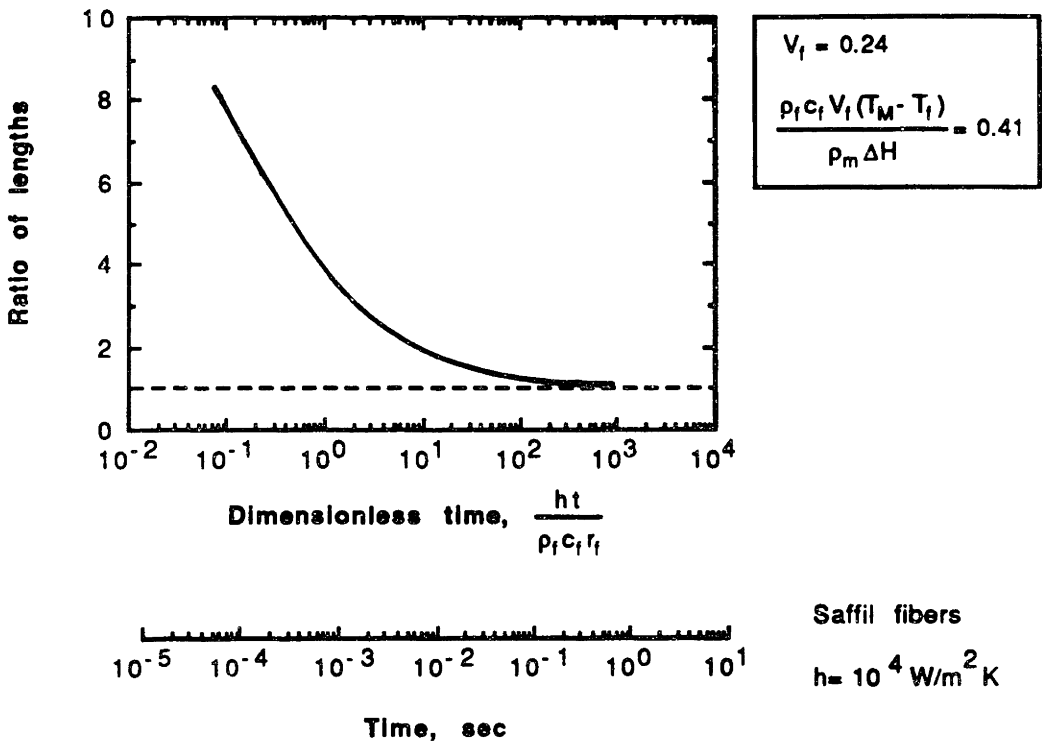

Figure 20: Ratio of length obtained for case of non-instantaneous heat transfer between metal and fibers to that obtained for case of instantaneous heat transfer, plotted as a function of dimensionless time. When the ratio falls to approximately unity the difference between non-instantaneous and instantaneous cases is negligible. Also superimposed is a time scale for the case of Saffil fibers and a specific heat transfer coefficient.

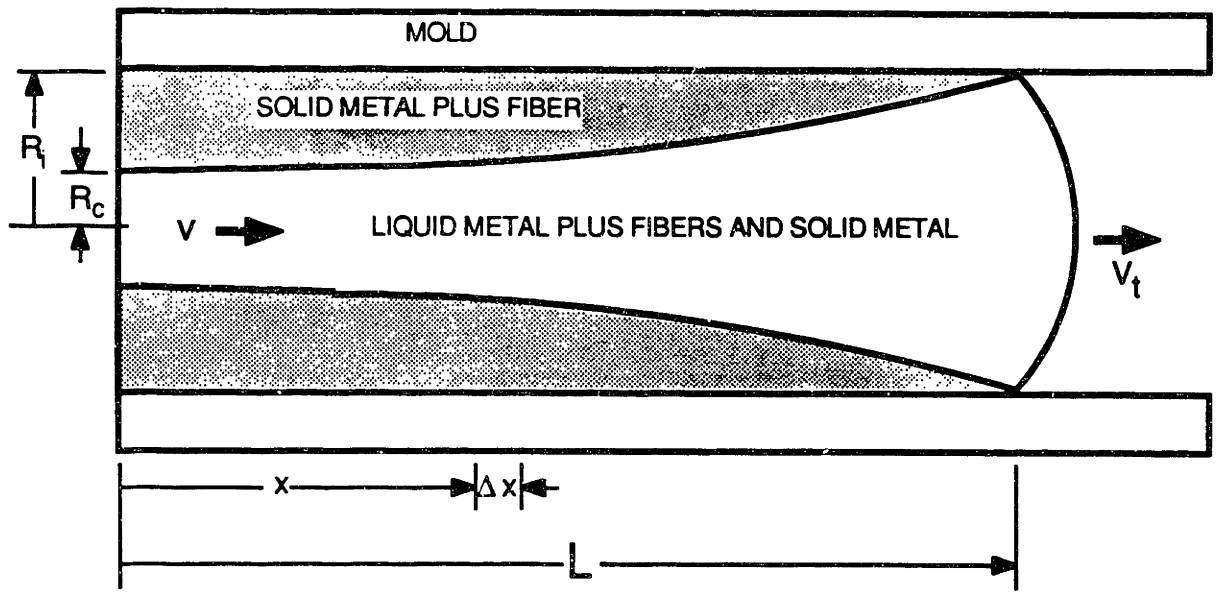

Figure 21: Schematic drawing of solidification due to external heat losses during infiltration.

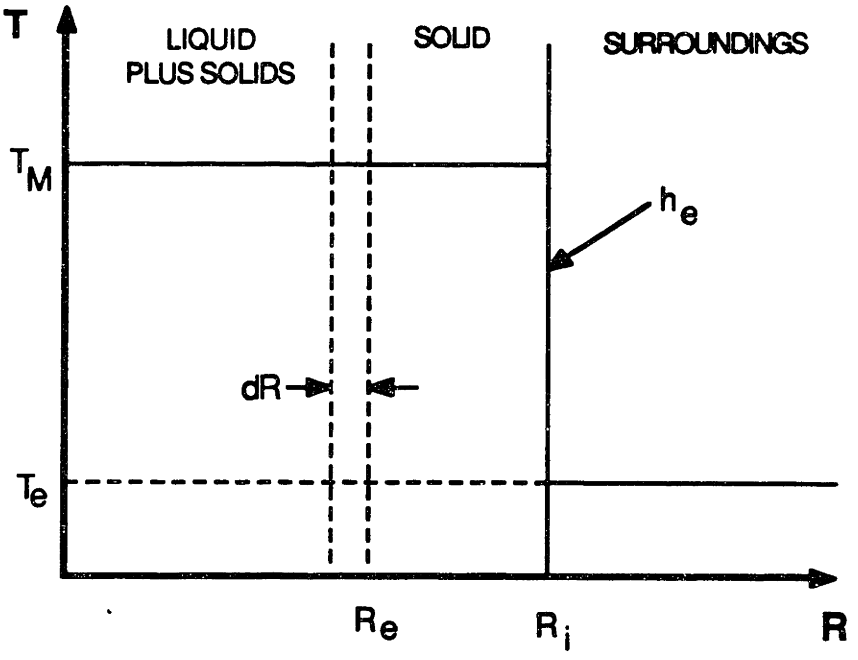

Figure 22: Radial temperature profile across the composite and mold plus casting for case of interface controlled heat transfer.

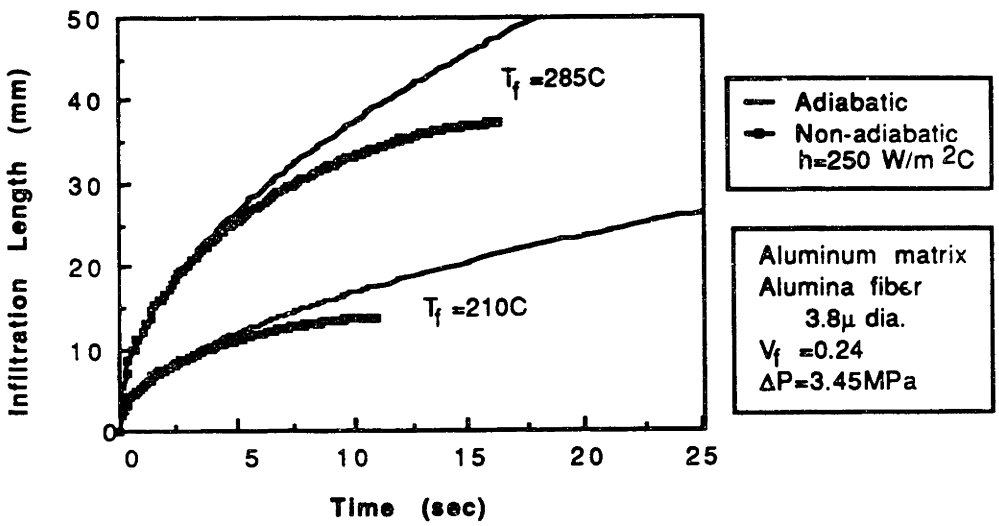

Figure 23: Infiltration length as a function of time for alumina fibers infiltrated in cross flow by pure aluminum. Non-adiabatic model, equations 36 and 34, is shown for one value of h and is compared to the adiabatic model, equation 22.

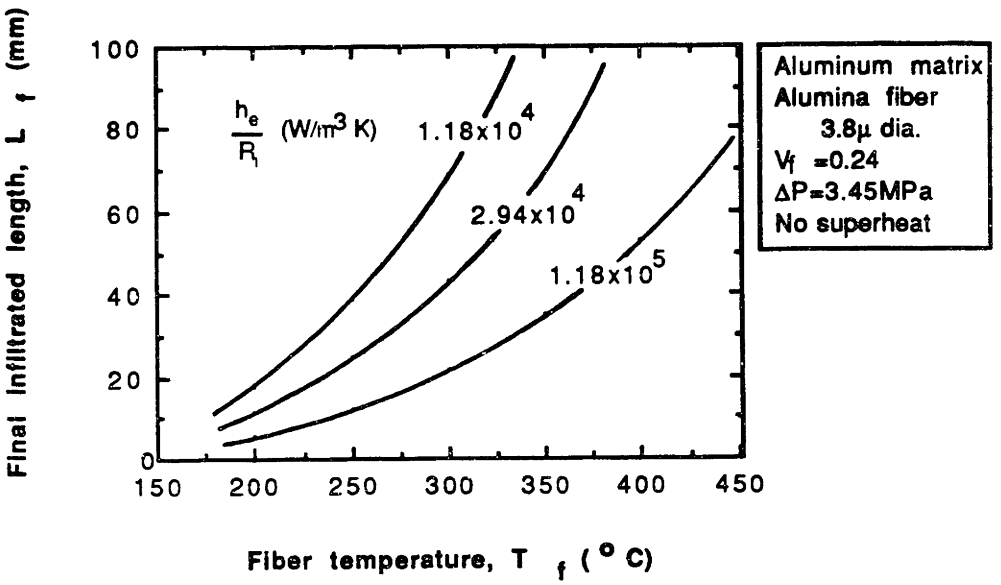

Figure 24: Plot of the effect of fiber temperature on final infiltrated length for the case of external heat loss controlled by convection, equations 34 and 36. For mold temperature same as fiber temperature.

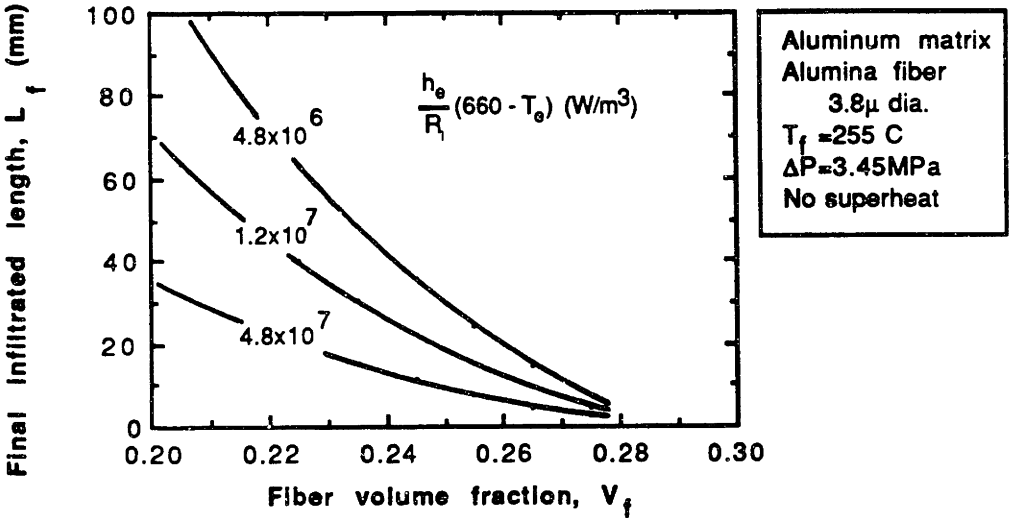

Figure 25: Plot of the effect of fiber volume fraction on final infiltrated length for the case of external heat loss controlled by convection, equations 34 and 36.

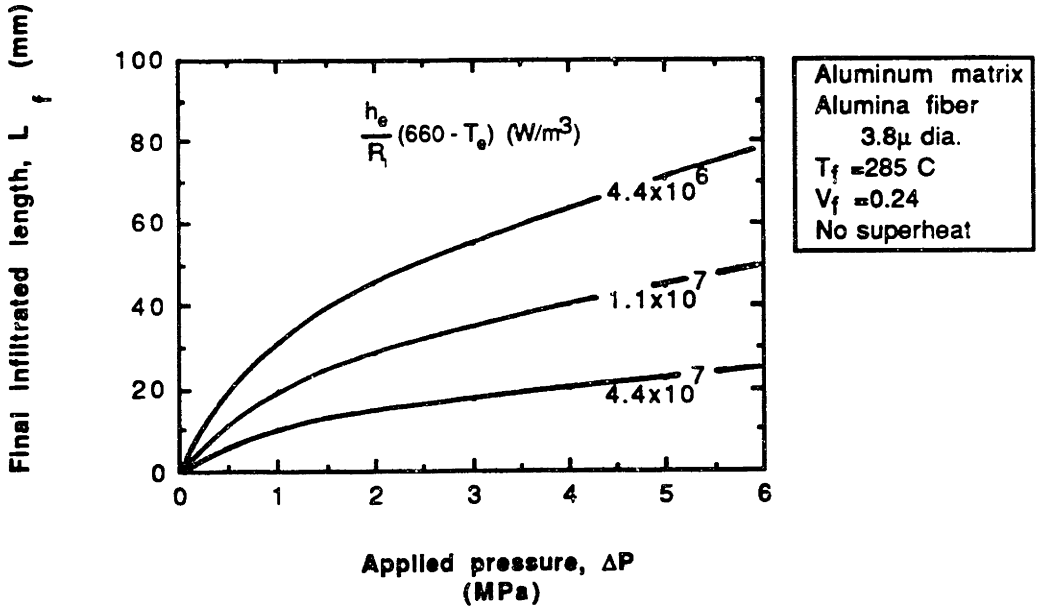

Figure 26: Plot of the effect of applied pressure on final infiltrated length for the case of external heat loss controlled by convection, equations 34 and 36 .

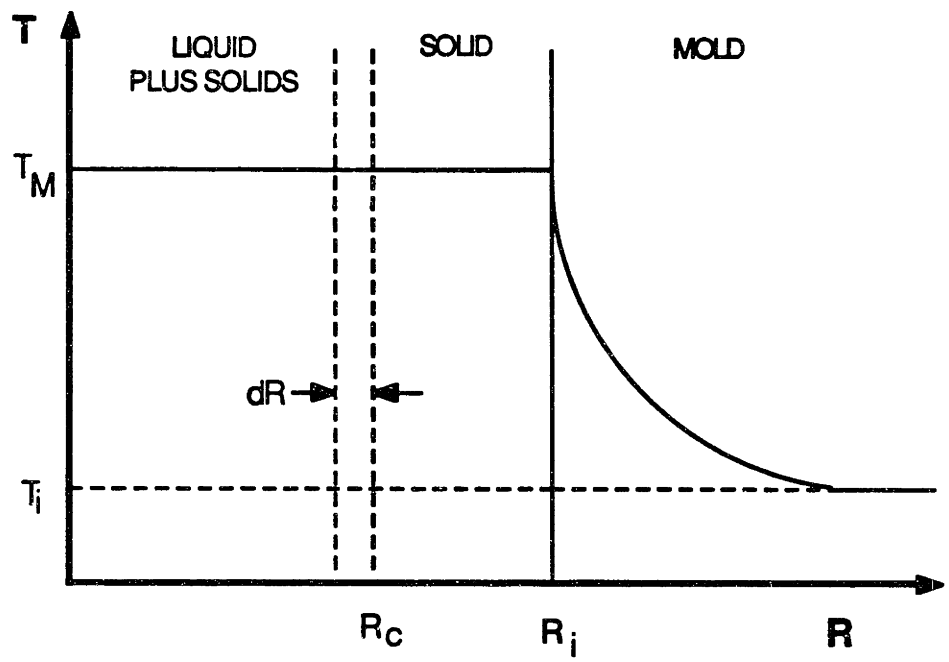

Figure 27: Radial temperature profile across the composite and mold for case of conduction controlled heat transfer.

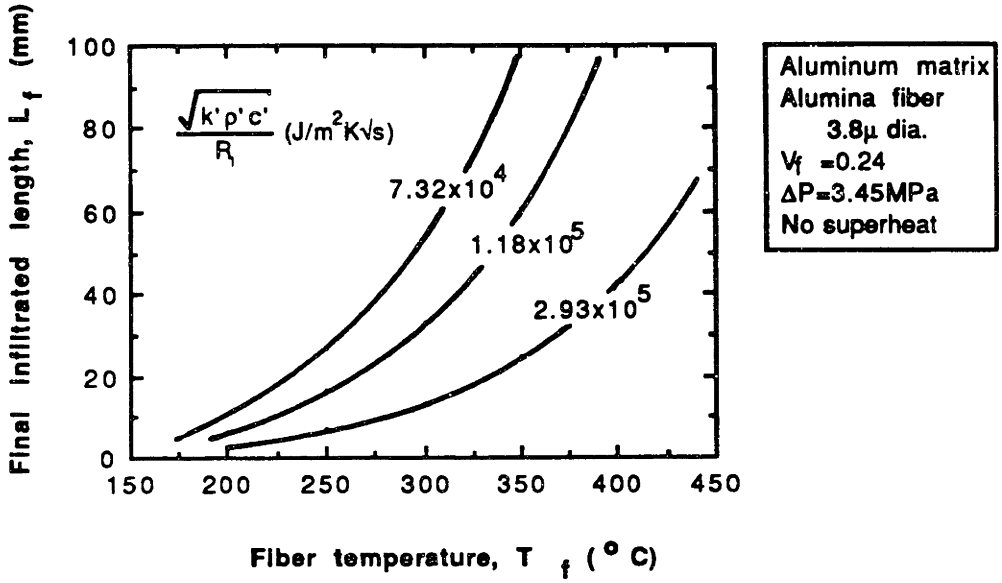

Figure 28: Plot of the effect of fiber temperature on final infiltrated length for the case of external heat loss controlled by conduction, equations 34 and 37 . For mold temperature same as fiber temperature.

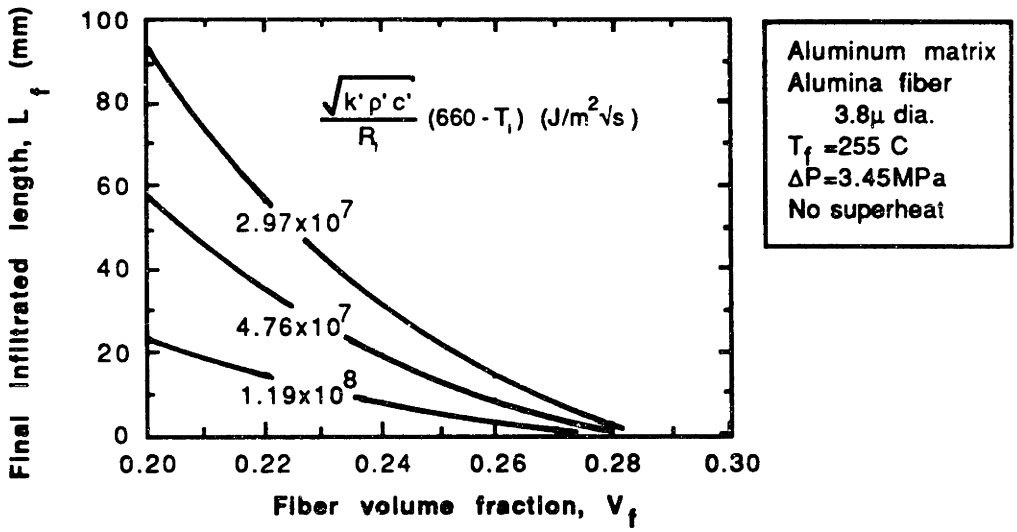

Figure 29: Plot of the effect of fiber volume fraction on final infiltrated length for the case of external heat loss controlled by conduction, equations 34 and 37.

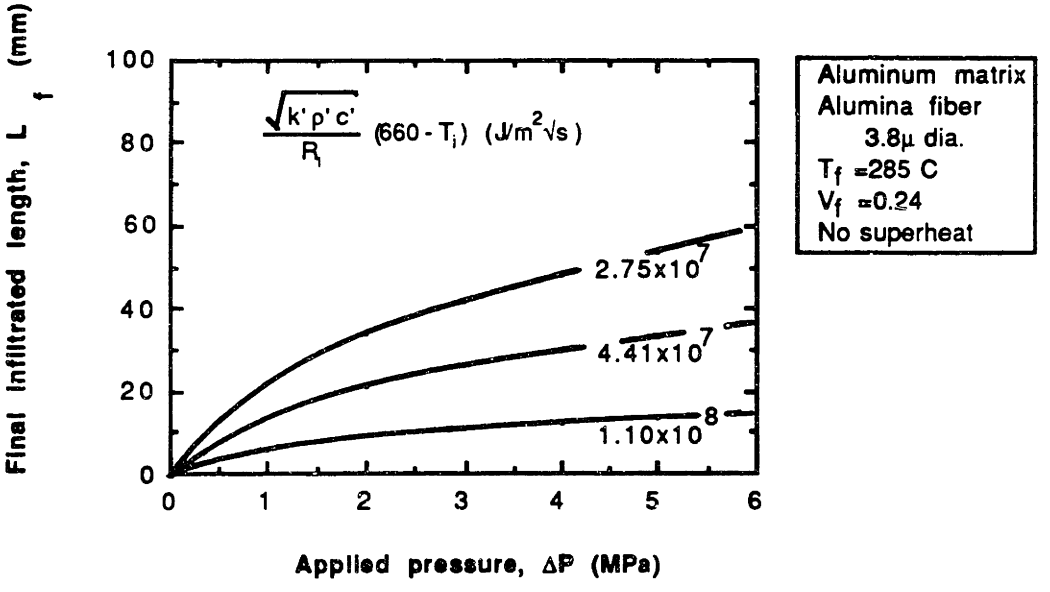

Figure 30: Plot of the effect of applied pressure on final infiltrated length for the case of external heat loss controlled by conduction, equations 34 and 37 .

Chapter 2

INFILTRATION OF FIBROUS PREFORMS BY A PURE METAL

PART II: EXPERIMENT

I. INTRODUCTION

In the previous chapter [1] analytical solutions were given to describe the unidirectional infiltration of a pure metal into a preform of aligned fibers under the application of a constant pressure. In particular, the influence on infiltration kinetics was shown for the processing parameters of: a) fiber volume fraction, b) fiber temperature, c) metal superheat, and d) applied pressure. The interaction between the flowing metal and fibers for the case of fibers heated below the metal melting point was shown to be the solidification of solid metal to form a sheath surrounding the fibers. Also, it was shown that the effect of metal superheat, if present, was to remelt this solid metal sheath. The cessation of fluid flow was shown to be due to solidification from the mold wall progressing inwards and closing the flow channel. Calculations were performed to predict the behavior of pure aluminum infiltrating alumina fibers in cross flow under a variety of experimental conditions.

In this chapter experiments are presented to test the results of the foregoing calculations. All experiments were performed with alumina fibers and aluminum metal ranging in purity from 99.9% to 99.999%. The experiments were performed for the case of the fibers at a temperature below the metal melting point, which is the case of practical interest for the fabrication of fiber-reinforced diesel engine pistons, for example.

II. EXPERIMENTAL APPARATUS AND PROCEDURE

A. Fiber preform preparation

Saffil™ fibers were obtained from Imperial Chemical Industries, London, England. Saffil™ is a nominally 3μm diameter, delta-alumina fiber that is chopped and pressed into disk shaped preforms. The preform fabrication operation tends to align the fiber axes perpendicular to the pressing direction, resulting in a two-dimensional random arrangement of fibers. The preforms used in this study were 100mm diameter by 15mm thick and nominally 24% dense by volume. Figure 1 is an electron micrograph showing a typical Saffil preform prior to infiltration.

Cylindrical plugs were cut from the mother preform using a knife-edged cutter 17mm in internal diameter. These plugs were then tightly fitted into quartz tubes 17mm in internal diameter and 1mm in wall thickness. Their orientation was such that

metal infiltration was perpendicular to the fiber axis. In these experiments either two or three plugs were placed atop one another within the quartz tube, resulting in fiber preforms 30mm or 45mm in length. Finally, a ceramic support rod was placed on top of the preforms to prevent them from moving upwards in the quartz tube during infiltration. Figure 2 schematically illustrates the preform preparation process.

Each plug cut from the preform was weighed to calculate fiber volume fraction. It was discovered that plugs taken from the outer periphery of a preform were approximately 10% greater in fiber volume fraction than those taken from the center. When choosing a group of plugs for an experiment it was ensured that the fiber volumes were within 0.5 volume percent of one another. In this study the fiber volume percent ranged from 22.5% to 25.5%.

Selected preforms (chosen at random for each batch of raw materials) were further characterized by a water permeability test (see Table III). In this test a falling head permeability apparatus, Figure 3, was used to measure the preform permeability, K, from the following equation [2]:

$$K(m^2) = 1.02 \times 10^{-7} \frac{L}{t_1 - t_o} \ln\frac{h_o}{h_1} \qquad (1)$$

where h_o is the water height at time t_o, h_1 is the water height at time t_1, and L is the length of the preform in meters.

B. Pressure infiltration apparatus

Figure 4a is a schematic drawing of the pressure caster that was constructed specifically for this study. Unlike most pressure casters, this apparatus uses pressurized gas to cause infiltration rather than a mechanical piston. Consequently, the apparatus is designed as a pressure vessel with various feedthroughs for power, control, et cetera.

The fiber-filled quartz tube discussed above is secured to the cap of the pressure caster with an O-ring fitting, above which is attached a stainless steel tube to act as a chill in the event of over-infiltration. The fibers are heated by a helically wound resistance heater consisting of a 3.2mm diameter, sheathed heating element wound around, and silver soldered to, a 15.2cm long steel cylinder (1.6mm wall thickness). The heater assembly is placed over the quartz tube in the vicinity of the fibers; the space between the heater and quartz is filled by a 1.6mm thick layer of Fiberfrax™ insulation, Figure 4b. Temperature control is maintained with a thermocouple placed between the quartz tube and heater at the midpoint of the fiber preform. Temperature differences measured within the furnace over the 45mm length occupied by the fibers were found to not vary by more than ±5°C.

A second resistance furnace for metal melting is located in the bottom of the pressure vessel portion of the pressure caster. It measures 11.4cm in internal diameter and 15.2cm in height. Metal, either 99.9% or 99.999% aluminum, is melted in a

graphite crucible in air.

Pressurization is achieved with nitrogen gas, which is delivered to the apparatus through two inlets via 10.2mm internal diameter high-pressure hoses. Fast pressurization of the apparatus (≈1.2 seconds) is achieved by pre-pressurizing a holding tank, from which nitrogen is released via two 10.2mm orifice ball valves.

In a typical experiment, the cap is removed from the pressure caster and the fibers and metal are independently heated. The fibers are brought to temperature and allowed to soak for a minimum of thirty minutes (in air, but capability for vacuum or other atmosphere is also available). The metal is melted and allowed to stabilize, then the surface is skimmed to remove the dross. The cap is then lowered onto the pressure vessel so that the bottom of the quartz tube is immersed in the molten aluminum (a thermocouple attached to the bottom of the quartz tube measures the liquid metal temperature). The seal between the cap and the pressure vessel is achieved with an O-ring; the cap is secured to the pressure vessel by sliding the apparatus into a steel frame. The holding tank is then opened. Gas enters the pressure caster, which applies pressure onto the surface of the liquid metal, forcing it upwards into the quartz tube and through the preform. Note that the metal and fibers do not come into contact until infiltration begins, which enables accurate and independent control of the metal and fiber temperatures. The pressure is measured with a pressure transducer located on the cap. As a result of the design of the

device, the die need only sustain the compressive stresses imposed by the pressurized gas; heavy-walled metal dies common to other pressure casters are thus replaced here with a quartz tube.

C. Liquid metal position sensor

A technique was developed to sense the position of the liquid metal front as it advances through the fiber preform during infiltration. A SiC filament is used as a variable resistor, and as a result of its change in resistance during the experiment the liquid metal position can be calculated. The filament of choice is a 140μ diameter SCS-2 SiC fiber manufactured by AVCO-Specialty Materials Division. It is very stiff, which is ideal for specimen preparation, and has a relatively high electrical resistivity (≈10Ω/mm), which is important for resolution of the metal position.

To make use of the technique, a single SiC filament is inserted through the center of the preform during specimen preparation. The top of the filament above the preform has been nickel-plated and is attached to the fitting at the top of the quartz tube, the portions of the filament within the preform and extending out the bottom are unplated and allowed to hang free. The interface between the plated and unplated part of the filament is located exactly at the top of the preform. A load resistor is placed in series with the filament and a constant potential is applied between the load resistor and the metal

crucible, with the molten metal acting as a switch to close the circuit, Figure 5. The potential drop across the SiC filament is then measured as a function of time with a chart recorder. As the metal infiltrates the preform the potential measured across the filament decreases due to the decrease in its effective electrical length. Since resistance and length are linearly related, monitoring the potential drop during infiltration allows a calculation of the position of the metal front and its velocity over time. The equation used to calculate position is:

$$L_t = \left[1 - \frac{V_t(V - V_o)}{V_o(V - V_t)}\right] L_f \qquad (2)$$

where: L_t = liquid metal position at any time

L_f = length of fiber preform

V = applied voltage across filament

V_o = voltage across filament when liquid metal is at the bottom of the preform

V_t = voltage across filament at any time

V_o is found by examining the chart recorder trace and noticing the sudden change of slope that occurs when the liquid metal front encounters the preform. This technique obviates the need to account for changes in resistivity with temperature, as V_o and V_t are both measured with the filament at the same temperature. Examples of typical infiltration profiles are given in Figure 6. Note that near the end of an infiltration experiment the metal velocity is extremely low, which makes the

time at which infiltration completely ceases a somewhat arbitrary measurement.

The accuracy of the measurements was determined from consideration of the accuracy of the voltage readings collected during the experiments. The calculations indicate an accuracy of the position measurement of approximately 10%. The final infiltrated length of most samples was measured independently of the SiC filament and found to deviate from that measured with the sensor by no more than 10%.

D. Measurement of "breakthrough" pressure

The SiC filament sensor also provided a technique for detecting the onset of metal infiltration into the preform, and thus for measuring the pressure required to overcome surface tension forces, which is termed "breakthrough" pressure. For these experiments the infiltration pressure was slowly increased until infiltration into the preform was detected. These experiments were performed under isothermal conditions, as shown in Figure 7, to preclude premature solidification of the metal below the preform during the slow pressurization. Since infiltration occurs first through the larger pores of the preform, experiments were also performed at pressures slightly above the breakthrough pressure to force infiltration of some of the smaller pores.

E. Measurement of permeability

Slow flow of an incompressible fluid through a porous medium (see reference [1]) is predicted by Darcy's law. For a constant applied pressure, Darcy's law can be integrated to yield:

$$\frac{L}{\sqrt{t}} = \sqrt{\frac{2\,\Delta P_\mu\, K}{\mu\,(1 - V_f)}} \qquad (3)$$

where: L = position of liquid front

ΔP_μ = pressure drop in liquid metal due to viscous drag

t = time

μ = viscosity of liquid metal

K = permeability of the porous medium

V_f = fiber volume fraction

Thus given a measure of infiltration length L as a function of time t, the permeability K of the porous medium can be readily calculated (knowing applied pressure ΔP and fiber volume fraction V_f).

In much of the discussion that follows the effects of processing parameters are quantified by a measure of the parameter $L/\sqrt{t}$ introduced above. In this case, a length versus square-root time plot is examined and its slope is measured. The slope is measured just after the 1.2 second pressurization transient that accompanies each experiment.

F. Metallographic examination

Metallographic preparation of composite samples was achieved by polishing with an automatic polisher with diamond paste on hard synthetic cloth, followed by a final polish with magnesium oxide on a soft billiard-type cloth. Figure 8a is a cross-section of a typical Saffil-reinforced 99.999% aluminum composite. Figure 8b is an example unetched microstructure of such a composite. Some samples were chemically etched to reveal grains by immersing for 2-3 seconds in an etch pitting solution of 50ml. nitric acid, 47ml. hydrochloric acid, and 3ml. hydroflouric acid [3]. Observation of the samples under cross-polarizers accentuates the etch pits and readily shows differences in their orientation across different grains. An example in unreinforced aluminum is provided in Figure 9.

III. RESULTS

The results of permeability experiments performed with water, described in section *A* above, are presented in Figure 10. The results of permeability measurements performed with 99.999% aluminum, described in section *E* above, are presented in Figure 11, where they are displayed in terms of fraction solid metal, g_s, so that both water and metal permeability experiments could be included in the same plot. The metal experiments were run at different fiber temperatures, from which a value of g_s was calculated using equation 17 of reference [1]. The data for all

the experiments performed in this work are tabulated in Table I.

The effect on the infiltration kinetics of such processing parameters as fiber volume fraction, fiber temperature, metal temperature and infiltration pressure was quantified by the measurement of two parameters: $L/\sqrt{t}$, which is described in section *E*, and L_f, the final infiltrated length. In the figures that follow, experimental data are presented along with theoretical curves. The details of the calculations will be discussed in the following section.

Figures 12 to 15 relate the influence of fiber volume fraction, fiber temperature, metal temperature, and applied pressure on $L/\sqrt{t}$, respectively. Figure 16 presents these data in terms of V_{sf}.

Figures 17 to 20 relate the influence of fiber volume fraction, fiber temperature, metal temperature, and applied pressure on the final infiltration length L_f, respectively.

Breakthrough experiments were performed under isothermal conditions as described in section *D* above. For preforms of 25 volume percent and a temperature of 700°C it was found that approximately 0.20MPa was required to initiate infiltration into the preform, but that 0.45MPa was required to infiltrate approximately 90% of the pores. Therefore a nominal value of 0.3MPa is assumed as the breakthrough pressure.

Experiments were also performed to investigate the effect of mold radius and metal purity on infiltration behavior. The effect of the former is shown in Figure 21 for experiments with 99.9% aluminum; that of the latter is shown in both Figures 22

and 23. The purity of the starting material was certified by the supplier, the purity of the material after infiltration was determined by chemical analyses of samples taken from unreinforced portions of the casting located close to the fiber preform.

The scatter between experiments was small, owing in part to the degree of parametric control that was exercised. An example of the reproducibility of the infiltration process as measured by the SiC filament is shown in Figure 24. Note the very reproducible values of both final infiltration length and $L/\sqrt{t}$, even though the initial transient varied slightly in the two cases.

IV. DISCUSSION

The curves drawn in Figures 11 to 20 were calculated from the equations presented in reference [1]. The values of fiber volume fraction, fiber temperature, metal temperature, and infiltration pressure were taken directly from the processing parameters of each experiment, while the value of fiber radius was derived from the permeability measurements using water. To calculate fiber radius, equation 2 of the theory was used along with the permeability measured with water. The calculation yields a fiber radius of 1.9μm, matching well the value of 1.5μm reported by the supplier. Using this value of the fibe radius in equation 2 of the theory, the theoretical curve in Figure 11 was drawn. Note the excellent agreement with

experiment for permeability values that range over three orders of magnitude. [It is noteworthy to mention that the batch of raw materials used to fabricate the preforms can affect the measured fiber radius. Water permeability experiments performed on a group of preforms not used in this study yielded a fiber radius of 2.1μm. Presumably differences in the level of binder and the distribution of fiber sizes were responsible for the difference.]

The influence of fiber volume fraction and fiber temperature is shown in Figures 12 and 13, where two theoretical curves are presented, one for no superheat and one for 20°C of superheat. The curves presented in reference [1] are for the case of no metal superheat, however sound foundry practice dictates casting with some degree of superheat because of the possibility of premature formation of solid in the crucible or at the preform entrance. Therefore experiments were run with 20°C of superheat and the curves were calculated as detailed in reference [1]. Again note the excellent agreement between theory and experiment, and note also the sensitivity of the experimental technique.

The extreme sensitivity of the process to fiber volume fraction is due to its dual role in the permeability expression given in reference [1]. Not only does increasing the fiber volume fraction decrease the spacing between fibers, but it also increases the amount of solid formed per volume. This dual role significantly depresses the permeability upon a small increase in fiber volume fraction.

Theoretical considerations suggest that the effect of fiber volume fraction and fiber temperature can be combined. During the infiltration process only the size of the fiber, and not its shape, is changed by metal solidification. Therefore the infiltration kinetics should be accurately described by a parameter that describes the total amount of solid material contained in the preform, whether it be fiber or metal. This parameter, V_{Sf}, is defined in reference [1] by equations 17 and 20. The result of this calculation is shown in Figure 16, where the agreement between experiment and theory is very good.

The effect of metal superheat is shown in Figure 14. The theoretical curve is obtained using equations 25 and 26 of reference [1]. Again note the agreement between theory and experiment. Metal superheat is seen to have a minor role in the effect on infiltration kinetics. This is due to the fact that metal superheat, as discussed in reference [1], causes remelting of the solid metal around the fibers. To impart a significant effect on permeability, a considerable portion of the composite must be remelted. However, remelting requires such a large amount of thermal energy that for metal superheats normally encountered in the foundry, remelting distances are moderate and the effect on infiltration kinetics is minimal

To experimentally verify the physical model of the role of superheat, a technique was developed for infiltrating a small amount of aluminum followed by molten lead, Figure 25. While the aluminum solidifies in the preform during infiltration, the lead flows into those volumes not occupied by the aluminum.

This provides a high contrast metallographic observation of the volumes where the aluminum first flowed and solidified. The photomicrograph in Figure 26 shows the results of an experiment performed with the metal at 60°C superheat. Note the existence of a region at the base of the composite where the aluminum has been entirely replaced by lead. At the end of the experiment, therefore, this region was entirely liquid; any aluminum which had solidified had been remelted. In the central portion of the composite, lead and aluminum coexist in the matrix indicating that some aluminum was retained by the fibers as the lead flowed past. To be retained by the fibers, this aluminum must have been solid. Indication of a two-zone structure in cast aluminum matrix composites could also be found when the superheat was sufficiently high to yield a region of large columnar grains in the upstream portion of the composite, Figure 27. Note that this is also experimental evidence that the fibers do not act as nucleation sites for the growth of solid. Further down the same sample, in the vicinity of the infiltration front, the microstructure is shown by the photomicrograph in Figure 28, where many orientations of etch pits in a small volume indicate a fine grained matrix. This indicates the high nucleation rate achieved by rapid cooling by the fibers at the infiltration front.

Finally, the curve relating $L/\sqrt{t}$ to applied pressure is shown in Figure 15. In these experiments it was not possible to neglect the effect of ΔP_γ at low applied pressures as was done in reference [1], therefore the value found from the

breakthrough experiments described above was used. The curve was calculated using equation 3 with $\Delta P_\mu = P_o - \Delta P_\gamma$. Note that agreement between theory and experiment is good only at higher pressures, where the effect of the capillary pressure is minimized; at lower pressures the experiments deviate from theory.

An empirical method of determining the capillary pressure ΔP_γ is available from the experimental data. Since the permeability of the preform is the same for any two experiments shown in Figure 15, there exists a unique value of ΔP_γ such that the ratio $L^2/t(P_o - \Delta P_\gamma)$ remains the same for each experiment (see equation 3). The calculation yields ΔP_γ=1.1MPa and was verified with calculations on additional experiments. This value is much larger than that used to calculate the curve in Figure 15, and also larger than that calculated by Clyne and Mason (approximately 0.6MPa) [4]. One possible explanation for this behavior is that both the breakthrough experiments and Clyne's calculations are performed for isothermal conditions above the metal melting point. Oh [5] observed that lowering the fiber temperature raised the capillary pressure. This effect may have some applicability in this case, but no formal experiments have been run to confirm this theory.

The curves drawn in the plots of final infiltration length, Figures 17, 18, and 20, were calculated from the numerical integration of equation 34 of reference [1]. The heat loss was assumed to be limited by convection to the surroundings and so equation 36 of reference [1] describes the growth of

solid from the mold wall. Best agreement of theory with experiment is obtained assuming a value of h_θ of 250W/m^{2}C, Figure 29. This value lies between the typical values of 3000W/m^{2}C for fluidity tests with aluminum [6] and 10W/m^{2}C for cooling by natural convection in air [7]. However, the thin-walled quartz molds used in these experiments are capable of absorbing from 80% to 100% of the required solidification enthalpy before becoming thermally saturated and so the actual mechanism, depending on the experimental conditions, can be a combination of heat flow into a mold (quartz) of finite thickness, and convection to the surroundings. For the case of solidification controlled totally by heat flow to the mold, a finite difference approximation was used to calculate the temperature profile in the quartz over time, which was then used to determine the heat flux to the quartz, and hence the solidification in the composite. These results are presented in Appendix C for different values of h_θ and compared to experiment.

Returning to the experimental data for L_f, note that the effects of the processing parameters mirror those of $L/\sqrt{t}$, with the same experimental agreement with theory. The curves shown are calculated for the case of no metal superheat; the theory has not been extended to predict the effect of metal superheat on final infiltrated length. Thus the curve drawn in Figure 19 for metal superheat is simply a least squares fit to the experimental data.

The calculation of L_f is based on external heat losses being the mechanism for the cessation of infiltration. The physical model of solidification from the mold wall is confirmed by a re-examination of the aluminum-lead experiment of Figure 26. Near the mold wall primarily aluminum exists, indicating complete solidification of the aluminum at the mold wall prior to infiltration by lead. This corresponds well with the schematic drawing of solidification shown in Figure 21 of reference [1]. The effect of the mold radius is shown experimentally in Figure 21. Note that a change in mold radius does not affect the beginning of infiltration, but does have an impact on the time at which flow ceases and thus the total infiltrated length. This is in qualitative agreement with theoretical predictions that mold radius should not effect preform permeability, but will effect the growth of solid due to external heat losses.

Metal purity was noted to have a very strong effect on the infiltration kinetics, as shown in Figures 22 and 23. Not only could the difference between 99.999% and 99.9% aluminum be detected, but when repeatedly using a melt of 99.999% aluminum, a significant difference in infiltration kinetics could be detected when the melt purity dropped to only 99.95%. The effect of metal purity on fluid flow was also observed by Feliu et al.[8] where they reported an 8% decrease in fluidity in a vacuum fluidity test when changing from 99.99% to 99.9% aluminum. They concluded the impurities influenced the mode of solidification, which in turn affected the drag between liquid

and solid metal. This conclusion has also been documented by observations of the transition from planar to cellular solidification interfaces due to small changes in solute levels [9]. Therefore, the lower purity metal may form solid that is not a smooth cylinder surrounding a fiber, Figure 30. Therefore, the increase in surface area is responsible for the decrease in permeability. Finally, in the case of an alloy the permeability is markedly lowered because not only is the interface irregular, but the solid does not grow on the fibers [10].

V. SUMMARY AND CONCLUSIONS

1) An apparatus was designed and built for the infiltration of molten metal into porous preforms under carefully controlled processing conditions. The apparatus utilized pressurized gas to cause infiltration under a constant applied pressure.
2) A sensor was developed to measure the flow of liquid metal through a porous preform composed of non-conductive material. This sensor was used for quantitative measurements of infiltration kinetics.
3) Quantitative agreement of theory with experiment has been shown under a variety of processing conditions. For example, it was shown that an increase in fiber volume fraction of only 10% from 0.22 to 0.24 caused a drop in infiltration length of 46%, however an increase in fiber temperature by 10% from 250°C to 275°C increased

infiltration length by only 35%. The effect of applied pressure on infiltration length is parabolic, thus a 10% increase in pressure results in only a 5% increase in length.

4) Metal superheat induces a gradual remelting at the preform entrance of solid previously formed. This mechanism was verified by metallographic observation of experiments performed with the immiscible aluminum-lead system. The technique also provided experimental verification for solidification from the mold walls, which is the mechanism for cessation of infiltration.

5) The effect of capillary pressure was noted for experiments at low values of applied pressure. The capillary pressure calculated from these experiments was much larger than those calculated and measured for the same system with the fibers heated above the metal melting point.

6) The effect of metal purity on infiltration was extremely pronounced. A decrease in purity from 99.999% to 99.9% resulted in a decrease in infiltration length of 50%. It was concluded that the impurity level affects the mode of solidification; lower purity material solidifies with a non-planar solid-liquid interface and thus creates a greater drag on the flowing fluid than a smooth interface.

7) These experimental results provide strong confirmation of the analysis of infiltration presented in a previous paper, and show that simple calculations can be performed to predict the results of many practical infiltration processes.

Appendix A: Validity of assumptions

Implicit in the application of the equations presented in the theory is the validity of the assumptions introduced in the derivation of those equations. Table II is a list of the physical and thermal properties for the Saffil-reinforced aluminum composites studied in these experiments. In what follows each of the assumptions introduced in the theory are validated.

Crossflow through a square array of cylinders: Although infiltration is perpendicular to the fiber axis for more than 90% of the fibers, the process used in the fabrication of the preform does not exactly align all the fibers in two dimensions. The micrograph in Figure 8 shows a few fibers that are oriented obliquely to the metal flow direction, which would result in an increased permeability in that area. However, because the fibers are only 500μm in length this region of increased permeability only accounts for a small, microscopic pocket. The bulk of the preform is experiencing infiltration in crossflow, so that even though on a microscopic scale the infiltration front has many fine spikes in it, on a macroscopic scale as measured in these experiments the infiltration front progresses as a plane.

The square array of fibers was used for simplicity. Although the preforms used in these experiments are clearly not composed of fibers on a square array, the data in the review of Jackson and James [11] indicate that the geometry of the array

is not a significant factor for the measurements of these experiments.

Creeping flow: Throughout this work it is assumed that Darcy's law describes the flow of metal through the preform; a valid assumption for Reynolds numbers (based on fiber diameter, see equation 8 of reference [1]) less than 1. In these experiments the maximum velocity measured is on the order of 0.01 m/s, the fiber diameter we use is the experimentally measured value of 3.8μ, and viscosity and density data are provided in Table II. The Reynolds number for these experiments is on the order of 0.08, clearly within the creeping flow regime.

Negligible viscous energy dissipation: It is assumed that the energy released due to viscous flow of the liquid metal past the fibers is negligible. The Brinkman number is a measure of the significance of viscous energy effects, defined as:

$$Br = \frac{\mu \left(\frac{dL}{dt}\right)^2}{k_m \Delta T}$$

where ΔT is the temperature difference within the liquid metal. Viscous energy effects are significant for $Br>2$ [12]. We shall assume, for instance, that a $1^{o}C$ temperature difference is considered significant. Using values from Table II, along with a value of 0.01 m/s for dL/dt, one finds that $Br \approx 10^{-5}$, which clearly indicates a negligible effect of viscous dissipation.

Instantaneous heat transfer between metal and fibers: In section IV of reference [1] an expression is developed for the time taken for a fiber to heat to a given temperature for a

given value of the the heat transfer coefficient, h. It is difficult to provide a reasonable estimate for h. Certainly h values encountered in conventional casting processes have limited applicability in the pressure casting of composites. Overall heat transfer coefficients calculated from Nusselt number approximations are not valid because conduction is much faster than convection on this size scale. Therefore as a worst case estimate we consider the heat transfer by conduction through a 1μm air gap between the metal and fiber. The value of h is therefore estimated as 2.6×10^4 W/m^2C. Using equation 31 of reference [1] and the values in Table II we estimate a time lag of approximately 0.3 microseconds. To translate this time lag into an effect on infiltration, we numerically solve equation 32 of reference [1], see Appendix C. This is displayed in Figure 20 of the same reference, where the infiltration length has been ratioed to the length that would have resulted if the heat transfer to the fibers had been instantaneous. Note that the ratio becomes approximately unity for times greater than about 0.01 seconds; therefore for an experiment that lasts approximately 10 seconds, the effect of a finite heat transfer coefficient between the metal and fibers is negligible.

Negligible heat transfer ahead of the infiltration front:

Equation 30 in reference [1] describes the effect of heat transfer ahead of the infiltration front. The effect manifests itself as an increase in the solid metal that forms around the fibers. Referring to the last term in brackets in equation 30, the quantity $r_g c_g / r_f c_f$ is much less than unity for a Saffil

preform surrounded by air (see Table II) and so this term can be neglected. The other term in brackets in equation 30 becomes significant only when the value of $A = \Psi/2\sqrt{\alpha_c}$ falls below unity; refer to Figure 18 of the same reference. One calculates α_c using the expression for k_c for a Saffil/air "composite" in transverse flow (equation 4 in reference [1]); the $\rho_c c_c$ term is calculated from the rule of mixtures. In this manner, for a 24 volume percent Saffil preform we find $A = \Psi/4.2\text{x}10^{-4}$, which will clearly be larger than unity for all values of Ψ measured experimentally in Table I. Therefore the effect of heat transfer ahead of the infiltration front is negligible for all the experiments considered in this work.

Negligible temperature gradients in the composite perpendicular to the infiltration direction: The Biot number gives a measure of the significance of temperature gradients within the composite, defined as:

$$Bi = \frac{h_e R_i}{k_c}$$

For Biot numbers less than approximately 0.1 the temperature in the composite is nearly uniform [13]. For the system considered in this work, where h_e is approximately 250 W/m^2C, R_i is 0.0085m and k_c is given by rule of mixtures, we find Bi=0.03, clearly within the regime where temperature gradients may be considered negligible.

Appendix B: Pressure infiltration of Al-4.5%Cu alloy

Infiltration of a cold fiber preform with an alloy results in macrosegregation parallel to the direction of infiltration due to simultaneous solidification and fluid flow. The solid that forms due to contact with the cold fibers is entrapped by the fiber network, whereas the surrounding enriched liquid is free to continue moving downstream. The result is a solute impoverished region near the base of the composite and a solute enriched region near the tip of the composite, with a resulting concentration profile and microstructure as shown in Figure B-1.

In the case of metal superheat, as explained previously, a region at the base of the composite remelts and is replaced by liquid of the nominal composition. Since this region is fully liquid after infiltration ceases, the subsequent solidification is not affected by the forced fluid flow and therefore results in a region of nominal composition, Figure B-2.

Appendix C: Numerical Calculations

In this section programs that were written and used for numerical calculations are listed, they are found together as Figure C1. Specifically, the program for h-controlled heat transfer solves equation 34 of reference [1] using equation 36 of the same reference. Similarly, the program for conduction-controlled heat transfer also solves equation 34, but using equation 37. The program for non-instantaneous heat

transfer solves equation 32, as was mentioned in Appendix A.

The remaining program listed is a finite difference approximation for the temperature profile in a cylindrical mold of finite thickness where one wall is adiabatic and the other absorbs heat from an infinite medium at constant temperature through an interface with a heat transfer coefficient h. The approximation is [15]:

$$T_{t+\Delta t}(m) = \frac{T_t(m-1)\left(1 - \frac{\Delta r}{2\,r(m)}\right) + T_t(m+1)\left(1 + \frac{\Delta r}{2\,r(m)}\right)}{2}$$

$$\text{for } 2 = \frac{\Delta r^2}{\alpha\,\Delta t}$$

where m is the node number, r is the radius and t is time. At the surface, which is node 1, a flux balance in invoked:

$$2\pi r_1 h\,[T_M - T(1)] = 2\pi k \frac{T(1) - T(2)}{\ln \frac{r_2}{r_1}}$$

From the temperature profile calculated at each time interval, a heat flux is calculated and balanced with the amount of solid that must have formed. The effect on flow is then similar to those simplified cases mentioned above. The results of the calculations for various values of h are shown in Figure C2. Note that an h of approximately 600W/m^{2}K agrees well with experiment. This value is somewhat closer than the previous calculations to the value of 3000W/m^{2}K reported in the literature. At other typical experimental conditions this technique is not applicable due to the fact that the quartz tube

becomes thermally saturated; therefore other heat loss mechanisms must be present.

REFERENCES

1. A. Mortensen, L.J. Masur, J.A. Cornie, and M.C. Flemings: "Infiltration of Fibrous Preforms by a Pure Metal, Part I: Theory"
2. T.W. Lambe and R.V. Whitman: *Soil Mechanics, SI Version*, John Wiley & Sons, New York, NY, 1979, p.281.
3. *Smithells Metals Reference Book, Sixth Edition*, Butterworths, London, UK, 1983, p.10-27.
4. T.W. Clyne and J.F. Mason: *Metall. Trans. A*, 1987, vol.18A, pp.1519-1530.
5. Se-Yong Oh, Ph.D. Thesis, Massachusetts Institute of Technology, 1987.
6. M.C. Flemings, F.R. Mollard, E. Niyama, and H.F. Taylor: *Trans. AFS*, 1962, vol.70, pp.1029-1039.
7. J. Szekely and N.J. Themelis: *Rate Phenomena in Process Metallurgy*, John Wiley & Sons, New York, NY, 1971, p.234.
8. S.Feliu, M.C. Flemings, and H.F. Taylor: *The British Foundryman*, 1960, vol.43, pp.413-425.
9. W.A. Tiller and J.W. Rutter: *Can. J. of Physics*, 1956, vol.34, pp.96-121.
10. A.Mortensen, J.A.Cornie and M.C.Flemings, "Columnar Solidification in a Metal Matrix Composite", accepted *Metallurgical Transactions A*.
11. G.W.Jackson and D.F.James: *Can. J.of Chem. Eng.*, 1986, vol.64, pp.364-374.

12. R.B. Bird, W.E. Stewart, and E.N. Lightfoot: *Transport Phenomena*, John Wiley & Sons, New York, NY, 1960, p.278.

13. G.H. Geiger and D.R. Poirier: *Transport Phenomena in Metallurgy*, Addison-Wesley Publishing Company, Reading, MA, 1973, p.303.

14. T.W. Clyne and M.G. Bader: in *Proc. Fifth Int. Conf. Composite Materials (ICCM5)*, W.C. Harrigan, J. Strife, and A.K. Dhingra, eds., TMS-AIME, 1985, pp.755-771.

15. *Handbook of Heat Transfer*, W.M. Rohsenow and J.P. Hartnett, eds., McGraw-Hill Book Company, New York, NY, 1973, p.4-62.

Run number	Metal purity	Mold radius (mm)	V_f	T_f (°C)	ΔP (MPa)	T_o (°C)	Ψ (m/√s)	L_f (mm)	V_{sf}
1	99.9%	5.5	.245	750	0.72	750	---	---	
2	99.9%	5.5	.250	710	0.46	710	---	---	
3	99.9%	5.5	.250	700	0.26	700	---	---	
4	99.9%	5.5	.250	330	3.59	687	---	23.0	.60
5	99.9%	8.5	.250	330	3.52	682	.0144	43.5	.60
6	99.9%	8.5	.250	302	3.55	686	.0113	33.5	.63
7	99.9%	8.5	.240	286	3.42	678	.0101	20.5	.62
8	99.990% *	8.5	.240	287	3.48	680	.0137	38.5	.62
9	99.999%	8.5	.240	289	3.48	678	.0136	39.0	.61
10	99.999%	8.5	.240	273	3.52	677	.0129	33.0	.63
11	99.991% *	8.5	.240	257	3.52	680	.0115	29.5	.65
12	99.999%	8.5	.240	231	3.45	677	---	22.0	.67
13	99.987% *	8.5	.240	468	3.45	675	.0304	>45	.43
14	99.999%	8.5	.240	210	3.42	670	.0051	11.5	.69
15	99.990% *	8.5	.240	372	3.45	675	.0201	>45	.53
16	99.999%	8.5	.235	255	3.42	845	.0147	37.0	
17	99.947% *	8.5	.245	255	3.31	738	.0104	23.0	
18	99.999%	8.5	.240	254	3.45	800	.0125	33.0	
19	99.999%	8.5	.235	255	3.42	750	.0121	30.0	
20	99.999%	8.5	.220	211	3.45	680	.0144	36.5	.64
21	99.999%	8.5	.240	285	2.35	680	.0100	29.0	.62
22	99.999%	8.5	.240	285	1.30	680	.0052	10.5	.62
23	99.999%	8.5	.260	255	3.38	680	.0070	14.5	.70
24	99.999%	8.5	.220	256	3.38	683	.0158	45.0	.59
25	99.999%	8.5	.240	289	2.28	677	.0119	34.5	.62
26	99.999%	8.5	.240	285	4.52	678	.0141	39.5	.62
27	99.999%	8.5	.245	287	0.90	675	---	4.0	
28	99.999%	8.5	.240	284	1.73	679	.0079	21.0	

* indicates chemical analysis was performed

Table I: Summary of experiments with pure aluminum.

Property	Units	Aluminum	Saffil	Quartz	Air
ρ	(kg/m^3)	$2.4x10^3$	$3.3x10^3$	$2.2x10^3$	$1.1x10^0$
ρC	(J/m^3K)	$2.6x10^6$	$4.0x10^6$	$3.1x10^6$	$1.1x10^3$
k	(W/m K)	93	8	2	$2.6x10^{-2}$
α	(m^2/s)	$36x10^{-6}$	$2x10^{-6}$	$0.65x10^{-6}$	$2.4x10^{-5}$
$\rho\Delta H$	(J/m^3)	$9.5x10^8$			
μ	(Pa.s)	$1.3x10^{-3}$			

Table II: Values of selected thermal and physical constants

Number	V_f	$K_{(m^2)}$
1	.230	7.8×10^{-13}
2	.233	7.5×10^{-13}
3	.245	6.0×10^{-13}
4	.248	5.0×10^{-13}
5	.255	5.0×10^{-13}
6	.261	4.0×10^{-13}

Table III: Summary of experiments with water

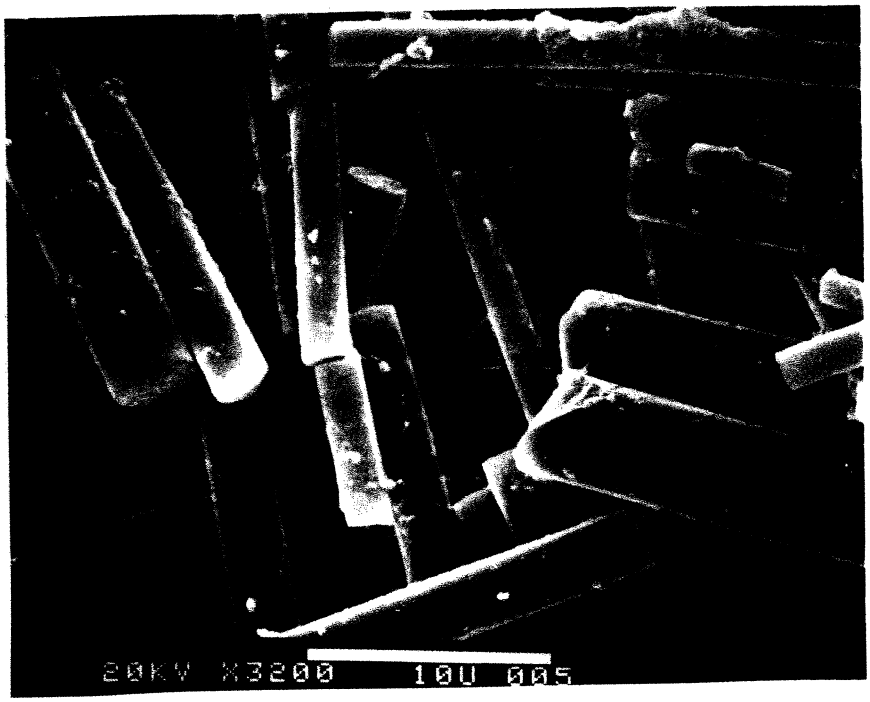

Figure 1: Scanning electron micrograph of Saffil alumina preform. Infiltration direction is parallel to viewing direction.

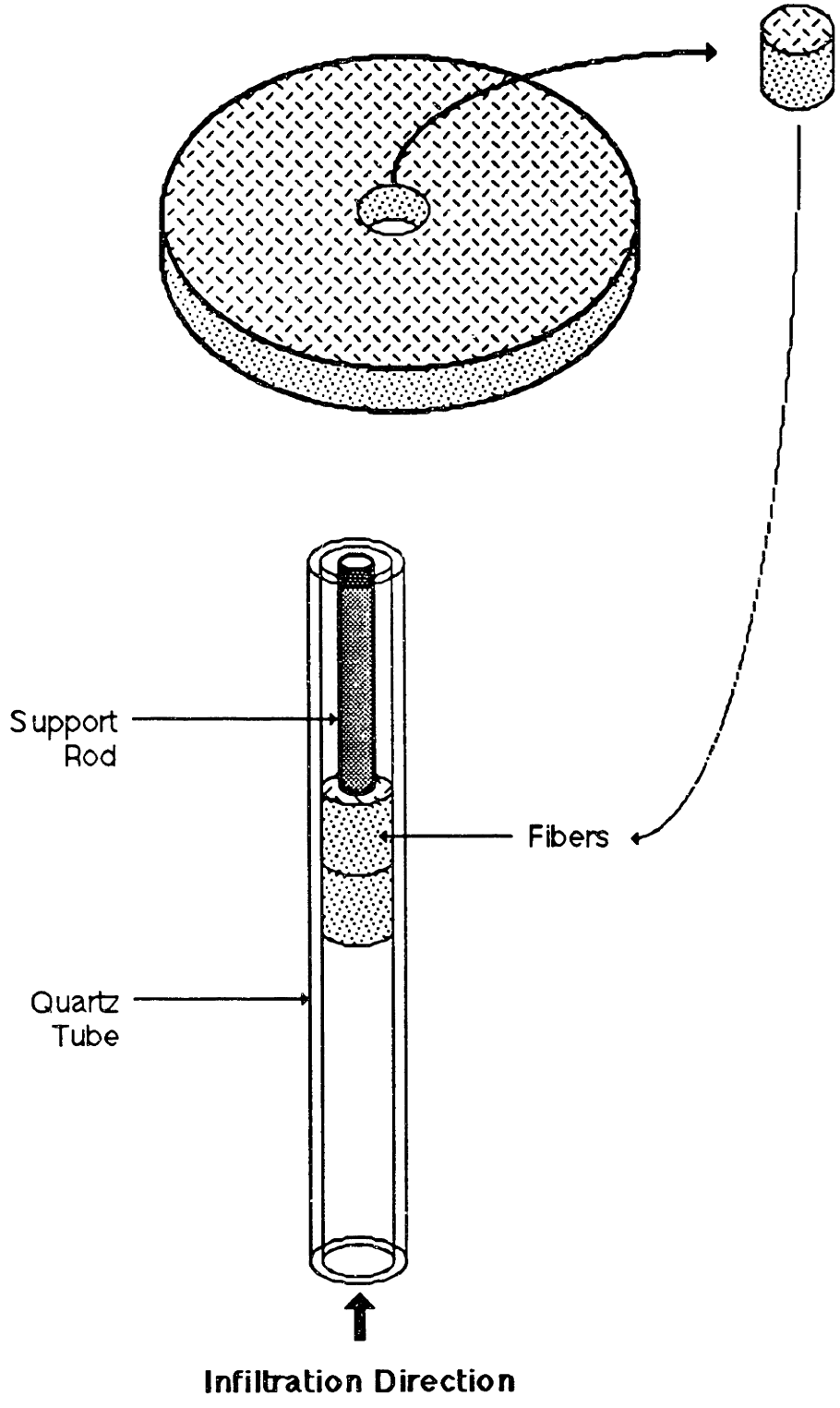

Figure 2: Schematic drawing of fiber preform preparation process

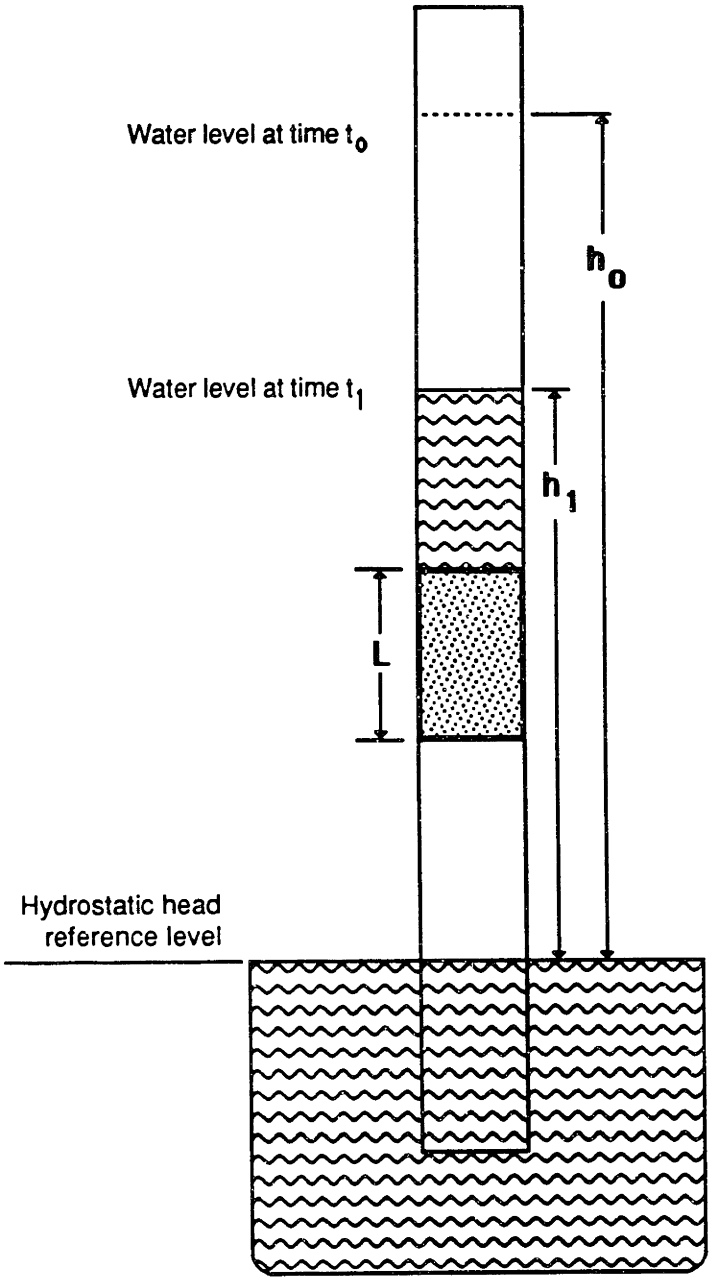

Figure 3: Schematic drawing of water permeability test (falling head type).

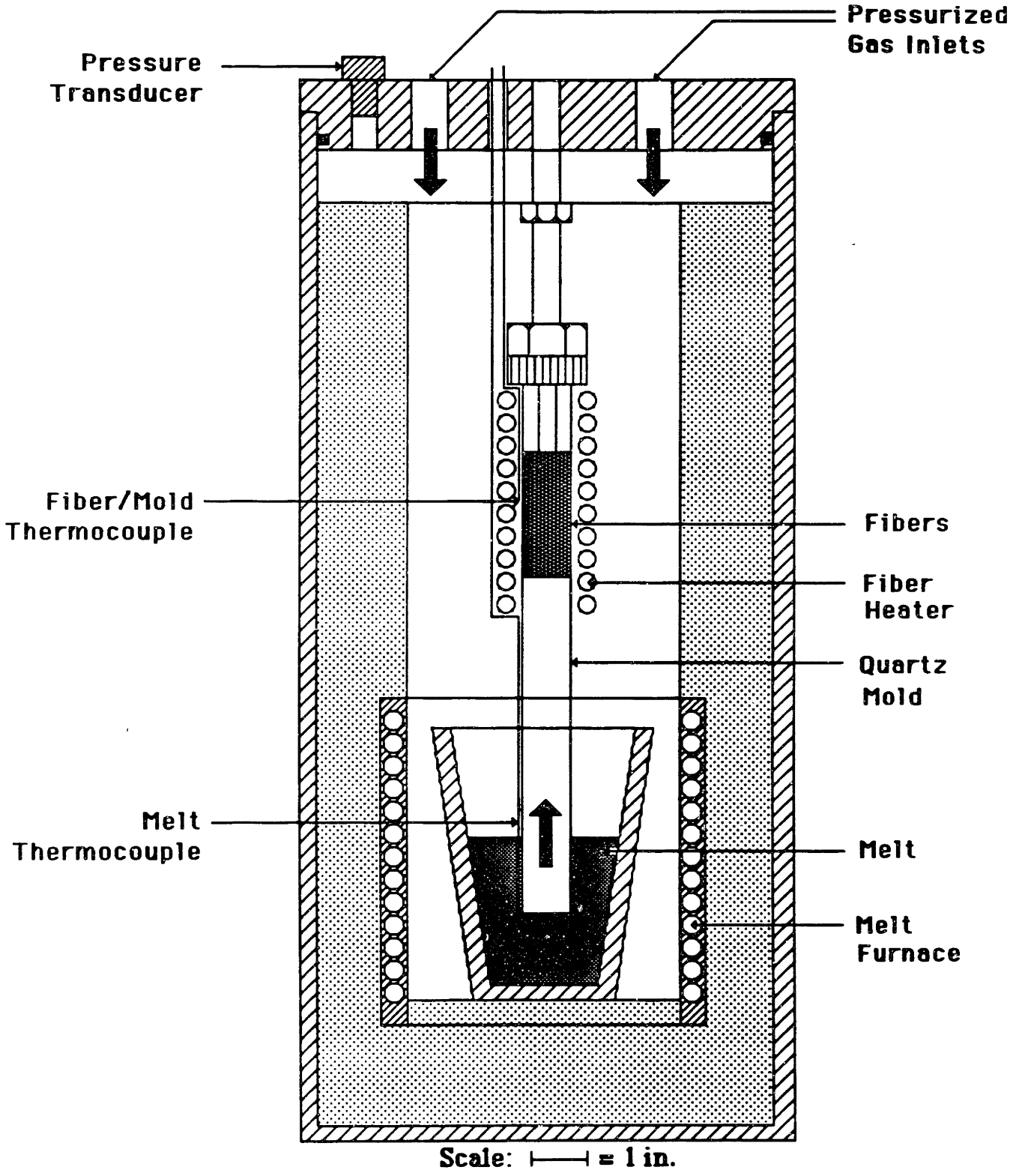

Figure 4a: Schematic drawing of pressure caster

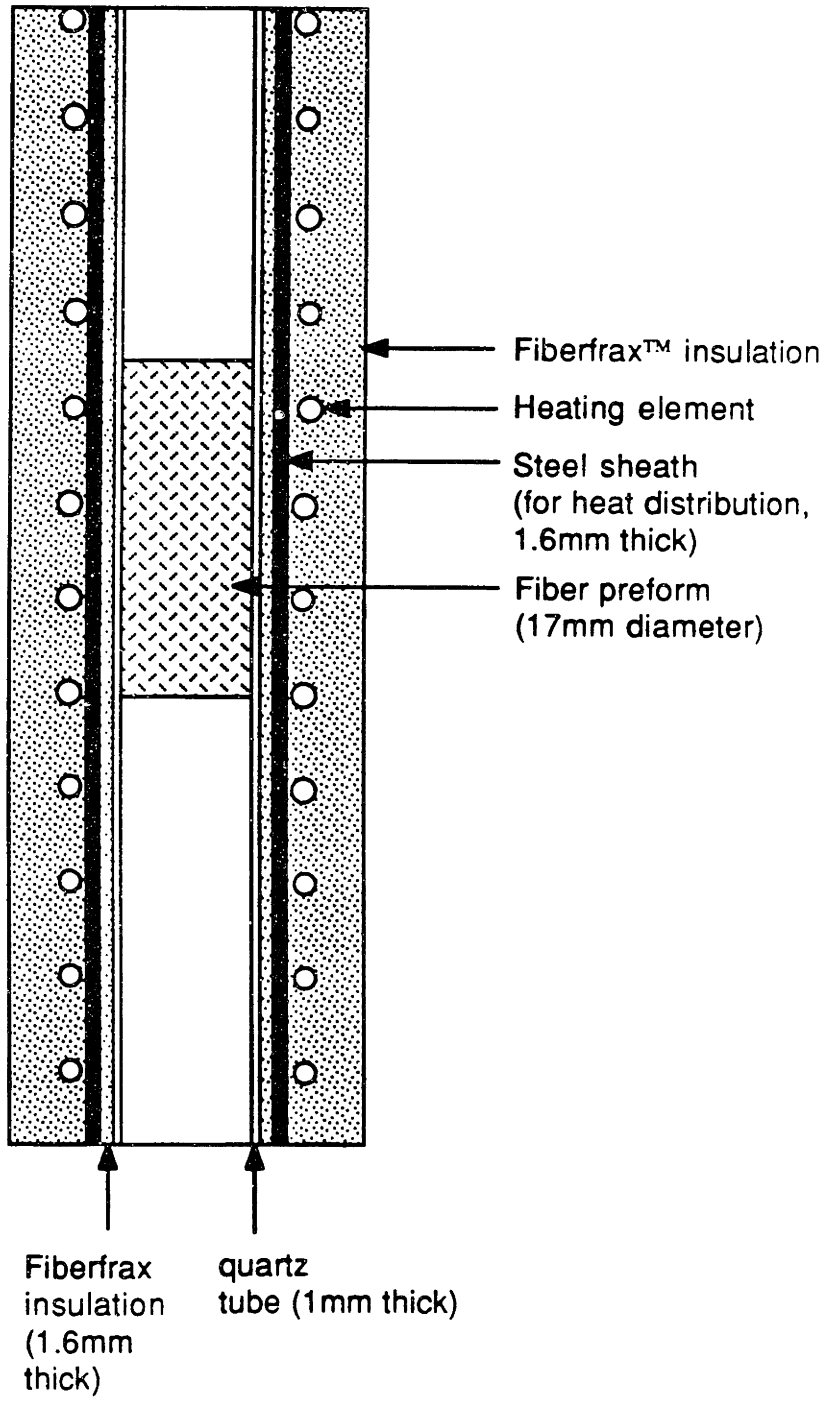

Figure 4b: Schematic drawing of experimental arrangement of fiber preform and heater. Scale is 1:1.

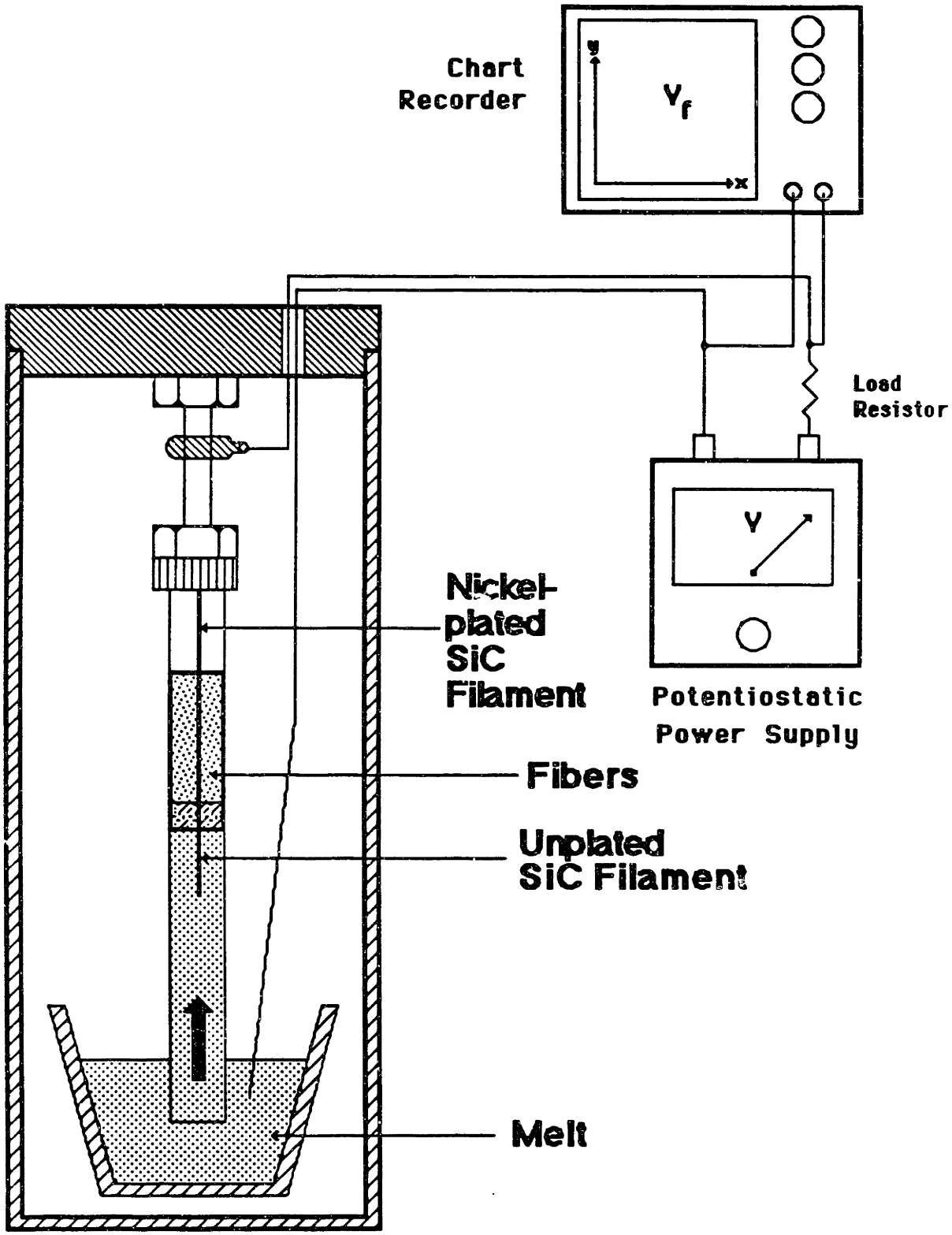

Figure 5: Schematic drawing of liquid position measurement technique. SiC filament detects movement of liquid metal.

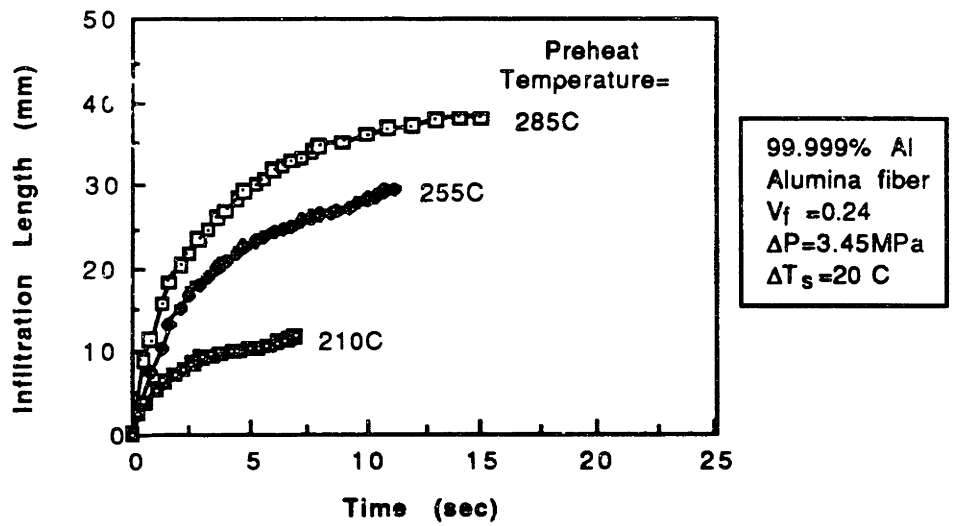

Figure 6: Typical infiltration profiles measured with apparatus shown in Figure 5.

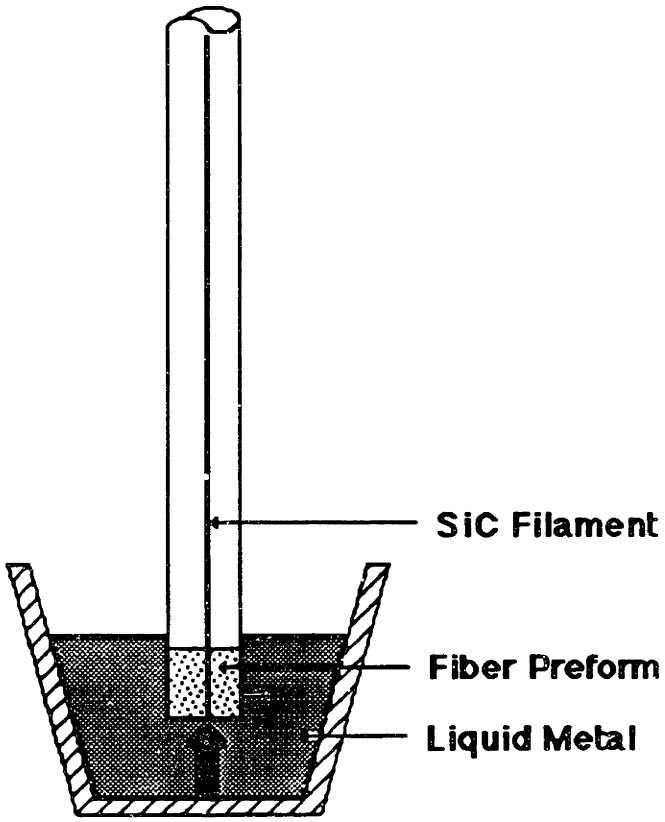

Figure 7: Schematic drawing of breakthrough pressure experiment. Preform is heated by immersion in liquid metal; SiC filament detects movement of liquid metal in preform.

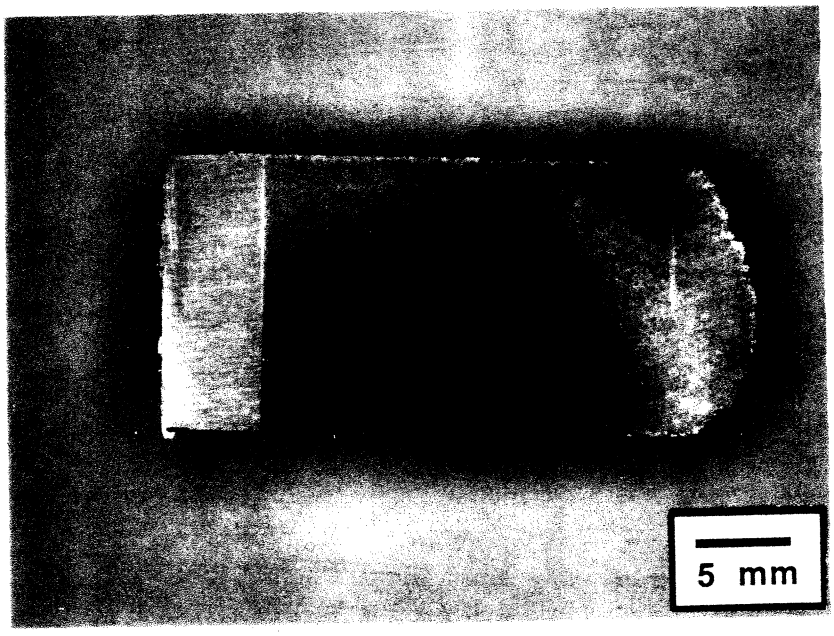

Figure 8a: Cross-section of typical Saffil-reinforced aluminum composite produced with experimental apparatus.

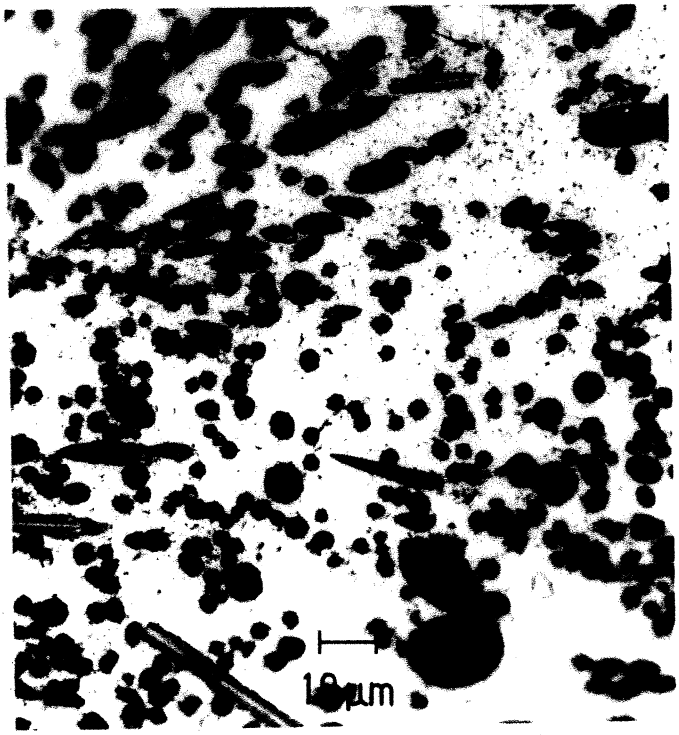

Figure 8b: Photomicrograph of 24 volume percent Saffil-reinforced aluminum (99.999% pure). Infiltration direction is upwards.

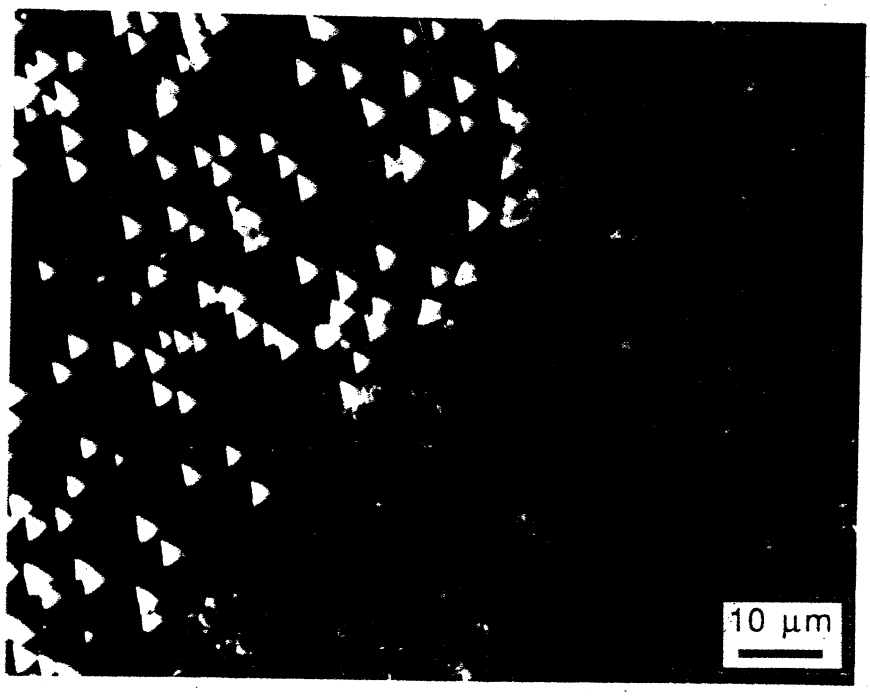

Figure 9: Photomicrograph of etch pitted sample viewed under cross-polarized light. Note difference in orientation of pits across different grains.

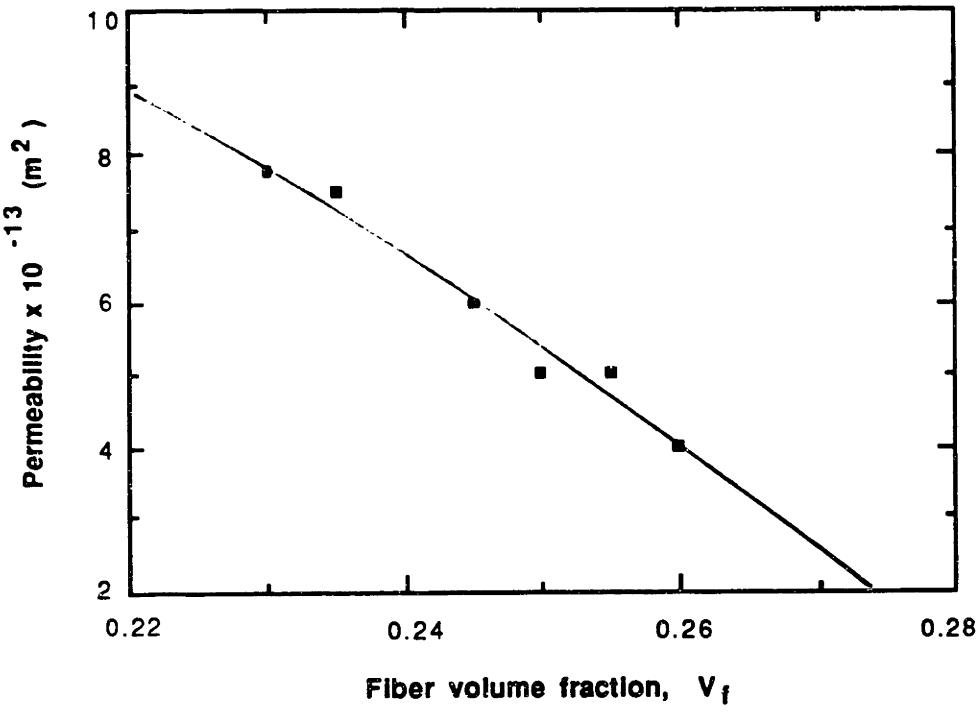

Figure 10: Experimental measurements of preform permeability using water. From equation 1 using the apparatus shown in Figure 3.

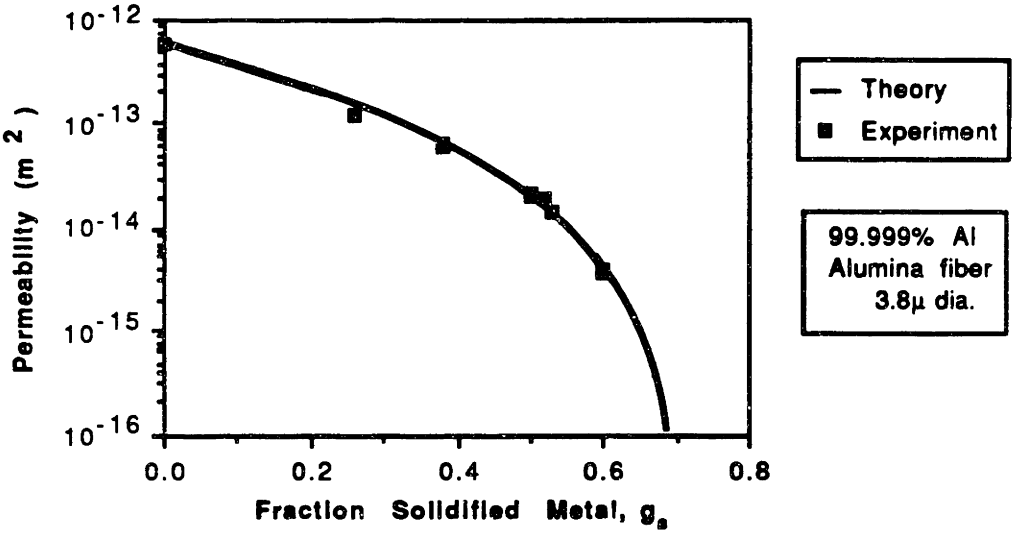

Figure 11: Plot of permeability as a function of fraction solidified metal. Experimental point at 0.0 solidified metal is for an experiment using water. This datum point is used to calculate fiber radius.

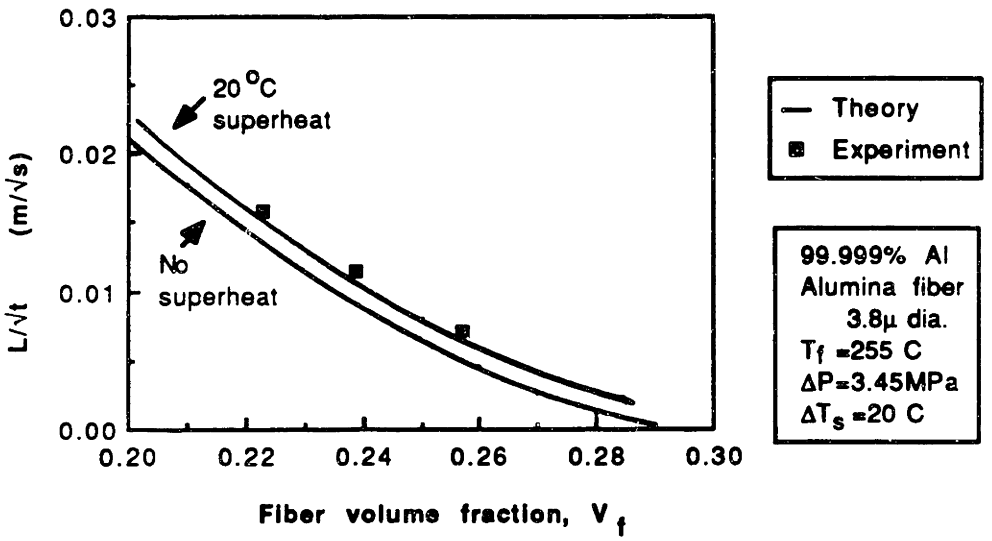

Figure 12: Effect of fiber volume fraction on $L/\sqrt{t}$. Curves drawn are for no superheat and 20°C of superheat; negligible capillary pressure.

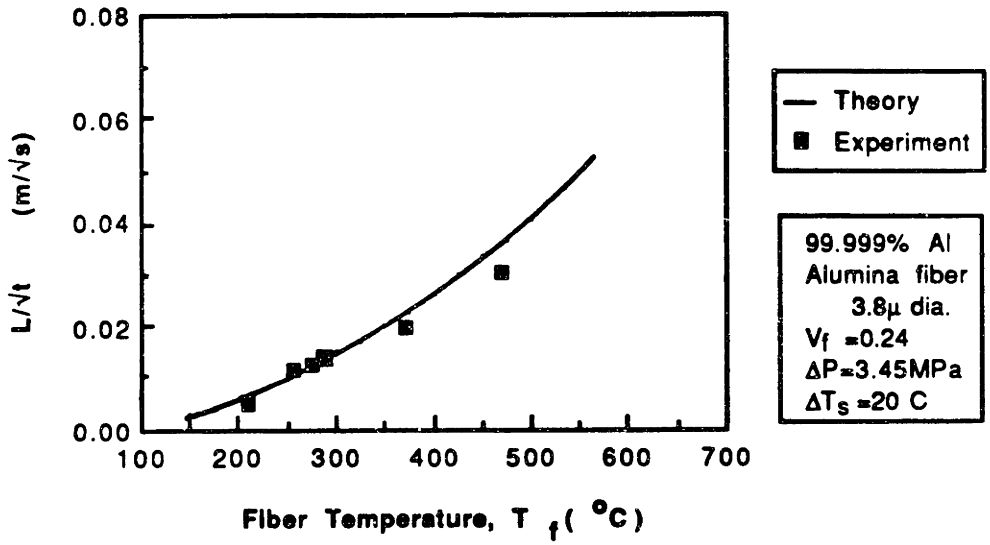

Figure 13: Effect of fiber temperature on $L/\sqrt{t}$ Curve drawn is for 20°C of superheat and negligible capillary pressure.

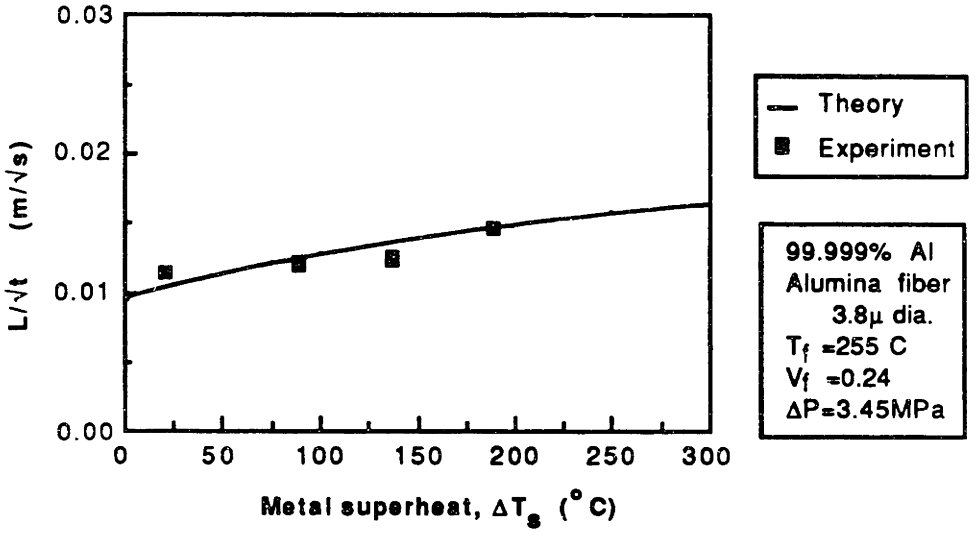

Figure 14: Effect of metal superheat on $L/\sqrt{t}$. Curve drawn is for negligible capillary pressure.

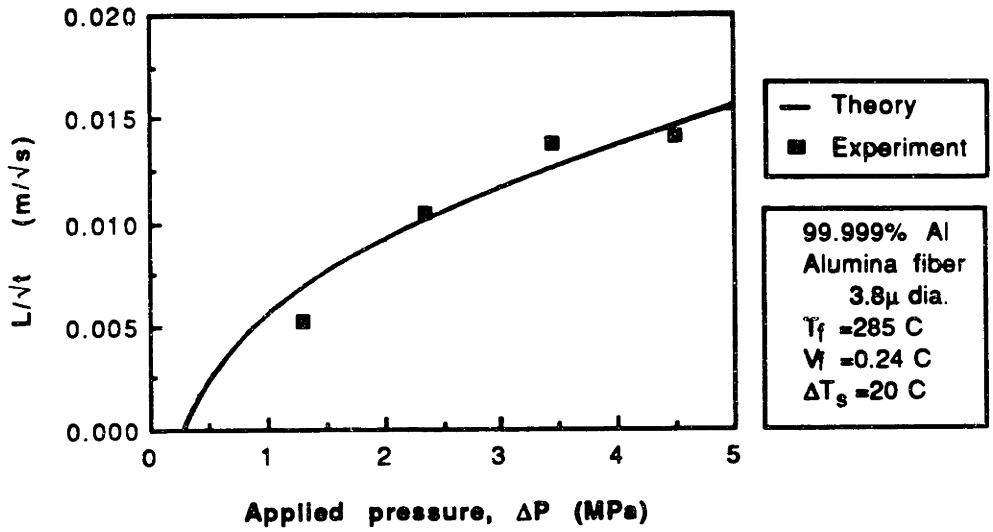

Figure 15: Effect of applied pressure on $L/\sqrt{t}$ Curve drawn is for 20°C of superheat and a capillary pressure of 0.3MPa.

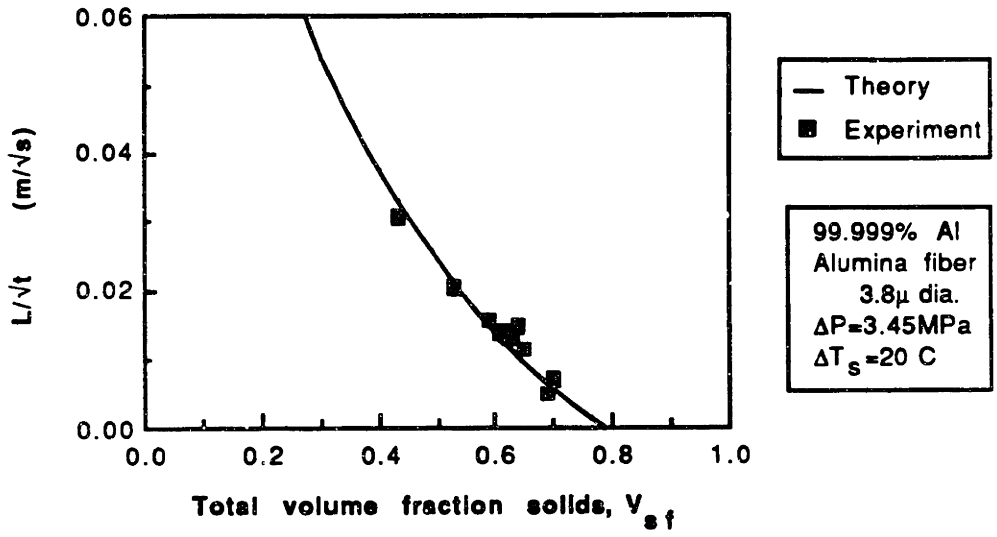

Figure 16: Unification of the effects of fiber volume fraction and temperature by considering the total solid material in the fiber preform. The experimental points are for a range of fiber volume fractions from 0.22 to 0.26 and a range of fiber temperatures from 210°C to 468°C.

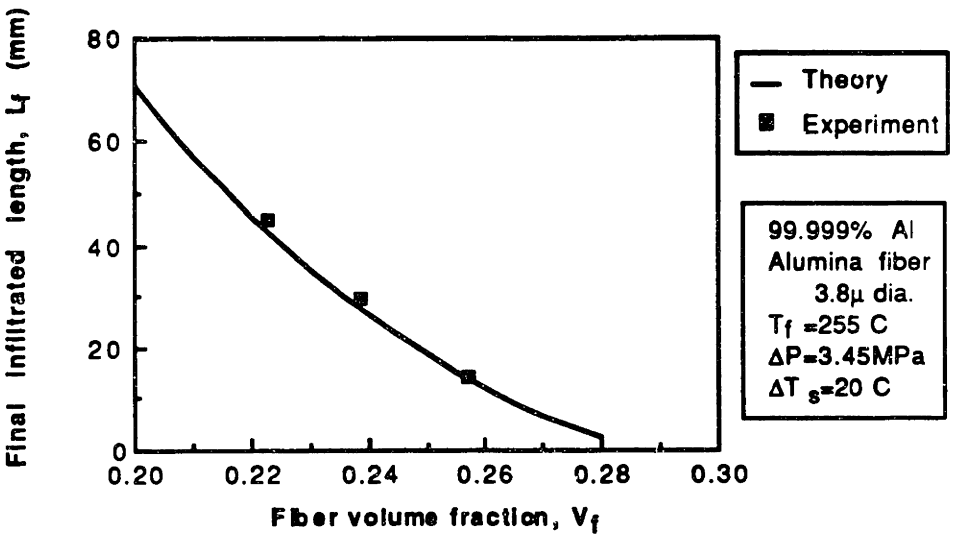

Figure 17: Effect of fiber volume fraction on final infiltrated length. Theoretical curve assumes h_e=250W/m^{2}K.

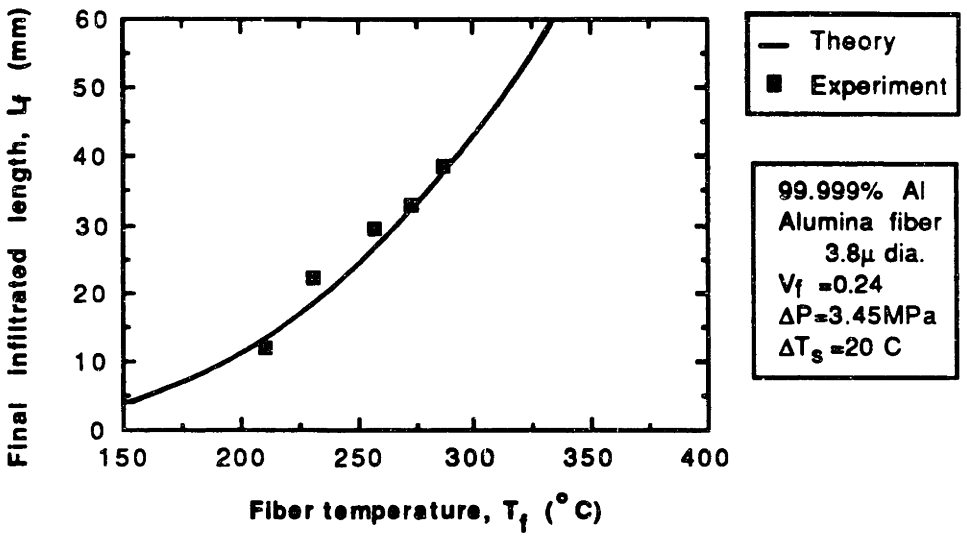

Figure 18: Effect of fiber temperature on final infiltrated length. Theoretical curve assumes h_e=250W/m^2 K.

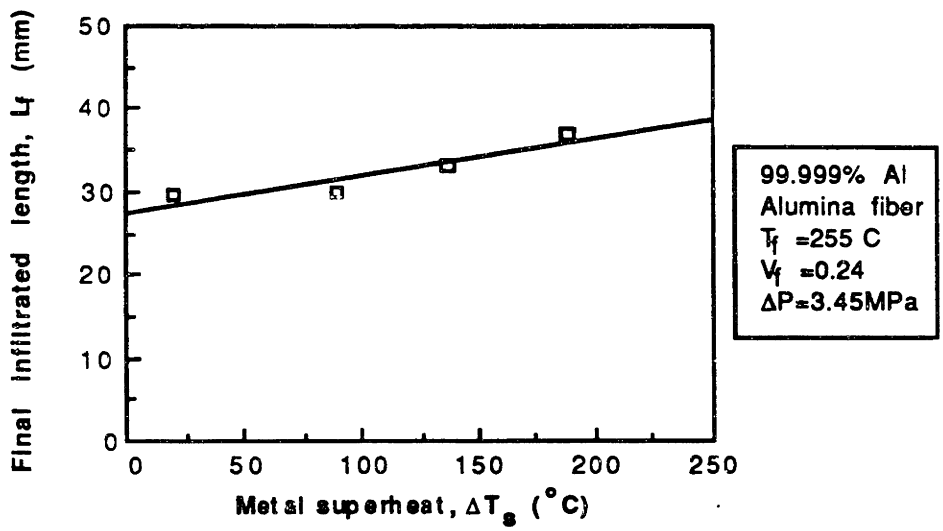

Figure 19: Effect of metal superheat on final infiltrated length. Line drawn is least squares fit through experimental data.

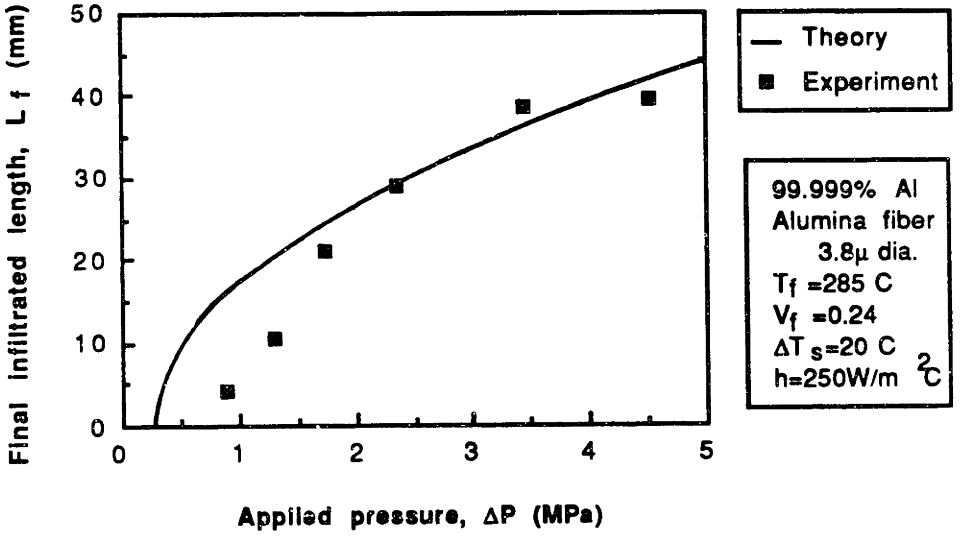

Figure 20: Effect of applied pressure on final infiltrated length. Calculations assume h_e=250W/m^{2}K.

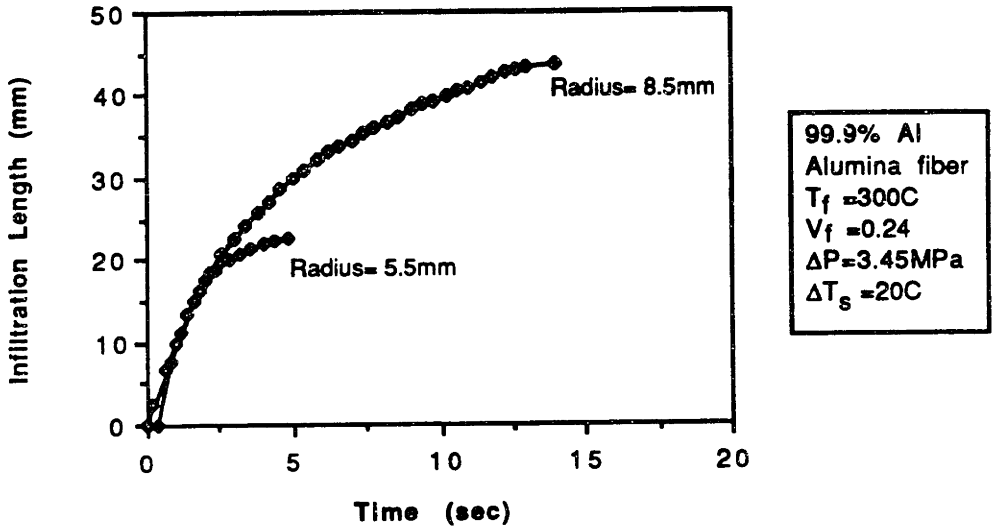

Figure 21: Effect of mold radius on infiltration behavior.

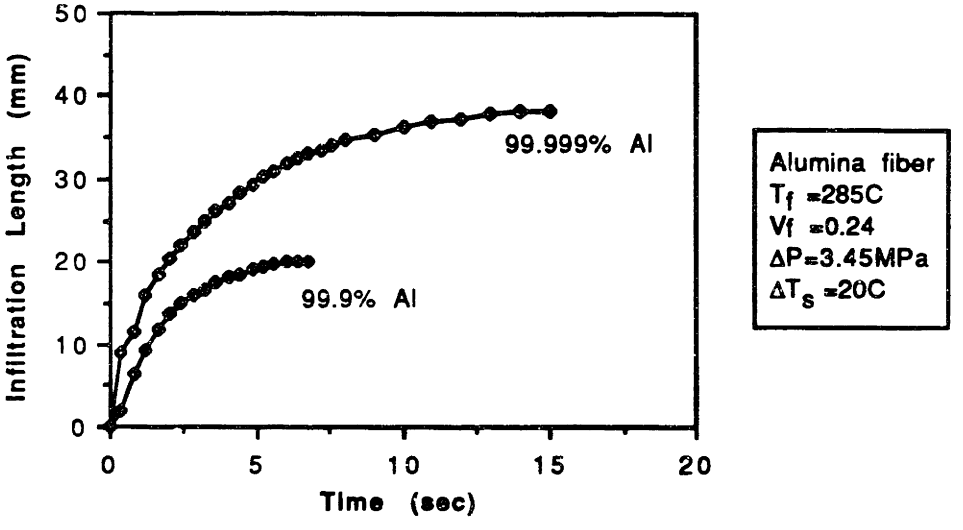

Figure 22: Effect of metal purity on infiltration behavior.

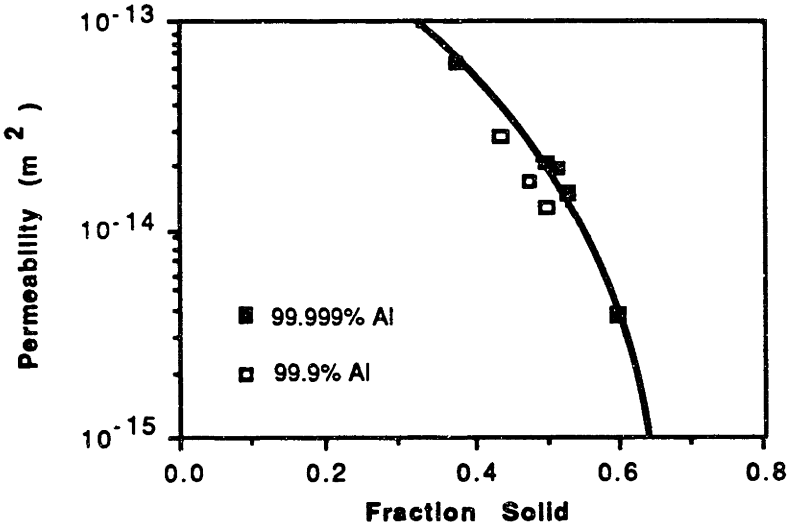

Figure 23: Measured permeability during experiments with 99.999% and 99.9% aluminum, compared with those calculated from theoretical considerations. For 24 volume percent alumina fibers.

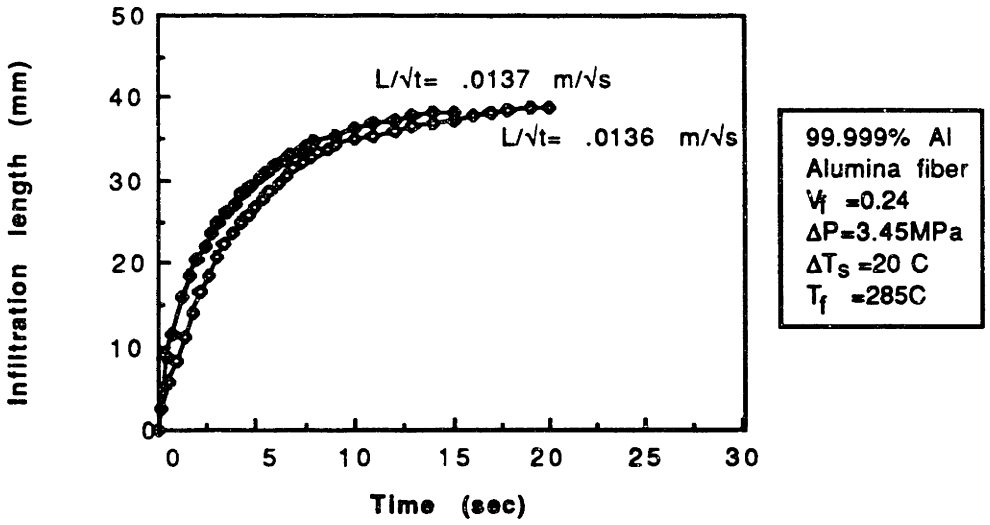

Figure 24: Example of the reproducibility of the infiltration process as measured with the SiC filament sensor technique.

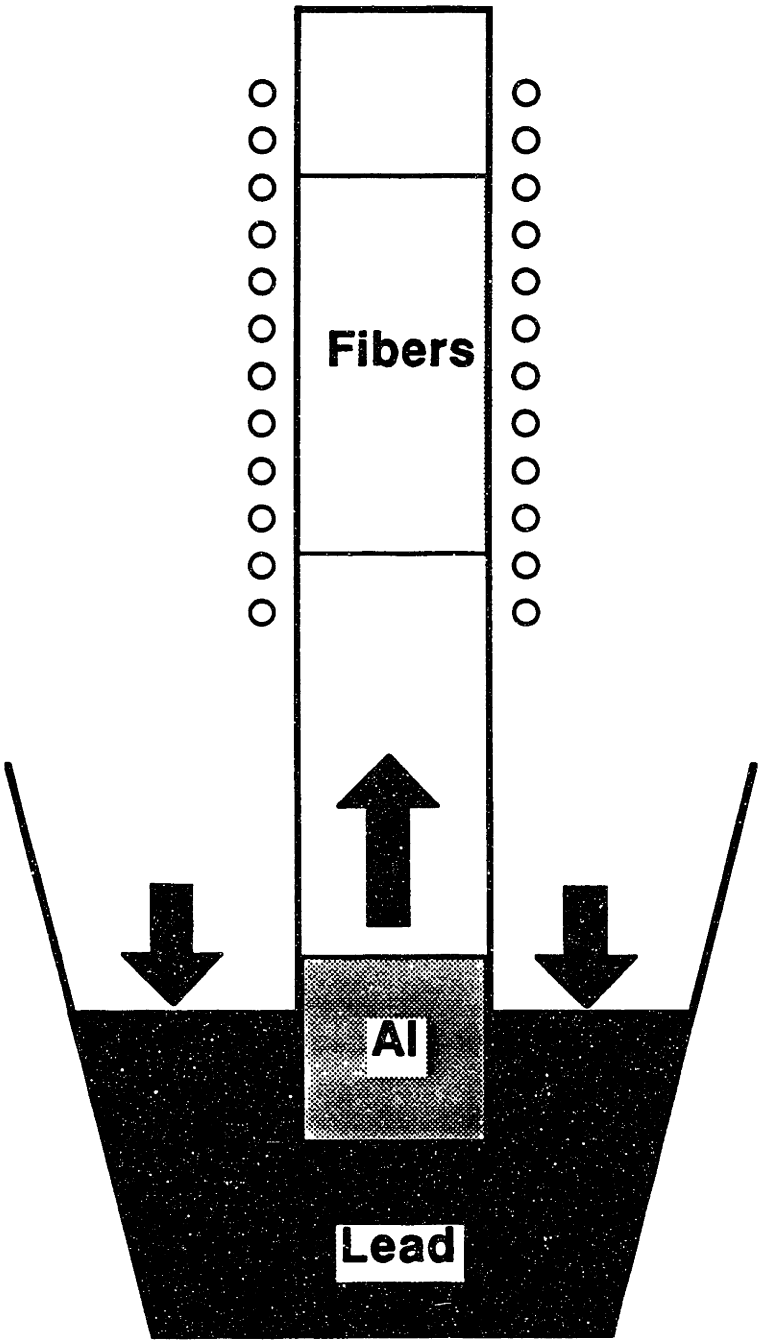

Figure 25: Technique for infiltrating a small amount of aluminum followed by molten lead.

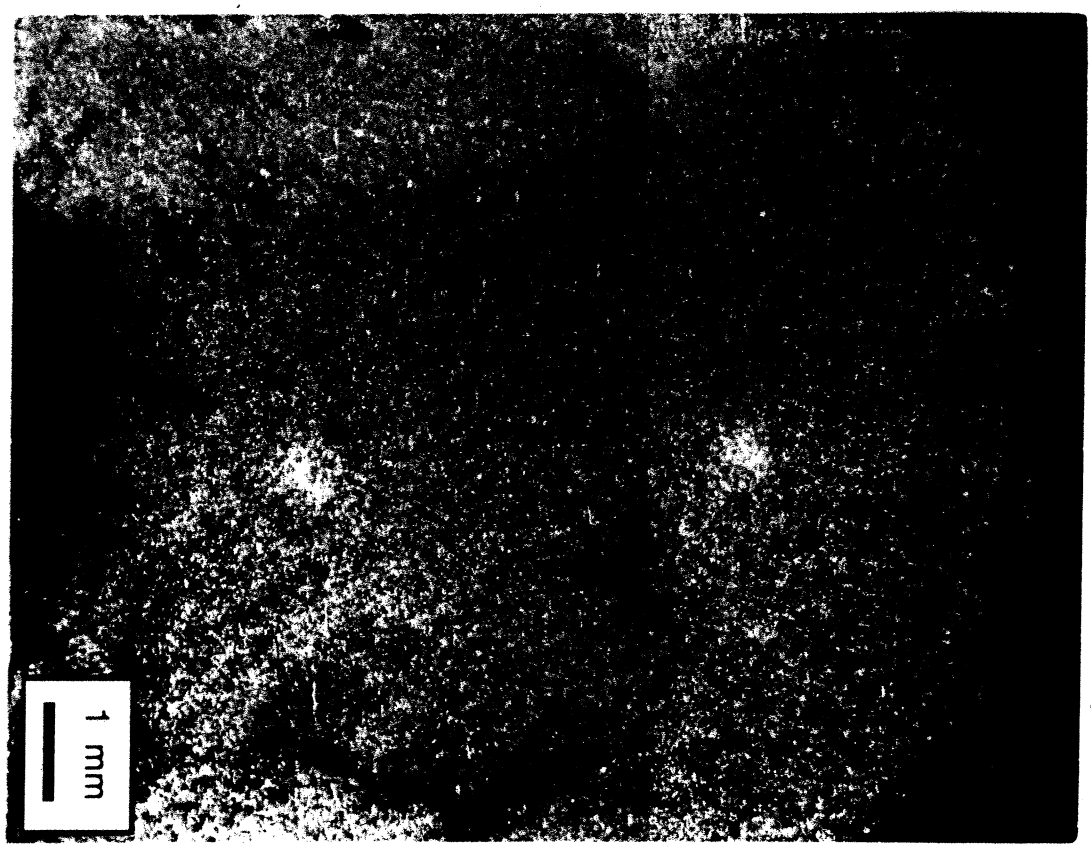

Figure 26: Photomicrograph of infiltration by aluminum followed by lead. Dark regions are lead, light regions are aluminum. Infiltration proceeded from left to right.

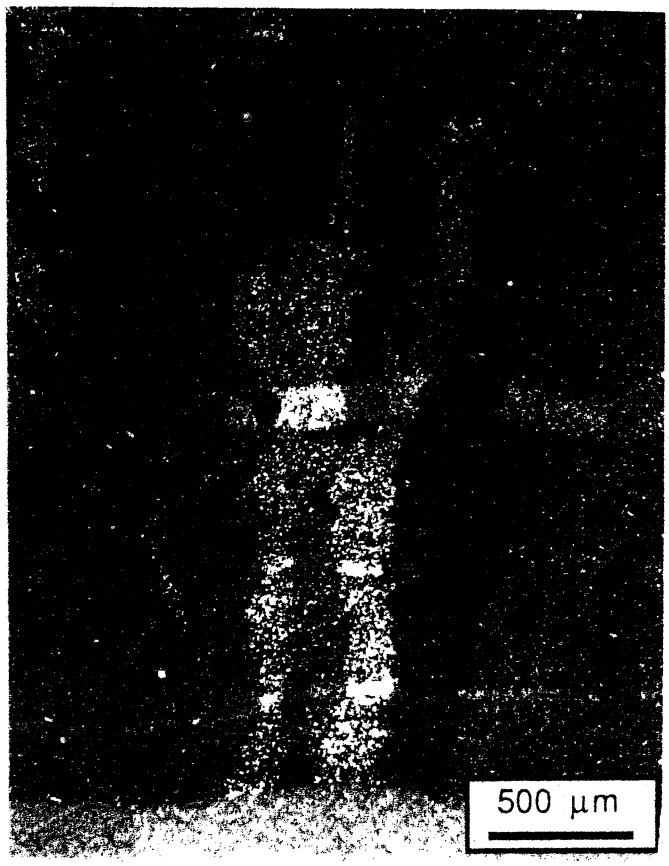

Figure 27: Photomicrograph of preform entrance region of etch-pitted composite viewed under cross-polarized light. Infiltration occurred upwards.

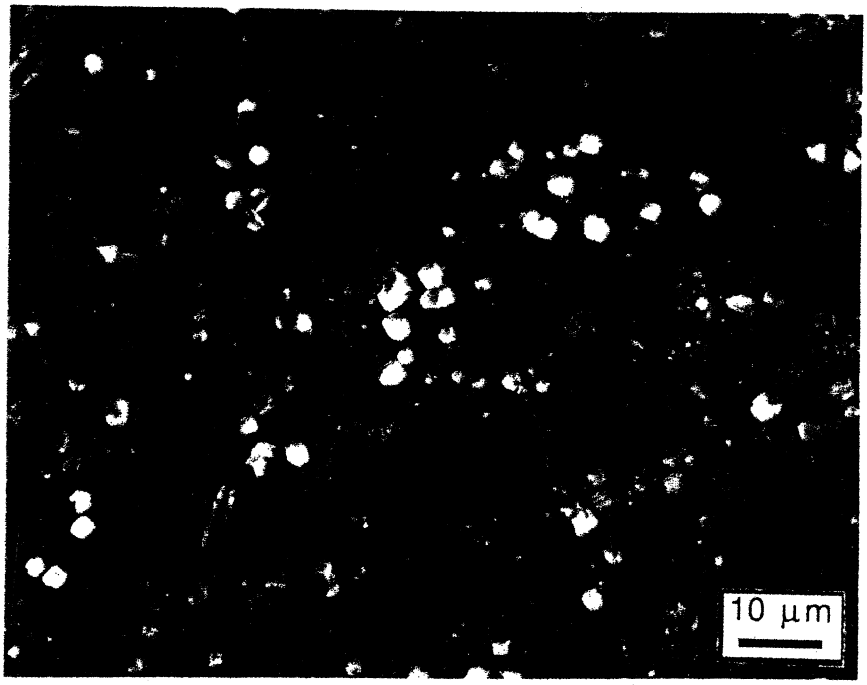

Figure 28: Photomicrograph of infiltration front region of etch-pitted composite viewed under cross-polarized light. Note the many orientations of etch pits in the volume shown.

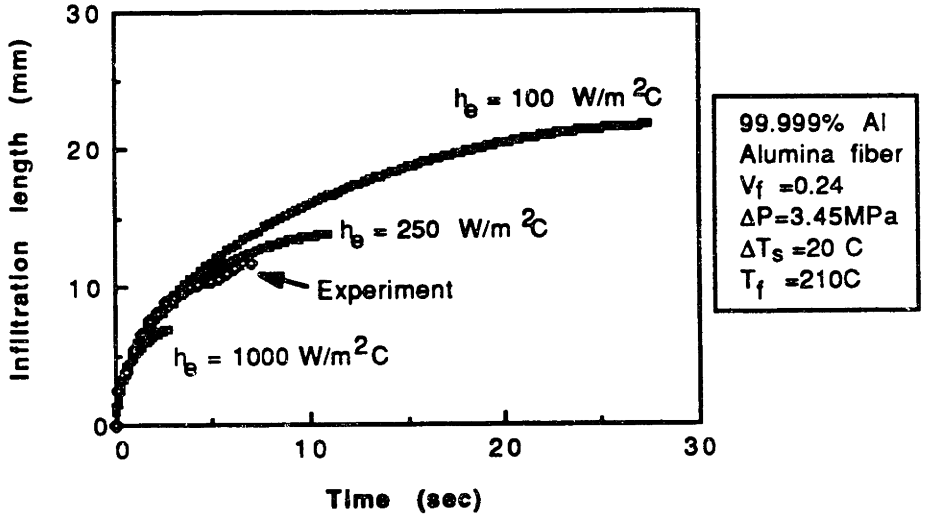

Figure 29: Calculated infiltration profiles for three values of h_e , plus a superimposed profile from an experiment. Indicates empirical selection of h_e =250 W/m^2 K.

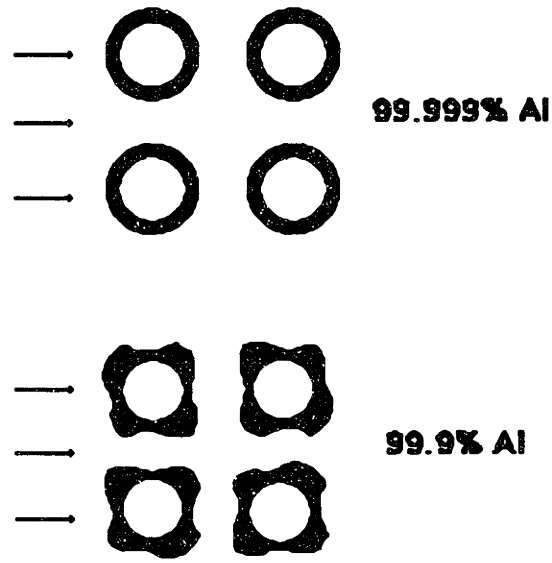

Figure 30: Schematic drawing of possible effect of impurities on solidification morphology.

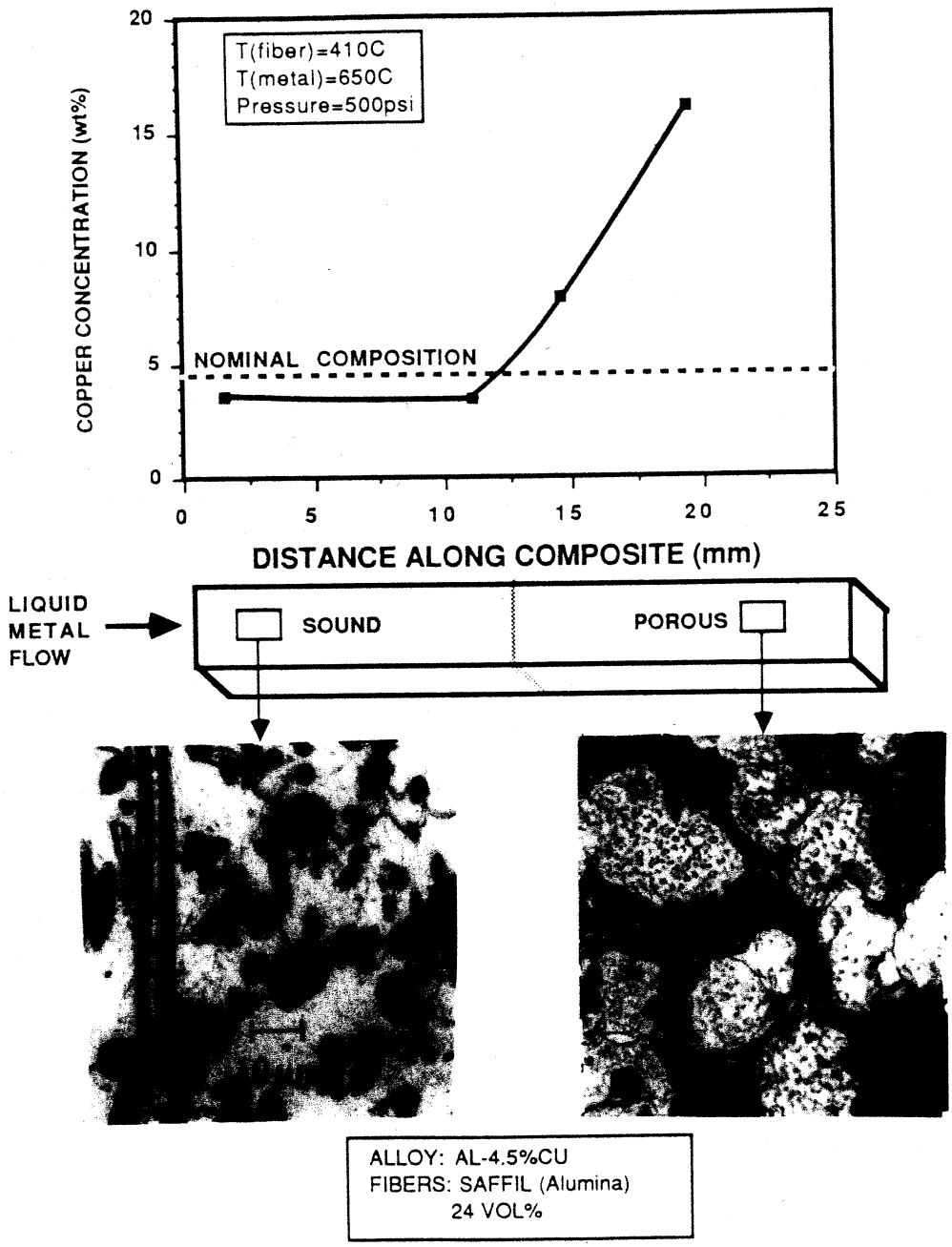

Figure B1: Illustration of macrosegregation resulting from infiltration of molten alloy into a cold fiber preform. Copper concentration increases in the porous region of the casting, resulting in a microstructure enriched in eutectic. Sound portion of casting is solute impoverished.

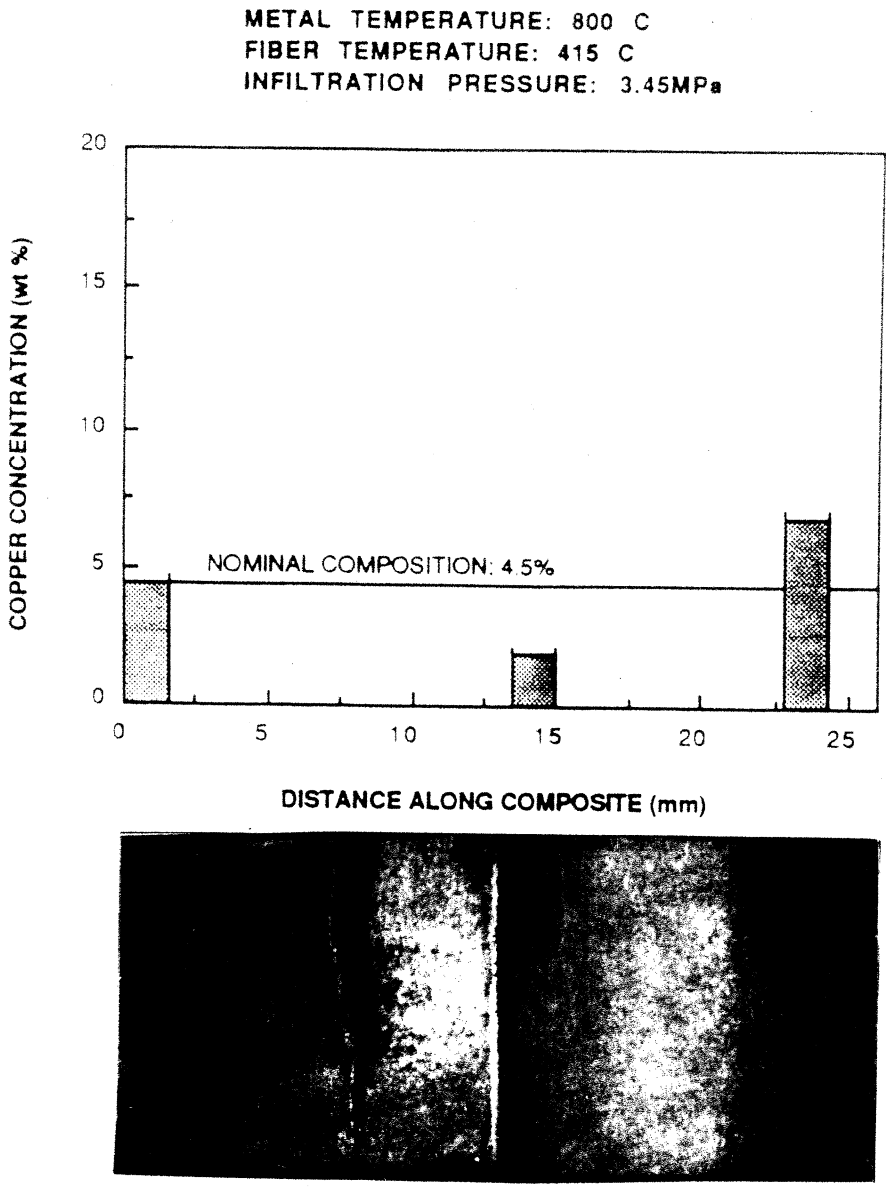

Figure 82 Illustration of macrosegregation resulting from infiltration of superheated alloy into a cold fiber preform. Coarse-grained region at left corresponds to remelted metal and contains the nominal solute concentration.

```
REM***INFILTRATION PROFILE FOR H-CONTROLLED HEAT TRANSFER
DIM X(200)
DIM L(200)
DIM R(200)
  PRINT"FIBER VOLUME FRACTION"
  INPUT VF
  PRINT"FIBER PREHEAT TEMPERATURE"
  INPUT TI
  PRINT"INFILTRATION PRESSURE (IN MEGAPASCALS)"
  INPUT P
        P=P*1000000!
  PRINT"RADIUS OF MOLD (IN METERS)"
  INPUT RI
  PRINT"INTERFACIAL HEAT TRANSFER COEFFICIENT (IN W/M^2 C)"
  INPUT HE
  GS= (.00421*VF*(660-TI)) / (1-VF)
  VS= VF+ (GS*(1-VF))
  LCONST= ( .314*3.61E-12*P / (.0013*VF*(1-VF)) )* (1-SQR(VS/.785))^2.5
  RCONST= (2*HE*(660-TI)) / ((1-VS)*RI*9.5E+08)
  KI= SQR(2*LCONST)
  T=0
  TCRIT=1/RCONST
  DT=TCRIT/100
  N=0
  X(0)=0
  X(1)= KI*SQR(DT)
  OPEN "CLIP:" FOR OUTPUT AS #1
    WRITE#1,0,0
INTEGRATION:
    N=N+1
    T = T+DT
      IF 1-(RCONST*T)<0 GOTO FINISH
    INTEGRAL=0
      FOR I=0 TO N-1
        R(I) = 1-(RCONST* ((N-I)*DT) )
        R(I+1) = 1-(RCONST* ((N-(I+1))*DT) )
        INTEGRAL = INTEGRAL+(  (2*(X(I+1)-X(I)) ) / (R(I)+R(I+1))    )
      NEXT I
     L(N+1) = LCONST*DT/INTEGRAL
     X(N+1) = X(N)+L(N+1)
     PRINT T, 1000*X(N)
     WRITE#1,T,1000*X(N)
  GOTO INTEGRATION
FINISH:
  CLOSE#1
END
```

Figure C1

```
REM***INFILTRATION PROFILE FOR CONDUCTION-CONTROLLED HEAT
TRANSFER
DIM X(200)
DIM L(200)
DIM R(200)
VF=.24
TI=260
P=3450000!
RI=.0085
KMOLD=2
RHOCMOLD=3100000!
  GS= (4000000!*(660-TI)*VF) / (9.5E+08*(1-VF))
  VS= VF+ (GS*(1-VF))
  LCONST= ( .314*3.61E-12*P / (.0013*VF*(1-VF)) )* (1-SQR(VS/.785))^2.5
  RCONST= (2*(660-TI)*SQR(1.273*RHOCMOLD*KMOLD)) /
              ((1-VS)*RI*9.5E+08)
  KI= SQR(2*LCONST)
  T=0
  TCRIT=1/RCONST^2
  DT=TCRIT/100
  N=0
  X(0)=0
  X(1)= KI*SQR(DT)
  OPEN "CLIP:" FOR OUTPUT AS #1
    WRITE#1,0,0
INTEGRATION:
    N=N+1
    T = T+DT
      IF 1-(RCONST*SQR(T))<0 GOTO FINISH
    INTEGRAL=0
      FOR I=0 TO N-1
        R(I) = 1-(RCONST*SQR((N-I)*DT))
        R(I+1) = 1-(RCONST*SQR((N-(I+1))*DT))
        INTEGRAL = INTEGRAL+(  (2*(X(I+1)-X(I)) ) / (R(I)+R(I+1))   )
      NEXT I
      L(N+1) = LCONST*DT/INTEGRAL
      X(N+1) = X(N)+L(N+1)
      PRINT T, X(N)*1000
      WRITE#1,T,X(N)*1000
  GOTO INTEGRATION
FINISH:
  CLOSE#1
END
```

Figure C1 - cont.

```
REM***INFILTRATION PROFILE WHEN HEAT TRANSFER TO FIBERS IS
NON-INSTANT.
DIM X(200)
DIM VS(200)
DIM K(200)
  PRINT"FIBER VOLUME FRACTION"
  INPUT VF
  PRINT"FIBER RADIUS"
  INPUT RF
  PRINT"FIBER PREHEAT TEMPERATURE"
  INPUT TF
  PRINT"INFILTRATION PRESSURE (IN MEGAPASCALS)"
  INPUT P
        P=P*1000000!
  PRINT"INTERFACIAL HEAT TRANSFER COEFFICIENT (IN W/M^2 C)"
  INPUT H
  PRINT"TIME INCREMENT"
  INPUT DT
    VSCONST=.00421*VF*(660-TF)
    HCONST=-2*H/(4000000!*RF)
    KCONST=.314*RF^2/VF
    XCONST=P/(.0013*(1-VF))
    KI= SQR(2*XCONST*KCONST*(1-SQR(VF/.785))^2.5)
    KIREF= SQR(2*XCONST*KCONST*(1-SQR((VF+VSCONST)/.785))^2.5)
  T=0
  N=0
  X(0)=0
  X(1)= KI*SQR(DT)
  L=KI*SQR(DT)
  OPEN "CLIP:" FOR OUTPUT AS #1
SUMMATION:
    N=N+1
    T = T+DT
    SUM=0
      FOR I=1 TO N
        VS(I)   =VSCONST*(1-EXP(HCONST*(N-I)*DT))
        VS(I-1)=VSCONST*(1-EXP(HCONST*(N-(I-1))*DT))
        VSAVG=(VS(I)+VS(I-1))/2
        K(I)=KCONST*(1-SQR((VF+VSAVG)/.785))^2.5
        SUM=SUM+X(I)/K(I)
      NEXT I
    X(N+1)=XCONST*DT/SUM
    L=L+X(N+1)
    LREF=KIREF*SQR(T)
    LRATIO=L/LREF
    PRINT T, LRATIO
    WRITE#1,T,LRATIO
  IF LRATIO>1.1 GOTO SUMMATION
  CLOSE#1
END
```

Figure C1 - cont.

```
REM***FINITE DIFFERENCE APPROXIMATION FOR HEAT FLUX INTO A
REM***MOLD OF FINITE THICKNESS WITH ADIABATIC OUTER WALL
OPEN "CLIP:" FOR OUTPUT AS #1
WRITE#1, 0, 0
PRINT "NUMBER OF DIVISIONS"
INPUT N
PRINT "VALUE OF H"
INPUT H
DIM T(N+1)
DIM TPREV(N+1)
TM=660
TI=210
KQRTZ=2
ALPHA=6.5E-07
L=.001
RI=.0085
DR=L/N
DT=DR^2/(2*ALPHA)
TIMELIMIT=INT(15/DT)
PRINT "NUMBER OF ITERATIONS:";TIMELIMIT
PRINT "NUMBER OF SKIPS IN CALCULATING FLUX"
INPUT SKIP
C1=H*RI
C2=KQRTZ/LOG((RI+DR)/RI)
C3=3.14159*((RI+L)^2-RI^2)
C4=2*3.14159*DR
REM***INITIALIZE TEMPERATURE
  FOR J=0 TO N
    TPREV(J)=TI
  NEXT J
REM***CALCULATE TEMPERATURES
  FOR I=1 TO TIMELIMIT
      FOR J=1 TO N-1
        R=RI+(N-J)*DR
        T(J)=.5*(TPREV(J-1)*(1-DR/(2*R))+TPREV(J+1)*(1+DR/(2*R)))
      NEXT J
    T(0)=T(1)
    T(N)=(TM*C1+T(N-1)*C2)/(C1+C2)
REM***SET UP PREVIOUS TEMPERATURES
      FOR J=0 TO N
        TPREV(J)=T(J)
      NEXT J
  REM***STORE FLUX AT DESIGNATED INTERVALS
    IF I MOD SKIP <>0 GOTO ILOOP
    SUM=0
      FOR J=1 TO N
        R=RI+(N-J)*DR
        SUM=SUM+C4*R*(.5*(T(J)-T(J-1))+T(J-1)-TI)
      NEXT J
    DIMFLUX=SUM/((TM-TI)*C3)
    FO=ALPHA*I*DT/L^2
```

```
      PRINT "T(0)=";T(0),"T(N)=";T(N)
      PRINT I, FO, "FLUX="; DIMFLUX
      WRITE#1, FO, DIMFLUX
ILOOP:  NEXT I
CLOSE #1
END
```

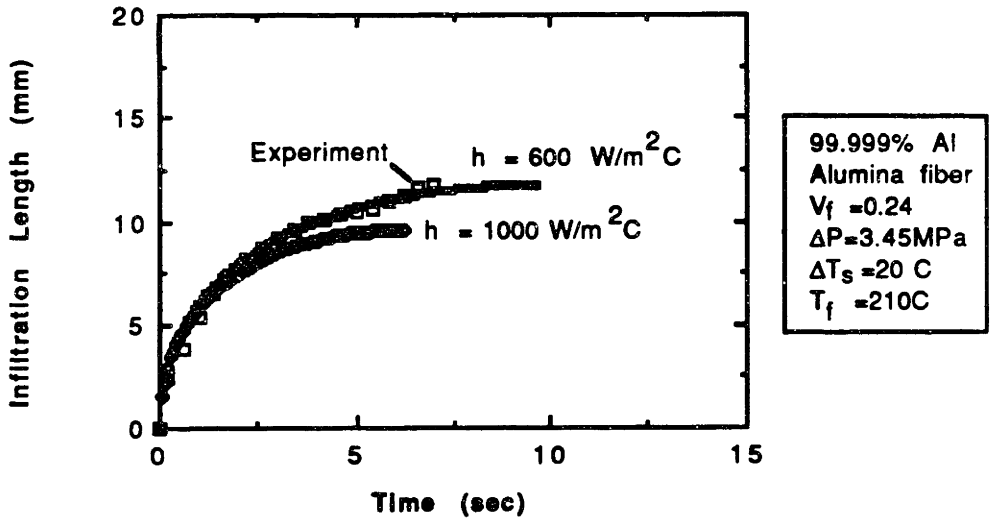

Figure C2: Calculated infiltration profiles for heat loss into a cylindrical quartz mold of finite wall thickness, from finite difference approximation in Appendix C. Superimposed experimental data indicates h = 600W/m^2 K.

Chapter 3
CONCLUSIONS

1. General expressions are given to describe the infiltration of a fibrous preform by a pure metal. They are solved analytically for some simplified cases of practical interest.
2. For the case of fibers at a temperature below the metal melting point, flowing pure metal will solidify as a sheath surrounding the fibers. Both fiber volume fraction and fiber temperature influence the amount of solid formed, with fiber volume fraction imparting a more significant effect on the infiltration kinetics.
3. For the case of fibers at a temperature below the metal melting point, the effect of metal superheat is to remelt the solid metal sheath that has formed around the fibers. The length of the remelted region always remains a fixed fraction of the total infiltration length for the case of constant applied pressure, no external heat extraction, and instantaneous heat transfer between the metal and fibers. From this model the influence of metal superheat on infiltration kinetics is minor.
4. For the case of no external heat extraction, constant applied pressure, and instantaneous heat transfer between the metal and fibers, flow through the preform will continue

indefinitely. When external heat extraction is present, flow will cease when solidification from the external heat sink has closed the flow channel. This will occur first at the entrance to the fiber preform and can be predicted analytically for simple geometries. The final infiltrated length can then be predicted upon knowledge of the external heat transfer kinetics.

5. Infiltration pressure does not affect the preform permeability. Therefore, under a constant applied pressure, instantaneous heat transfer between the metal and fibers, and negligible capillary pressure, the effect of infiltration pressure on final infiltrated length is parabolic.
6. An infiltration apparatus using pressurized gas was designed and built to enable infiltration under carefully controlled processing conditions. A sensor was developed to measure the flow of liquid metal through a fibrous preform and thus quantitatively test the calculations of infiltration kinetics.
7. Quantitative agreement of theory with experiment for aluminum metal and alumina fibers was shown under a variety of processing conditions. The processing parameters investigated were 1) fiber volume fraction, 2) fiber temperature, 3) metal temperature, and 4) applied pressure.
8. The mechanism of remelting of solid metal due to metal superheat was verified metallographically. Also, the mechanism of flow cessation due to external heat extraction was verified by the same technique.

9. The simple analytical model presented in this work can be used to predict quantitatively the infiltration behavior of a pure metal into a preform of aligned fibers under the application of a constant pressure.

Chapter 4

SUGGESTIONS FOR FURTHER WORK

The work on the pure aluminum system has been nearly completed. However, there are two areas that are in need of further investigation: 1) experimental verification of the morphology of solidification on the fibers, and 2) quantification of the role of capillary pressure. For the former, an experimental technique using the immiscible aluminum-lead system has been established and used for macroscopic verification of remelting. The technique can be extended with the use of careful metallography to include a microscopic investigation of the morphology of solidification around the fibers, with particular attention to the difference in morphology between 99.9% and 99.999% aluminum.

For the latter, it is suggested that a series of experiments be performed using a variety of fiber temperatures and volume fractions to measure the capillary pressures. The calculations of Mortensen and Cornie (*Metall. Trans. A*, 1987, vol.18A, pp.1160-1163) and of Clyne and Mason (*Metall. Trans. A*, 1987, vol.18A, pp.1519-1530) provide two techniques of calculating capillary pressure. The verification of one or the other would advance the knowledge of a very critical and actively debated area.

The next obvious step after the understanding and description of the infiltration of a pure metal is an understanding of the infiltration of an alloy. In the aluminum system, aluminum-4.5%copper is an ideal alloy due to its well understood solidification behavior and its applicability to other aluminum alloys of engineering importance. Some experimental work on this alloy has been performed by this author. Significant amounts of macrosegregation were observed, however no quantitative work of sufficient detail was performed to report any conclusions. This system is also an analytical challenge due to the presence of concurrent heat, fluid, and mass transfer.

Finally, another major step between a laboratory curiosity and an engineering application for the liquid infiltration process is the elimination of casting porosity. This porosity has at least three sources: 1) metal feeding and shrinkage during solidification, 2) poor infiltration of interfiber spaces, and 3) entrapment of gas. This area of research has barely been touched and is ripe for quantitative investigation.

BIOGRAPHICAL NOTE

Lawrence Jay Masur was born in Newington, Connecticut on December 27, 1956. He was graduated from Newington High School in 1975, and then attended University of Connecticut in Storrs, Connecticut. He graduated from the honors program at the University of Connecticut in 1979 with a B.S. in Physics. He was elected a University Scholar and member of Phi Beta Kappa at that time. During the summers of 1979 and 1980 he worked at United Technologies Research Center in East Hartford, Connecticut. He entered the graduate school of Massachusetts Institute of Technology in September 1979 and received the degree of Master of Science in Metallurgy in June 1982. Upon graduation he was employed as a research metallurgist at TRW Castings Division in Cleveland, Ohio. He re-entered the graduate school of MIT to work on a Doctorate in January 1985.